Mechanistic Understanding and Enhancing Pool Boiling Heat Transfer via Surface Property and Structure Design

by

Youngsup Song

M.S., Yonsei University (2012)

B.S., Yonsei University (2010)

Submitted to the Department of Mechanical Engineering in

Partial Fulfillment of the Requirements for the degree of

Doctor of Philosophy in Mechanical Engineering

at the

Massachusetts Institute of Technology

September 2021

Signature of Author: .....

Department of Mechanical Engineering

August 12, 2021

Certified by:.....

Evelyn N. Wang

Ford Professor of Engineering and Department Head of Mechanical Engineering

Thesis Supervisor

Accepted by:.....

Nicolas Hadjiconstantinou

Professor of Mechanical Engineering

Chairman, Department Committee on Graduate Theses

Intentionally blank page

Mechanistic Understanding and Enhancing Pool Boiling Heat Transfer via Surface Property and Structure Design

by

Youngsup Song

Submitted to the Department of Mechanical Engineering on August 30th, 2021,

in Partial Fulfillment of the Requirements for the Degree of Doctor of Philosophy

Abstract

Boiling is a vital process used to transfer heat effectively via harnessing the large latent heat of vaporization for a variety of energy and thermal management applications. The boiling heat transfer performance is described mainly by critical heat flux (CHF) and heat transfer coefficient (HTC), which quantifies the operational heat flux limit and the efficiency of boiling heat transfer, respectively. The goal of this thesis is two-fold: fundamental understanding on the mechanisms associated with CHF and significantly enhancing pool boiling heat transfer. First, we addressed the large discrepancy of experimental CHF values on flat surfaces reported in the literature by accounting for hydrocarbon adsorption and oxidation of metallic surfaces during boiling. Accordingly, we developed an experimental protocol based on this understanding on the causes of spread in CHF values and used the protocol throughout this thesis for consistent experimental measurements.

We subsequently investigated the effects of surface structures on enhanced CHF during pool boiling of hemi-wicking surfaces. We systematically designed micropillar surfaces with controlled roughness and wickability, and combined the results with scaling analysis to obtain a unified descriptor for CHF. This unified descriptor represents the combined effects of the extended contact line length and volumetric wicking rate, which shows a reasonable correlation with CHF values with our experiments and literature data.

Next, we engineered boiling surfaces to achieve simultaneous CHF and HTC enhancements. We developed a microtube structure, where a cavity is defined at the center of a pillar, to enhance the heat transfer characteristics in controllable manner. In addition to uniform microtube arrays, we designed a surface with microtube clusters interspersed with micropillars, referred to as tube-clusters in pillars (TIP), to mitigate the earlier boiling crisis

of uniform microtube arrays due to the extensive bubble coalescence. While uniform microtube arrays and TIP surfaces showed significant enhancement of both CHF and HTC compared to a flat surface, there was an intrinsic trade-off between CHF and HTC associated with the nucleation site density. Accordingly, we proposed hierarchical TIP (h-TIP) surfaces to control vapor nucleation with multi-scale structures while providing capillary wicking. These surfaces showed CHF and HTC enhancements up to 138 and 389%, respectively, compared to a flat surface.

Finally, we investigated the use of sandblasting as a scalable surface engineering technique for enhanced pool boiling heat transfer for industry-scale applications. Pool boiling results along with surface characterizations on silicon surfaces showed that surface roughness and volumetric wicking rates increased with the sandblasting abrasive size. As a result, CHF and HTC values enhanced up to 192.6 and 433.6% compared to a flat surface, respectively.

This thesis provides important insights to understand the role of surface properties and structures on pool boiling heat transfer, thereby providing guidelines for the systematic design of surface structures for enhanced pool boiling heat transfer.

Thesis Committee:

Professor Evelyn N. Wang (Thesis Advisor/Chair), Department of Mechanical Engineering

Professor Rohit Karnik, Department of Mechanical Engineering

Professor Matteo Bucci, Department of Nuclear Science & Engineering

Acknowledgements

First and foremost, I would like to express my deepest gratitude to my advisor, Professor Evelyn Wang, for her exceptional guidance and mentorship. Her insights, guidance, supports, and trust made my PhD journey extremely rewarding both academically and personally. Thank you, Evelyn. I am so privileged to have had you as my thesis advisor. I would like to also thank my thesis committee members, Professor Rohit Karnik and Professor Matteo Bucci, who provided insightful comments that completed this thesis, throughout our meetings.

I sincerely thank everyone at the Device Research Lab for stimulating discussions, supports, and, most of all, friendship. The DRL is a fantastic team. None of projects would have been possible without numerous discussions with the lab members. In particular, I would like to give special thanks to Dan Preston, Yangying Zhu, Jeremy Cho, and Zhengmao Lu for their great mentorship early on in my PhD studies. More broadly, I acknowledge colleagues with whom I closely worked with: Lenan Zhang, Kyle Wilke, Md Mahamudur Rahman, Shuai Gong, Geoffrey Vaartstra, Carlos Díaz-Marín, Yajing Zhao, Samuel Cruz, Hyeongyun Cha, Chi Wang, and Guanyu Su. I am immeasurably benefitted to have had the chance to work with and learn from you all.

I also acknowledge Kurt Broderick at MIT.nano for his support on microfabrication.

I have been fortunate to make great friendships outside of the lab as well; especially, I thank Mech-A-Pink crews and KGSA soccer team. Small talks over coffee and playing soccer have been positive resources charging me up to get through research endeavors.

I am immensely grateful for my parents for their unconditional support.

Finally, I thank you, MJ, my wife, for everything.

Intentionally blank page

Table of Contents

Intentionally blank page

List of Figures

List of Tables

Intentionally blank page

Chapter One

Introduction

Boiling is a liquid-to-vapor phase change process accompanying the nucleation of vapor bubbles within a bulk liquid, as opposed to evaporation, which can occur below a boiling point and does not generate bubbles. Boiling can be classified into pool boiling and flow boiling according to the presence of external fluid flow. Pool boiling is boiling on a heated surface submerged in a stagnant pool of liquid. Flow boiling, on the other hand, takes place in a flowing fluid, where an external pump typically forces the flow. The type of a boiling system can be determined according to the complexity, dimension, and heat transfer requirements of an overall system. This thesis focuses on a pool boiling system.

1.1 Motivation

The worldwide demand for electrical power has been continuously growing ~3% annually during the past decade [1]. Roughly 80% of this electrical power and 88% of energy in the United States in 2019 were produced by steam turbines with conventional and renewable resources such as natural gas, coal, nuclear energy, biomass, and geothermal energy, where the steam is generated through a boiling process (Top left panel of Figure 1.1) [2]. Steam

generation is also deeply engaged in sustainability such as food and chemical processing, water purification and sterilization (Bottom panels of Figure 1.1) [3-6]. Furthermore, the effective heat dissipation capability of boiling, by harnessing the large latent heat of vaporization, has potential in thermal management of high flux applications such as concentrated photovoltaics, fast-charging batteries, data centers, and integrated electronics (Top right panel of Figure 1.1) [7-10]. The increasing demand and complexity of boiling applications imply the greater importance of the reliable and accurate estimation and enhancement of boiling heat transfer.

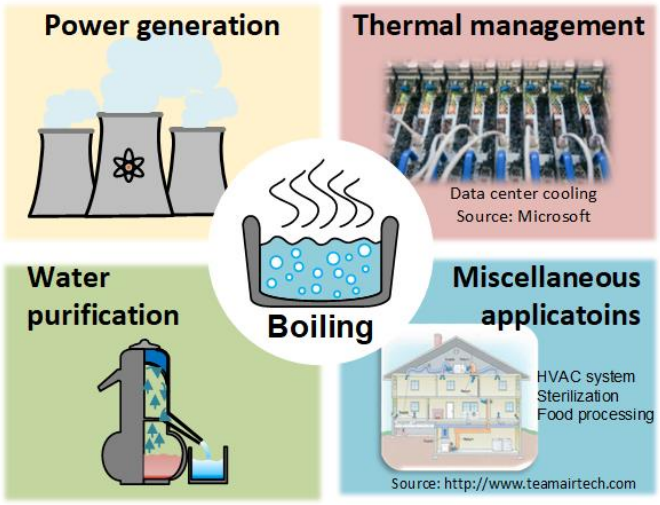

Figure 1.1. Ubiquitous boiling applications

1.2 Background

1.2.1 The boiling curve

Pool boiling heat transfer is commonly described by a boiling curve, *i.e.*, a plot of heat flux (q'') as a function of wall superheat (ΔT_w) (Figure 1.2). Here, wall superheat is the temperature difference between the boiling surface (T_w) and the saturated bulk fluid (T_{sat}), *i.e.*, $\Delta T_w = T_w - T_{sat}$, where T_{sat} is 100℃ for water at atmospheric pressure. Although a conventional boiling curve plots the heat flux and wall superheat on the y-axis and x-axis, respectively, a control parameter during boiling is usually the heat flux in actual operations. Nukiyama was the first who characterized pool boiling heat transfer using this boiling curve, where he identified different boiling regimes [11]. Figure 1.2 shows a typical boiling curve of pool boiling of water at atmospheric pressure with ballpark numbers on each axis. At low heat fluxes, the heat transfer takes place by single-phase natural convection. As the heat flux increases, the liquid near the wall is superheated and starts to nucleate vapor bubbles at the onset of nucleate boiling (ONB). As soon as bubbles nucleate on the wall, the wall superheat decreases momentarily due to the large latent heat of vaporization transported from the wall by bubbles. In addition to transporting the latent heat, bubbles induce fluid flow near the wall, which becomes more dynamic at a higher heat flux, and increase the convective heat transfer. This nucleate boiling provides very efficient heat transfer and, thus, most boiling applications operate in the nucleate boiling regime. The efficiency of boiling heat transfer is described by heat transfer coefficient (HTC, h), defined as the ratio of heat flux to the wall superheat, *i.e.*, $h = q''/\Delta T_w$. The heat flux, however, cannot increase infinitely. When the heat flux is sufficiently high, excessive vapor bubbles nucleated on the boiling surface prevent the liquid from rewetting the surface and, in turn, form an insulating vapor film over the surface. This vapor film becomes a thermal barrier that leads to a drastic increase in wall superheat

and burnout of a boiling system. This transition from nucleate boiling to film boiling is known as the departure from nucleate boiling (DNB), or a boiling crisis, where the maximum heat flux before reaching the DNB is called critical heat flux (CHF). The CHF, therefore, represents the operational limit of nucleate boiling. Between the nucleate and film boiling regimes, there is a transition boiling regime, where both nucleate and film boiling occur partially. The transition boiling regime is, however, very unstable and difficult to be characterized by controlling heat flux. In this thesis, all boiling curves are characterized up to CHF.

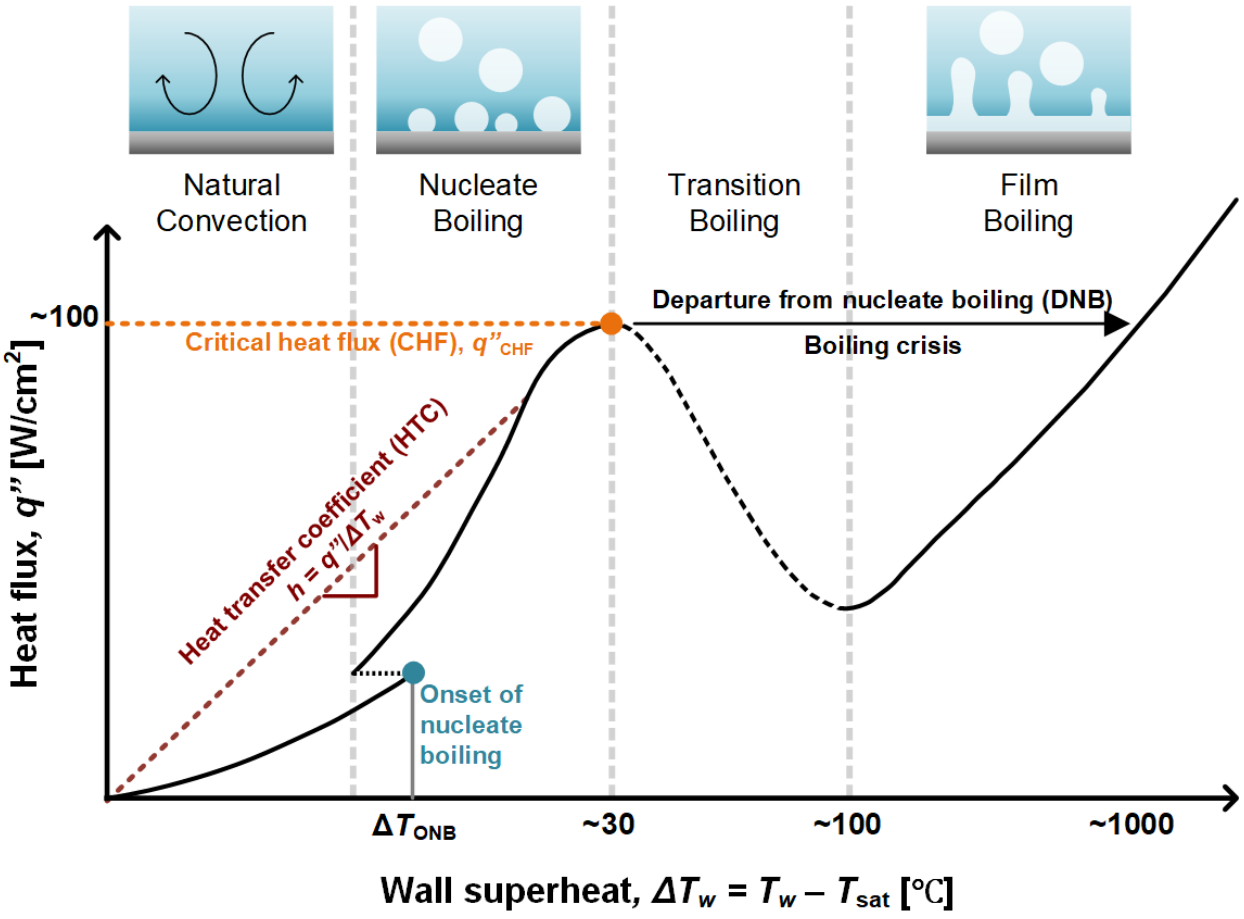

Figure 1.2. Schematic of a typical pool boiling curve of water at atmospheric pressure in log scales. There are four boiling regimes: natural convection, nucleate boiling, transition boiling, and film boiling. The heat transfer coefficient (HTC) and critical heat flux (CHF) are two major parameters that quantify the boiling performance. A typical CHF value for pool boiling of water on a flat surface is ~100 W/cm^2.

1.2.2 Effects of surface wettability on CHF

In general, phase-change heat transfer performance depends strongly on surface wettability to promote the formation of droplets (for condensation) or bubbles (for boiling), which can depart easily [12]. In condensation, for example, surface flooding – coverage with a fluid film over a condenser – can be delayed with a non-wetting condenser surface, *i.e.*, a surface on which the condensate exhibits a large contact angle (θ) (Figure 1.3a) [13, 14]. On such a surface, nucleated droplets readily coalesce and shed due to gravity, even up to high heat fluxes, which prevents surface flooding. Conversely, in boiling, a wetting surface, *i.e.*, one on which the boiling liquid forms a small contact angle, generates the desired growth and departure of small bubbles because the phases of the nucleating entity and the surrounding environment are the opposite of those in condensation (Figure 1.3b) [15, 16]. In the case of boiling, a small liquid contact angle allows bubbles nucleated on the surface to easily depart when buoyancy exceeds surface tension [17], which maintains the nucleate boiling regime up to high heat fluxes and prevents the transition to the film boiling regime. In other words, a small liquid contact angle is desired to delay a boiling crisis and exhibit a high CHF value.

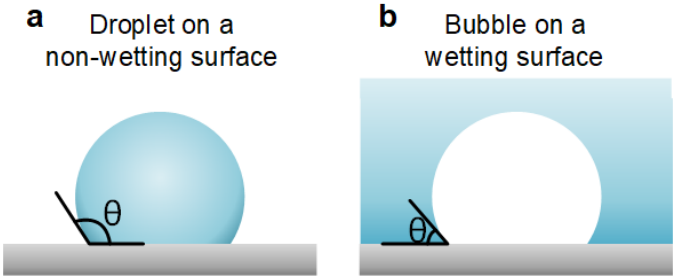

Figure 1.3. Surface wettability and a contact angle (θ). (a) A non-wetting surface with θ>90° can delay surface flooding in condensation. (b) A wetting surface with θ<90° can delay a boiling crisis.

1.2.3 Engineered boiling surfaces

Significant enhancement of pool boiling heat transfer, above that can be enhanced by wettability, has been achieved by engineering working fluid or surface properties [18, 19]. In particular, engineering boiling surfaces has received a greater attention for boiling heat transfer enhancement, as constraints on chemical compatibility or operational conditions may limit the choice of working fluid. Surfaces with microcavities or heterogeneous wettability patterns, also known as the biphilic wettability, for example, have improved HTC values by promoting vapor bubble nucleation [20-23]. Surfaces with permeable structures such as micropillars, microchannels and nanowires, in contrast, have shown significant enhancement of CHF values by harnessing the contact line augmentation and capillary-fed rewetting, that is, surface wickability [24-29]. In particular, a strong relationship between CHF values and the surface wickability has been widely reported [26, 27, 30]. A few studies have combined micro-permeable structures (micropillars or microchannels) with functional coatings, for example, self-assembled monolayers, reduced graphene oxide membranes, and porous copper layers, which exploit micro-permeable structures and the coatings to enhance CHF and HTC values, respectively [31-33]. The addition of nanostructures to microstructures or to heterogeneous wettability patterns has shown further increase in CHF and HTC values [21, 26, 27, 34, 35].

1.3 Thesis objectives and outline

The goal of this thesis is two-fold:

- Fundamental understanding on the mechanisms associated with CHF
- Significantly enhancing pool boiling heat transfer by engineering surface structures

Accordingly, the chapters are organized as follows:

- Chapter 2 explains two different pool boiling experimental setups used for this thesis.
- Chapter 3 addresses the large discrepancy of experimental CHF values on flat surfaces reported across the literature by accounting for hydrocarbon adsorption and oxidation of metallic surfaces during boiling. Accordingly, we developed an experimental protocol based on this understanding on the causes of spread in CHF values and used the protocol throughout this thesis for consistent experimental measurements.
- Chapter 4 investigates the effects of surface structures on enhanced CHF during pool boiling of hemi-wicking surfaces. We systematically designed micropillar surfaces with controlled roughness and wickability, and combined the results with scaling analysis to obtain a unified descriptor for CHF. This unified descriptor represents the combined effects of the extended contact line length and volumetric wicking rate, which shows a reasonable correlation with CHF values with our experiments and literature data.
- Chapter 5 explores engineered boiling surfaces for the simultaneous enhancement of CHF and HTC. We developed a microtube structure, where a cavity is defined at the center of a pillar, to enhance the heat transfer characteristics in controllable manner. In addition to uniform microtube arrays, we designed a surface with microtube clusters interspersed with micropillars, referred to as tube-clusters in pillars (TIP), to mitigate the earlier boiling crisis of uniform microtube arrays due to the extensive bubble coalescence. While uniform microtube arrays and TIP surfaces showed significant enhancement of both CHF and HTC compared to a flat surface, there was an intrinsic trade-off between CHF and HTC associated with the nucleation site density. Accordingly, we proposed hierarchical TIP (h-TIP) surfaces to control vapor nucleation with multi-scale structures while providing capillary wicking. These

surfaces showed CHF and HTC enhancements up to 138 and 389%, respectively, compared to a flat surface.

- Chapter 6 proposes the use of sandblasting as a scalable surface engineering technique for enhanced pool boiling heat transfer for industry-scale applications. Pool boiling results along with surface characterizations on silicon surfaces showed that surface roughness and volumetric wicking rates increased with the sandblasting abrasive size. As a result, CHF and HTC values enhanced up to 192.6 and 433.6% compared to a flat surface, respectively.
- Finally, Chapter 7 summarizes the thesis and discusses future directions.

Chapter Two

Pool boiling experimental setup

Two different pool boiling setups were used in this thesis. For silicon-based samples, we created a 100 nm serpentine platinum (Pt) heater on the backside of each sample, through which heating power was applied. These silicon samples were tested on the thin-film heater-based setup described in Chapter 2.1. For metal coupons, we soldered the samples to a copper block, which was heated by cartridge heaters. Details of this cartridge heater-based setup are explained in Chapter 2.2.

2.1 Thin-film heater-based setup

The thin-film heater-based pool boiling setup consisted of a glass chamber with an Ultem fixture at the bottom and a polyether ether ketone (PEEK) fixture at the top (Figure 2.1a). The test sample was attached to the Ultem fixture with adhesive sealant (High-temperature RTV Silicone, Permatex). A rope heater helped the glass chamber maintain the saturation temperature by preventing heat loss. At the top of PEEK fixture, an immersion heater and a reflux condenser were installed. We first pre-heated de-ionized water in a separate electric kettle before introducing the water into the glass chamber. The immersion heater was used

to degas the pre-heated water by boiling for another 30 minutes (this period of time of degassing was varied in Chapter 3.3 as a control parameter) before experimental measurements. The reflux condenser condensed water vapors and allowed them to fall back to the pool as liquid. A power supply (KLP 600-4-1200, Kepco) provided power for Joule heating through the serpentine Pt heater that defined the heating area A_h. A multimeter (2110 5½, Keithley) formed a serial connection with the power supply and the sample for the current measurement across the heater (I), while the other multimeter (34401A, Agilent) was connected in parallel for the voltage-drop measurement (V). The input heat flux could therefore be calculated as $q''_{in} = (I \times V)/A_h$. The size of test sample used in Chapter 4 was 12 × 18.5 mm^2 with a heating area A_h of 10 × 15 mm^2. All the other chapters (3, 5, and 6) used 20 × 20 mm^2–big samples with an A_h of 10 × 10 mm^2.

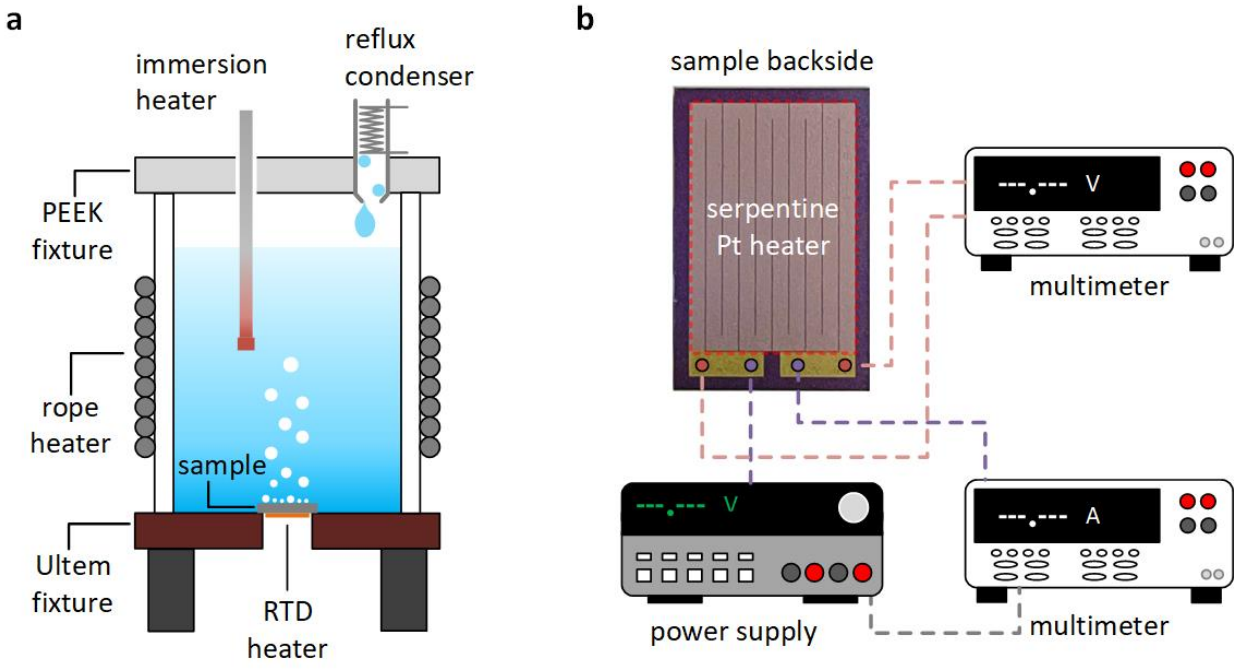

Figure 2.1. Thin-film heater-based pool boiling setup. (a) Pool boiling test rig. (b) Electrical circuits to apply power and measure the boiling heat flux and wall temperature.

The Pt backside heater also served as a resistance temperature detector (RTD) for temperature characterization. Prior to pool boiling experiments, test samples were placed in a furnace with a high accuracy Pt RTD (RTD-810, Omega Engineering) close to it. The heater resistance was then measured at five different temperature set points between 100 and 140℃. The dwell time at each set point was at least 2 hours to ensure thermal equilibrium within the furnace. The resistance was measured with the four-wire method using a temperature input module (NI-9226 and cDAQ-9171, National Instruments). The experimental data were fitted with a linear model as shown in Figure 2.2. This linear fit was used to convert the measured resistance to the temperature of the heater during pool boiling experiments.

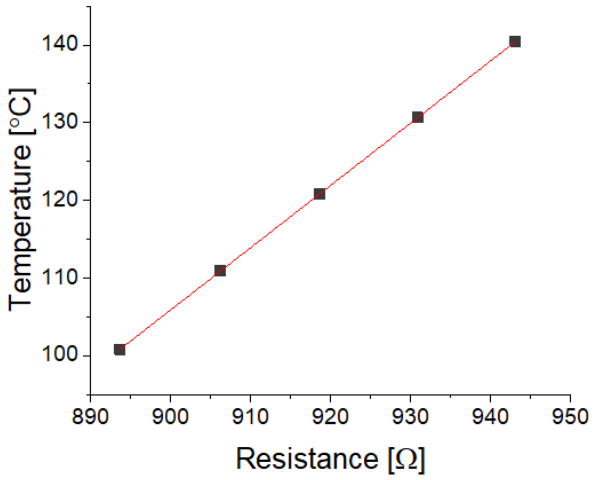

Figure 2.2. Backside heater temperature as a function of electrical resistance. The measured data (black squares) are fitted with a linear model (red line).

Due to the size mismatch between the actual heating area and the exposed surface area, there can be heat loss along the lateral direction through the sample thickness. We numerically calibrated (COMSOL Multiphysics 5.3a LiveLink for MATLAB) the boiling heat flux and wall superheat based on the measured input heat flux and the heater temperature

(Figure 2.3). In the numerical simulation, we iterated the calculations by changing the heat transfer coefficients at the boiling surface until the calculation results of the backside heater temperature matched the experimentally measured temperature. All data points in the boiling curves were calibrated in this manner.

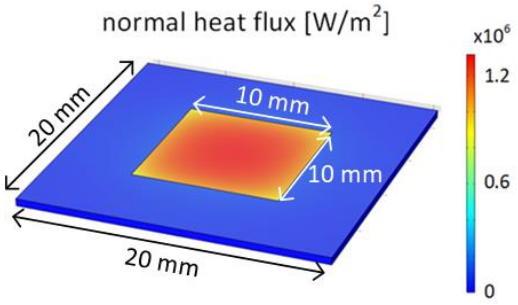

Figure 2.3. Numerical calibration results of a flat sample (20 × 20 mm^2) with a heating area of 10 × 10 mm^2 at CHF point.

The root-sum-of-squares (RSS) method of combining uncertainty components were used to evaluate the uncertainty propagation of experimental measurements [36]. The input heat flux was characterized based on the measurements of current, voltage, and the heater area, *i.e.*, $q''_{\text{in}} = f(V, I, A_{\text{h}})$. According to the RSS method, the estimated uncertainty of the input heat flux becomes

$$U_{q''_{\text{in}}}^2 = \left(\frac{\partial q''_{\text{in}}}{\partial V}\right)^2 U_{\text{V}}^2 + \left(\frac{\partial q''_{\text{in}}}{\partial I}\right)^2 U_{\text{I}}^2 + \left(\frac{\partial q''_{\text{in}}}{\partial A_{\text{h}}}\right)^2 U_{A_{\text{h}}}^2, \tag{2.1}$$

where U_{V}, U_{I}, and U_{A} are the uncertainties of the measured voltage, current, and the heating area, respectively. We can evaluate the partial derivatives and rearrange the equation (2.1), which results in

$$\frac{U_{q''_{\text{in}}}^2}{q''^2_{\text{in}}} = \frac{U_{\text{V}}^2}{V^2} + \frac{U_{\text{I}}^2}{I^2} + \frac{U_{A_{\text{h}}}^2}{A_{\text{h}}^2}. \tag{2.2}$$

Based on the manufacturer's specifications, the uncertainties of current (U_I) and voltage (U_V) are 10 μA and 2 mV, respectively. The uncertainty of heater area (U_A) is based on the photolithography resolution of 1 μm, which results in U_A of 0.04 mm^2. All of which give $U_{q"_{in}} \simeq 0.05$ W/cm^2 at CHF. In the numerical calibration, the HTC of non-boiling area was set to 4 kW/(m^{2}K) which is based on the slope of boiling curves before the onset of nucleate boiling. When there is 25% change in the HTC of non-boiling area, the resulting boiling heat flux changes up to ~2%. Considering that $U_{q"_{in}}$ is relatively negligible, the uncertainty of heat flux was estimated based on the uncertainty of non-boiling area HTC, which yield to ~ 2% error at CHF points.

2.2 Cartridge heater-based setup

Metal coupons in Chapter 3.3 were tested on a cartridge heater-based pool boiling setup (Figure 2.4). The boiling rig consisted of three major parts: a boiling chamber, a sample-mounted copper block, and a heating copper block. The boiling rig consisted of three major parts: a boiling chamber, a sample-mounted copper block, and a heating copper block. The boiling chamber part was similar to the thin-film heater-based setup. The two copper blocks were initially separated each other. A sample was soldered to the top copper block using a solder paste (Delta 717D, Qualitek). Three K-type thermocouples (SCAIN-020U-6, Omega) were inserted at the center axis of the top copper block with 5 mm spacing (Δx) to measure the temperature gradient. The measured temperatures were then converted to the heat flux based on Fourier's law with a three-point backward finite difference approximation, *i.e.*, $q" = k_{\mathrm{Cu}} \frac{3T_1 - 4T_2 + T_3}{2\Delta x}$, where T_1, T_2, and T_3 are the temperature measurements from the top,

middle, and bottom thermocouples, respectively, and k_{Cu} is the temperature-dependent thermal conductivity of copper ($k_{\mathrm{Cu}} = 2.83 \times 10^{-4}T^2 - 0.165T + 378.1$ [W/mK], where T is in K) [37]. An additional thermocouple inserted right beneath the sample was used to calculate the boiling surface temperature (T_{w}) combined with the measured heat flux, *i.e.*, $T_{\mathrm{w}} = T_{\mathrm{tc}} - q"t/k$, where T_{tc}, t, and k are the temperature measured by the thermocouple right beneath the sample, thickness, and thermal conductivity of a metal coupon, respectively. The bottom copper block contained five 250 W cartridge heaters (35025K131, McMaster-CARR) to provide the boiling heat flux. When the experiment was ready, we raised the level of the bottom copper block using a lab jack until it formed a robust contact with the top copper block for heat transfer. The applied heat flux was increased with a 10 W/cm^2 increment using a power supply (KLP 600-4, Kepco). Once a boiling crisis occurred, we stopped the power supply and detached the bottom copper block from the top by lowering the lab jack.

The uncertainty propagation of experimental measurements was evaluated using the RSS method based on the uncertainties of temperature measurements (U_{T}) and spacing between thermocouples ($U_{\Delta \mathrm{x}}$). The uncertainty of $q"$ measured on the cartridge heater-based setup is

$$\frac{U_{q"}^2}{q"^2} = \frac{U_T^2}{T^2} + \frac{U_{\Delta x}^2}{\Delta x^2}. \tag{2.3}$$

The uncertainty of thermocouple measurement (U_{T}) is ±1.1 K. The uncertainty of spacing ($U_{\Delta \mathrm{x}}$) was evaluated based on the sheath diameter of thermocouples, *i.e.*, 254 μm. The resulting $U_{q"}$ near CHF (~100 W/cm^2) is, therefore, ~ 0.03 W/cm^2. While the $U_{q"}$ based on U_{T} and $U_{\Delta \mathrm{x}}$ is negligibly small, since the heat flux was measured with a 10 W/cm^2 increment, we evaluated the heat flux uncertainty as 10 W/cm^2.

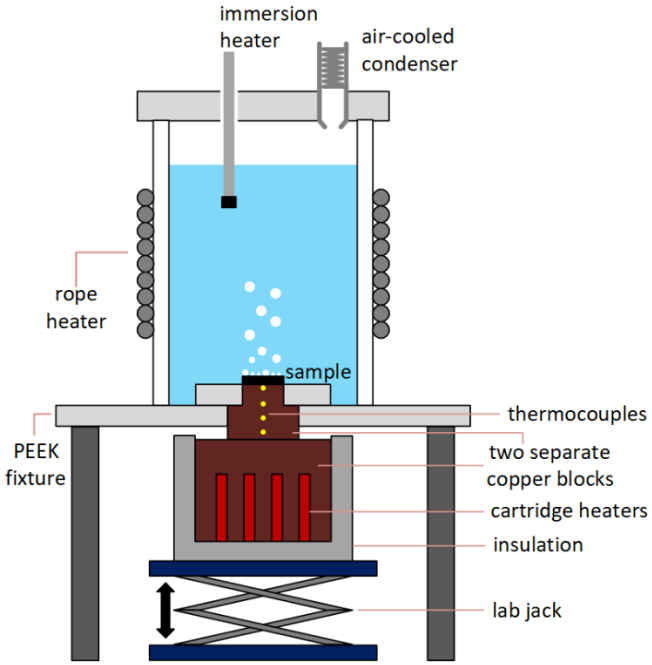

Figure 2.4. Cartridge heater-based pool boiling setup. A sample was attached to a top copper block, where four thermocouples are inserted for measurements. The bottom copper block contained five 250 W cartridge heaters to provide a boiling heat flux. The level of bottom copper block was controlled by a lab jack, so that the blocks could be attached during the boiling measurements and separated once the boiling crisis occurred.

Intentionally blank page

Chapter Three

Investigation of the spread in pool boiling CHF values on flat surfaces

3.1 Problem statement

While extensive efforts in the past decades have focused on engineering boiling surfaces to achieve CHF enhancement compared to that of a pristine and flat surface [19], CHF values of flat surfaces for pool boiling of water show a large discrepancy across the literature even for the same material (Figure 3.1). For example, CHF values on flat silicon (Si) and silicon dioxide (SiO_2) vary across the literature roughly from 60 to 110 W/cm^2 [21, 22, 24, 27, 29, 31, 38-50]. Metallic surfaces such as copper (Cu) and nickel (Ni) show even wider spreads in CHF values [26, 51-70], over the Zuber's CHF prediction for a flat surface [61]. Understanding the cause of this discrepancy is important for two reasons. First, an inaccurate CHF estimation could be detrimental for boiling applications such as nuclear power plants, where safety is the foremost concern. Second, the flat surface CHF is particularly important for the mechanistic

understanding of CHF because the flat surface CHF is used as a baseline value to which the enhancement of engineered surfaces is evaluated.

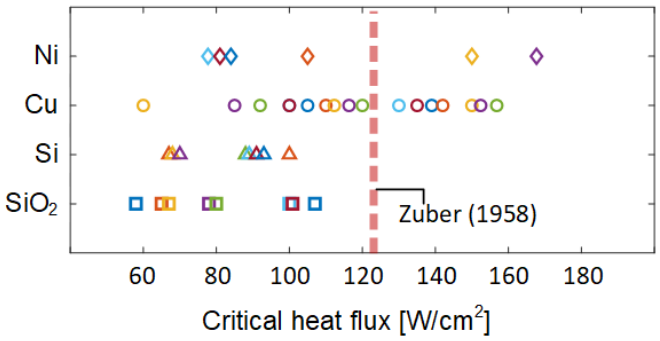

Figure 3.1. Large spread in reported CHF values during saturated pool boiling of water on flat nickel, copper, silicon, and silicon dioxide surfaces. All data used in this plot are summarized in Supplementary Information Table 8.1.

3.2 Effects of airborne hydrocarbon adsorption

3.2.1 Introduction

The dependence of CHF on wettability during pool boiling has been investigated and explained by a force-balance model that incorporates the contribution of surface tension and its dependence on contact angle [15]. On a flat surface, the interfacial energies among three phases (solid, liquid, and vapor) determine the contact angle. In other words, for a given combination of a liquid and a vapor with a known liquid-vapor interfacial tension, the contact angle is determined by the chemical surface interactions (quantified as surface energies) of the liquid and the vapor with the solid surface. However, Figure 3.1 shows that reported CHF values for pool boiling of water vary greatly even for the flat surfaces of the

same material. In this chapter, we explain the discrepancy of flat SiO_2 surfaces by accounting for hydrocarbon adsorption on a boiling surface.

Hydrocarbons are generally hydrophobic, and the adsorption of hydrocarbons on a surface can change the surface wettability towards hydrophobicity. Indeed, the amount of organic contaminants on a surface has often been characterized by the surface wettability [71]. This phenomenon has brought debates on the intrinsic wettability of materials as well. For example, in 1960s, Erb and Fowkes reported that gold was intrinsically hydrophobic [72, 73], which was contradicted by later findings that gold is, in fact, intrinsically hydrophilic, but becomes hydrophobic due to the rapid adsorption of airborne hydrocarbons on its surface [74-78]. A similar phenomenon and related debates were associated with various materials including metals and metal oxides [79-87], graphite and graphene [88, 89], and rare earth oxides [90]. These studies, conducted across many material classes and scientific disciplines, illustrate that the wettability may differ even for surfaces of the same material depending on the amount of hydrocarbon adsorption on the surface of the material, which, in the case of pool boiling, may cause the spread in reported CHF values.

3.2.2 Sample preparation

To investigate the effects of hydrocarbon adsorption on pool boiling heat transfer, we studied the correlation between the pool boiling CHF and the amount of adsorbed hydrocarbon on smooth SiO_2 surfaces. We chose SiO_2 surfaces because of their chemical stability in boiling water. First, we cleaned the flat SiO_2 surfaces with argon plasma to remove contaminants. The samples were then exposed to laboratory air (MIT Device Research Laboratory, ambient temperature= 22.5 ± 2.5℃, relative humidity = 25 ± 10%) for different periods of time (2 minutes, 7 hours, 24 hours, and 48 hours) before conducting pool boiling

experiments (Figure 3.2a). Argon plasma cleaning was carried out at 7.2 W for 15 min in a reaction chamber maintained at 600 mTorr (PDC-001, Harrick Plasma). X-ray photoelectron spectroscopy (XPS) data detailing atomic percent carbon on these surfaces was adopted from prior work by our group [90]. We chose argon plasma for cleaning because it removes surface contamination by physical bombardment, while oxygen- or hydrogen-based plasma reacts with the surface and chemically changes the surface wettability [91, 92]. Furthermore, the power of argon plasma we used does not alter surface roughness [93], which we confirmed with atomic force microscopy (AFM) scans of the test surfaces (Figure 3.2b); therefore, the wettability is not altered or enhanced by changes in the surface geometry on the plasma cleaned surfaces.

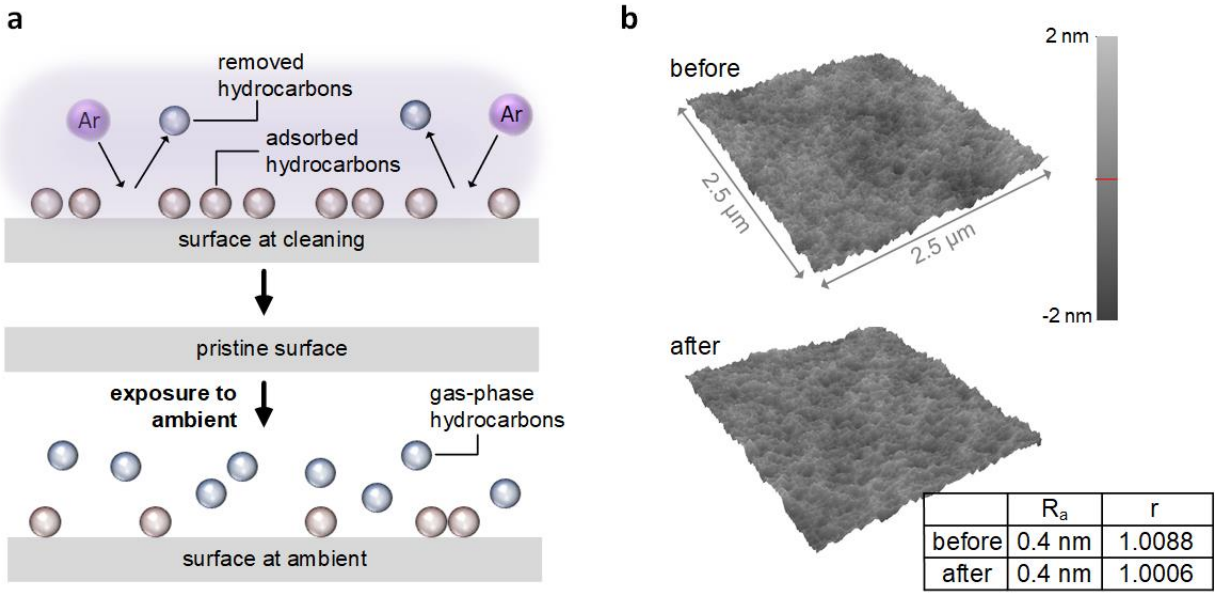

Figure 3.2. Argon plasma cleaning of surfaces and its effect on surface morphology. (a) Schematic showing sample preparation procedure. (b) Negligible change in the surface profiles of the smooth SiO_2 surfaces measured with AFM before (top) and after (bottom) argon plasma cleaning.

3.2.3 Results and discussion

Pool boiling curves of tested samples are plotted in Figure 3.3a. For comparison with the plasma-cleaned surfaces, another SiO_2 surface was prepared by solvent-cleaning, *e.g.*, acetone and isopropyl alcohol rinsing, without plasma cleaning. The surface exposed to laboratory air for only 2 minutes after plasma cleaning shows the highest CHF of 107 W/cm^2. CHF values decrease to 92.4, 82.3, and 76.6 W/cm^2 as the air exposure times increase to 7, 24, 48 hours, respectively, exhibiting a deviation in experimentally recorded CHF values of ~40%, all on the same underlying SiO_2 surface. The decrease in CHF on the smooth SiO_2 surface suggests that the surface becomes less hydrophilic over time. In addition to the decrease of CHF, the surface exposed to air for 2 minutes shows distinctly higher onset of nucleate boiling temperature (ΔT_{ONB}~20°C) compared with the others (<15°C), as shown in the inset of Figure 3.3a. This high ΔT_{ONB} is a characteristic of highly wetting surfaces because the energy barrier for the onset of nucleate boiling is higher for more wetting surfaces [94-96]. The contact angles of surfaces were measured to investigate the change in wettability. To avoid the change in surface conditions during the period between the contact angle measurement and boiling experiments, we developed an *in situ* contact angle measurement setup in the boiling chamber (Figure 3.3b), with which we could characterize the surface wettability in a saturated water environment right before the boiling experiments. To create a three-phase contact line for contact angle measurements, an air bubble was infused through a stainless-steel tube and placed on the surface. We placed a Teflon cover over the surface so as to prevent the bubble from leaving the surface by buoyancy; rather, it stayed in contact with the surface. We measured advancing and receding contact angles by infusing and withdrawing air with a syringe. Figure 3.3c and 3.3d show the markedly different wettability of two flat SiO_2 surfaces prepared by different cleaning procedures – the surface cleaned with solvents and the surface exposed to air for 2 minutes after argon plasma

cleaning, respectively. Both advancing and receding contact angles of the surface cleaned with argon plasma stayed ~5° (Figure 3.3d), while the solvent-cleaned surface showed a large contact angle hysteresis with larger advancing and receding contact angles (Figure 3.3c). This changing wettability, observed on the same flat SiO_2 surfaces, implies that the surface became less hydrophilic, presumably due to lower surface energy of adsorbed airborne hydrocarbons.

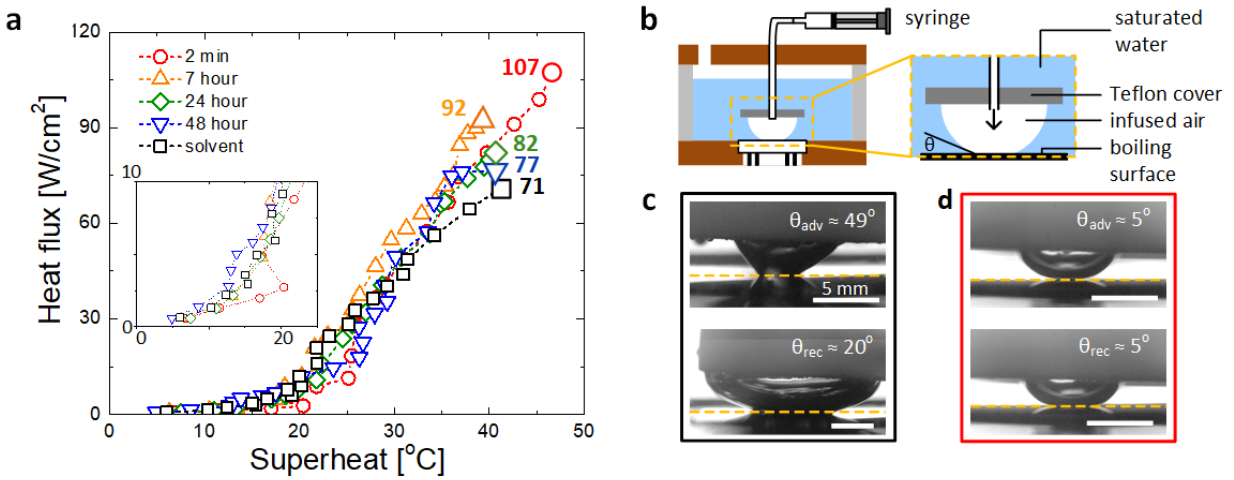

Figure 3.3. Pool boiling heat transfer and *in situ* contact angle measurements. (a) Experimental pool boiling curves. (b) Schematics of *in situ* contact angle measurement in a saturated water condition (not to scale). (c, d) Advancing (top) and receding (bottom) contact angles of the solvent-clean surface (c) and the surface exposed to air for 2 min after Ar plasma cleaning (d). Dashed lines show the surface boundaries. Scale bars are 5 mm.

Figure 3.4a shows the strong correlation between the CHF values and the amount of adsorbed hydrocarbons on the surfaces. The amount of hydrocarbons on the surface increased in time, while the CHF values decreased. The sharp increase of hydrocarbons at the early stage became more gradual as the time of exposure increased. The CHF values show a transient behavior similar to the amount of adsorbed hydrocarbon, *i.e.*, a sharp decrease at the beginning and more gentle decrease at later stages, which affirms the strong correlation

between these two parameters. In Figure 3.4b, we plot the measured amount of surface carbon with the Langmuir adsorption kinetic model [97], which describes the surface coverage ratio of adsorbate as a first-order differential equation in time, $d\theta/dt = k_a(1-\theta) - k_d\theta$, where θ, t, k_a, and k_d are the surface coverage ratio of adsorbate, time, adsorption rate, and desorption rate, respectively. The adsorption and desorption rate were used as fitting parameters. The well-matching general trend between XPS data of the amount of hydrocarbons on the surface and the governing equation of adsorption kinetics further corroborate that the hydrocarbons on the surface were from airborne hydrocarbon adsorption.

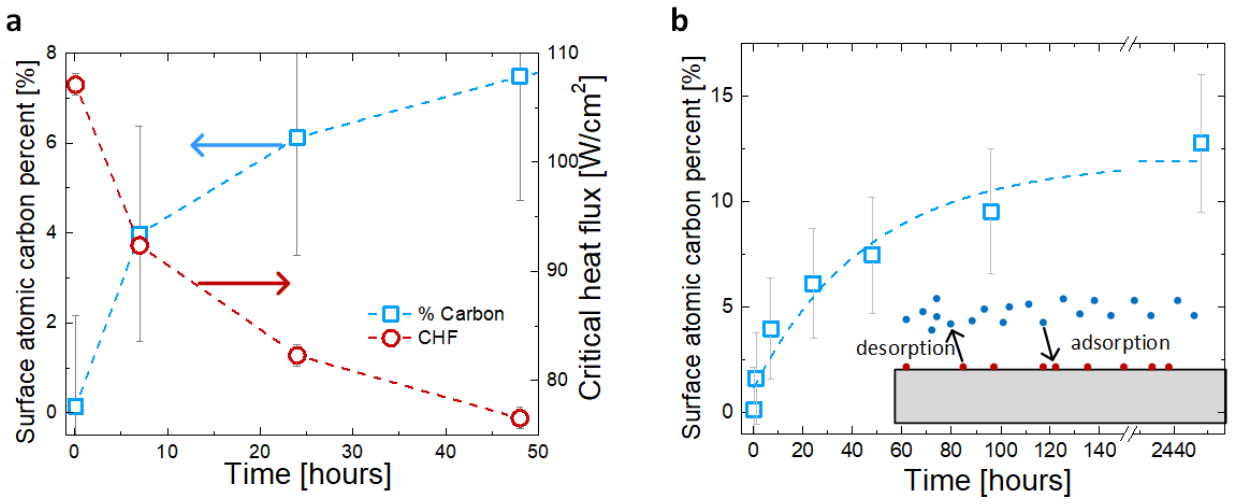

Figure 3.4. Analysis of the amount of adsorbed hydrocarbons. (a) The correlation between the amount of hydrocarbons on surfaces and pool boiling CHF values. (b) The amount of hydrocarbons on surfaces fitted with Langmuir adsorption kinetics in blue dashed line. The error bars for surface atomic carbon percent are based on the XPS measurement error and the evaluation uncertainty of the atomic percent from the spectra.

3.3 Oxidation of metallic surfaces during boiling

3.3.1 Introduction

The larger spread in CHF values of metallic surfaces than that of Si and SiO_2 (Figure 3.1), where some results show even higher values than Zuber's CHF prediction (125 W/cm^2 for water), cannot be explained by hydrocarbon adsorption. This is because hydrocarbon adsorption only lowers CHF values. The different methods of heat flux characterization and experimental measurement uncertainty could contribute up to ~20% CHF uncertainty [37]; yet, literature CHF values reported for Cu and Ni vary by a much larger range, up to 157 and 168 W/cm^2, respectively. In this chapter, we address the unexplained elevated CHF on metals by accounting for oxidation of metallic surfaces during boiling by testing Cu and Ni surfaces. Thermodynamically, both Cu and Ni are stable in pure, oxygen-free water; for example, the chemical stability of Cu in 400°C water has been experimentally demonstrated [98]. Nonetheless, the oxidation, *i.e.*, corrosion, of Cu and Ni in water has been reported because, in practice, metals can react with dissolved oxygen in water and outgassing hydrogen from the metal samples themselves or from the experimental apparatus [99-101]. In particular, Saadi et al. tested the corrosion of various metals in water at 75 and 95 °C; they found that a wide range of metals including Cu and Ni can corrode and form metal oxide nanostructures in hot water [99]. Because nanostructures on a boiling surface can increase CHF during pool boiling, the oxidation of metals and resulting formation of metal oxide nanostructures should be a key contributing factor in the spread in reported CHF values depending on the degree of oxidation.

3.3.2 Sample preparation

To investigate the oxidation of metallic surfaces during boiling and its effects on pool boiling heat transfer, we held Cu and Ni samples in saturated water for different periods of time (30 min, 7 h, and 24 h) before conducting pool boiling experiments. We prepared two different types of Cu and Ni samples that are commonly used for boiling research: (i) thin metal films coated on silicon wafers and (ii) bulk metal coupons. The thin-film samples were prepared by sputtering a 10 nm Ti adhesion layer followed by a 100 nm Cu or Ni layer on diced 650-μm-thick silicon chips (20 × 20 mm^2) covered with thermally grown 1 μm SiO_2 layers. Cu and Ni coupons were prepared by cutting metal sheets (813 μm-thick 110 copper and 483 μm-thick 200 nickel, McMaster-CARR) into 15 × 15 mm^2 squares with a waterjet. Metal coupons were smoothed with sandpaper (CarbiMet, Buehler) of up to 800 grit and subsequently polished with diamond suspensions of 1 and 3 μm (MetaDi Polycrystalline Diamont Suspensions, Buehler) to make the surface flat at the microscale. For convenience, we refer to each sample based on its duration in saturated water before boiling, material, and surface type; for example, a "24 h Ni thin film" means a Ni thin film surface left in saturated water for 24 h before boiling. Prior to boiling, all samples were cleaned in 2.0 M hydrochloric acid solution for 10 minutes to remove the native oxide and any organic contaminants.

3.3.3 Pool boiling results

Figure 3.5 shows the pool boiling curves of Cu and Ni samples. Both Cu thin films and Cu coupons showed apparent changes in pool boiling heat transfer associated with the duration (Δt) left in saturated water before boiling (Figure 3.5a and 3.5b). As Δt increased from 30 min to 24 h, pool boiling curves shifted upward to the left monotonically, representing

increasing CHF and HTC. The boiling curves of the Cu thin film samples (Figure 3.5a) showed more significant changes than the coupons. For example, CHF values of Cu thin films were 96.8, 120.9, and 133.7 W/cm^2 for Δt of 30 min, 7 h, and 24 h, respectively, which increased 38% from Δt of 30 min to 24 h. In addition, HTC values at CHF of Cu thin films increased from 24.5 to 54.4 kW/m^{2}K from Δt of 30 min to 24 h, a 122% increase in HTC. While less significant compared to Cu thin films, Cu coupons (Figure 3.5b) also showed increases in CHF and HTC at CHF values by 17.6 and 44%, respectively, as Δt increased from 30 min to 24 h.

Conversely, Ni surfaces exhibited relatively stable boiling heat transfer compared to Cu surfaces. CHF values of Ni thin films changed marginally (Figure 3.5c), *e.g.*, 99.0, 99.1, and 106.8 W/cm^2 for Δt of 30 min, 7 h, and 24 h, respectively. Changes in HTC values were also insignificant, which showed HTC at CHF values of 27.7, 22.0, and 27.1 kW/m^{2}K for 30 min, 7 h and 24 h, respectively. 30 min and 7 h Ni coupons followed the stable trend, where CHF values were 88.5 and 92.5 W/cm^2, respectively (Figure 3.5d). The 24 h Ni coupon, however, showed a noticeably higher CHF value of 121.3 W/cm^2.

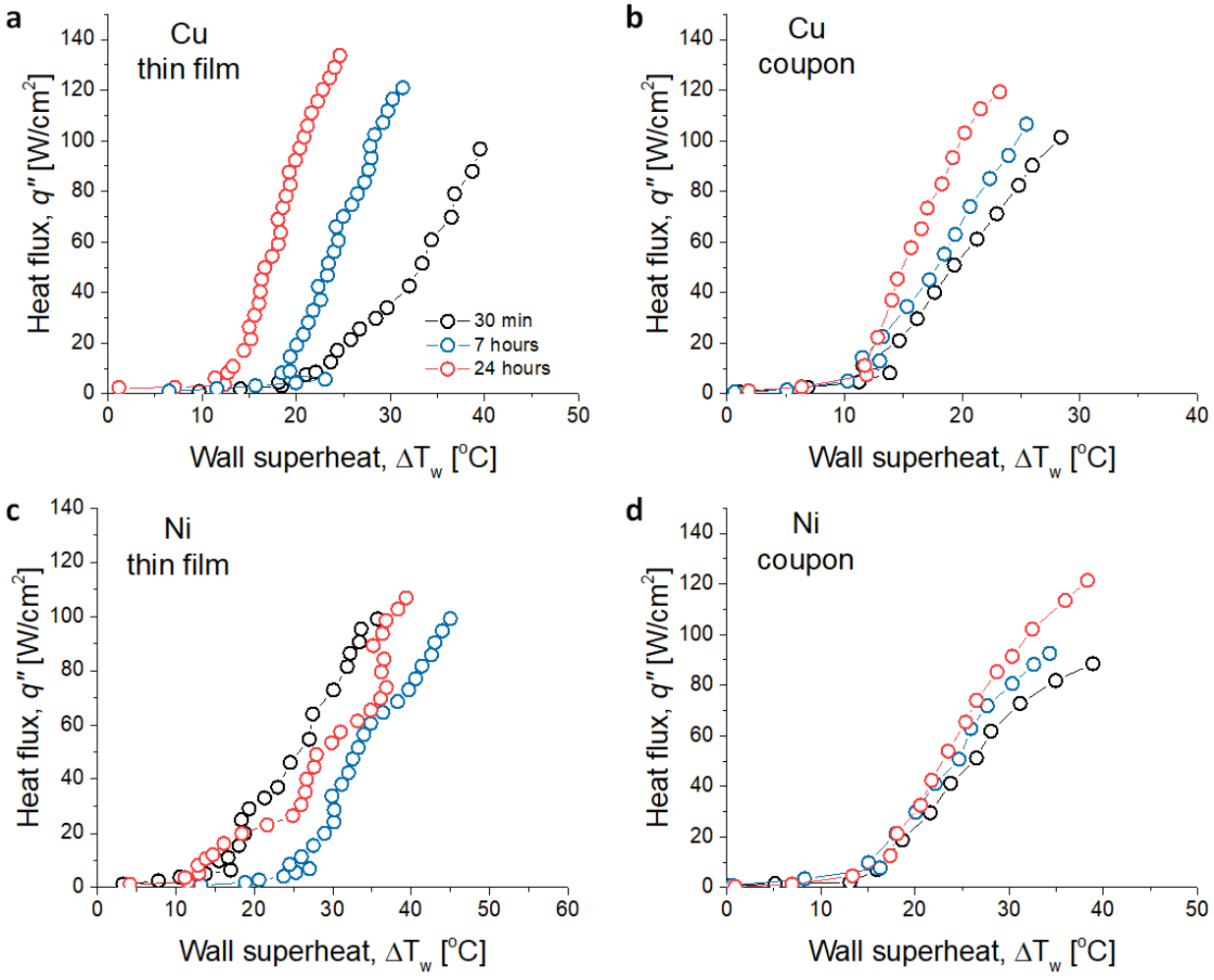

Figure 3.5. Pool boiling curves of (a) Cu thin film, (b) Cu coupon, (c) Ni thin film, and (d) Ni coupon surfaces. The surfaces were left in saturated water for different periods of time (30 minutes (black), 7 hours (blue), and 24 hours (red)) before measurements. The experimental uncertainty is smaller than the marker size in the plots.

In addition to boiling curves, we plotted CHF values (q''_{CHF}) normalized by the CHF of a corresponding material and type with 30 min Δt ($q''_{CHF,30min}$) as a function of Δt to investigate the relative change in CHF values (Figure 3.6). Along with Ni and Cu, we also plotted the results of chemically stable SiO_2 surfaces for reference. The plot shows clear increasing trends of CHF values of Cu surfaces as Δt increased. CHF values of Ni thin films

were as stable as those of SiO_2 reference surfaces, while the Ni coupon with 24 h Δt showed the relative change in CHF value as significant as Cu thin films.

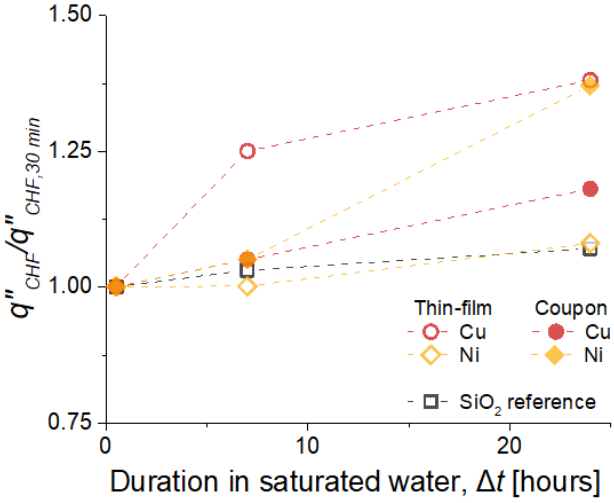

Figure 3.6. Relative change in CHF values as the duration in saturated water before boiling increases.

3.3.4 Change in morphology

The changes in CHF values shown in Chapter 3.3.3 indicate that surface material and structural properties were altered in a favorable way for pool boiling heat transfer as Δt increases. In this section, we investigate the change in surface morphology using scanning electron microscopy (SEM) and atomic force microscopy (AFM). Figure 3.7 shows the SEM images of Cu and Ni surfaces before and after boiling with different Δt. SEM images of surfaces before boiling show the initial surface conditions, where thin film surfaces represent fine grains resulting from sputtering and coupons show sandpaper scratches. Although the kinetics of nanostructure growth seems different for thin films and coupons, SEM images of Cu surfaces show growing nanostructures as Δt increased. The cube-like

shape indicates that the nanostructures are cuprous oxide (Cu_2O) rather than cupric oxide (CuO), where CuO usually exhibits sharp blade-like shapes [101]. Conversely, there are no noticeable changes on both Ni thin films and coupons.

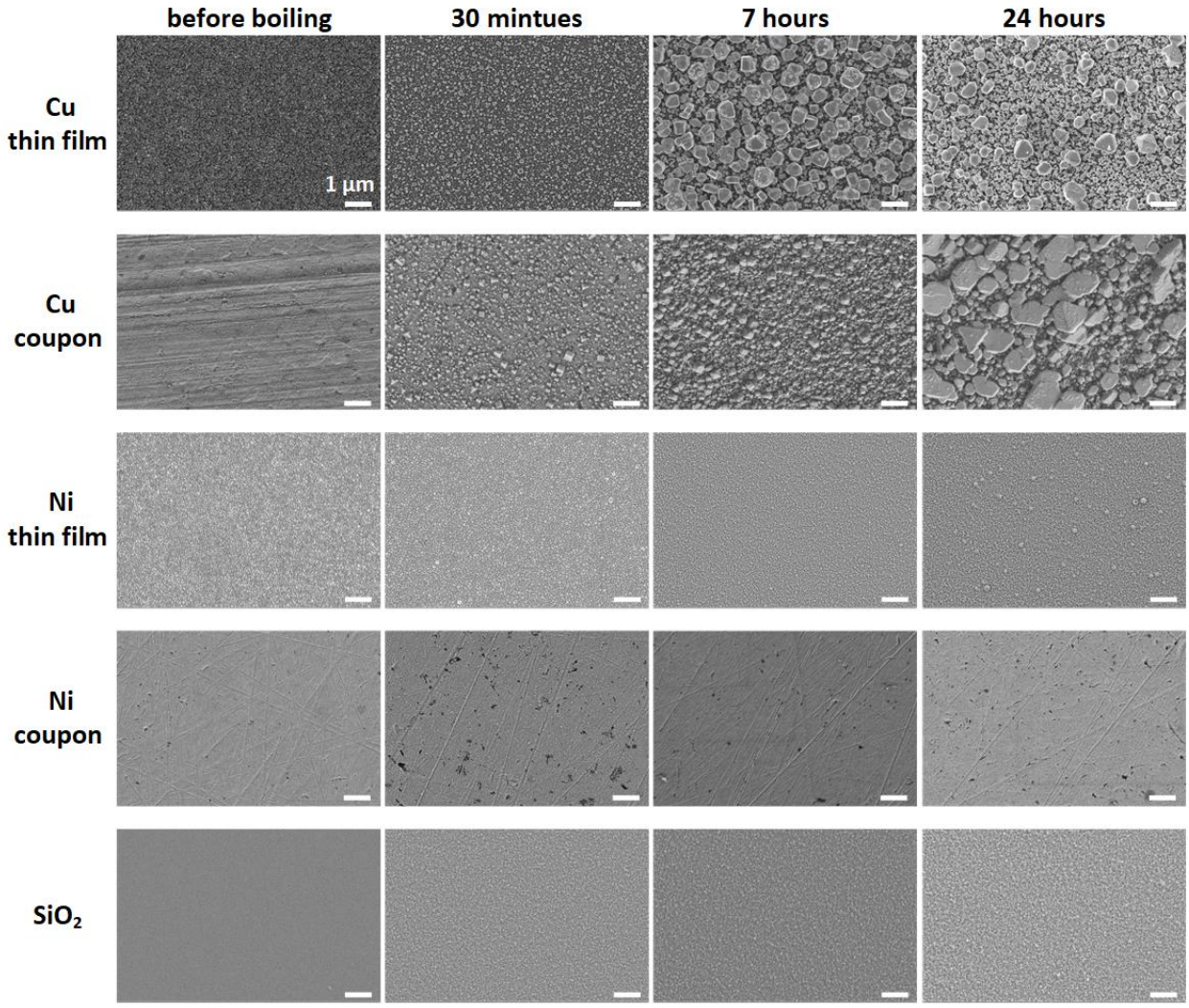

Figure 3.7. SEM images of Cu thin film, Cu coupon, Ni thin film, Ni coupon, and SiO_2 surfaces before and after boiling with different Δt. Cu shows growth in nanostructures as Δt increased, while changes in Ni surfaces are unnoticeable as in SiO_2 surfaces. All scale bars are 1 µm

For detailed analysis of surface morphology, we measured surface profiles using AFM and characterized their root mean square roughness (R_{sq}) and surface area ratio (r) (Figure 3.8), where r is defined as the ratio of actual surface area to the projected area. The change in R_{sq} and r of Cu increased with Δt similar to CHF. Specifically, Cu thin films showed significant increase in both R_{sq} and r, while Cu coupons showed a significant change in R_{sq} but the change in r remained less than 2.5%. This result implies that the shape of nanostructures on Cu thin films and coupons are different. A similar R_{sq} between thin films and coupons suggests the height of nanostructures was similar on both cases. The much higher r of thin films than coupons, on the other hand, indicates that the characteristic lateral size of nanostructures formed on thin films was smaller than coupons, so that the surface area increase on thin films was greater than that on coupons. This result was consistent with the three-dimensional profile images (Figure 3.8a) and SEM observation (Figure 3.7), where the 24 h Cu thin film showed relatively smaller lateral size of nanostructures than the nanostructures on the 24 h Cu coupon.

The morphology of Ni surfaces, as opposed to Cu, were stable for both thin films and coupons, which can explain the stable CHF values on Ni thin films. However, despite an observed change in CHF, the morphology of 24 h Ni coupon was not significantly changed as its CHF value. Although R_{sq} of 24 h Ni coupon increased slightly, the relative increase of CHF was more significant and comparable to that of Cu thin film sample, indicating that surface morphology is not the only important parameter governing CHF.

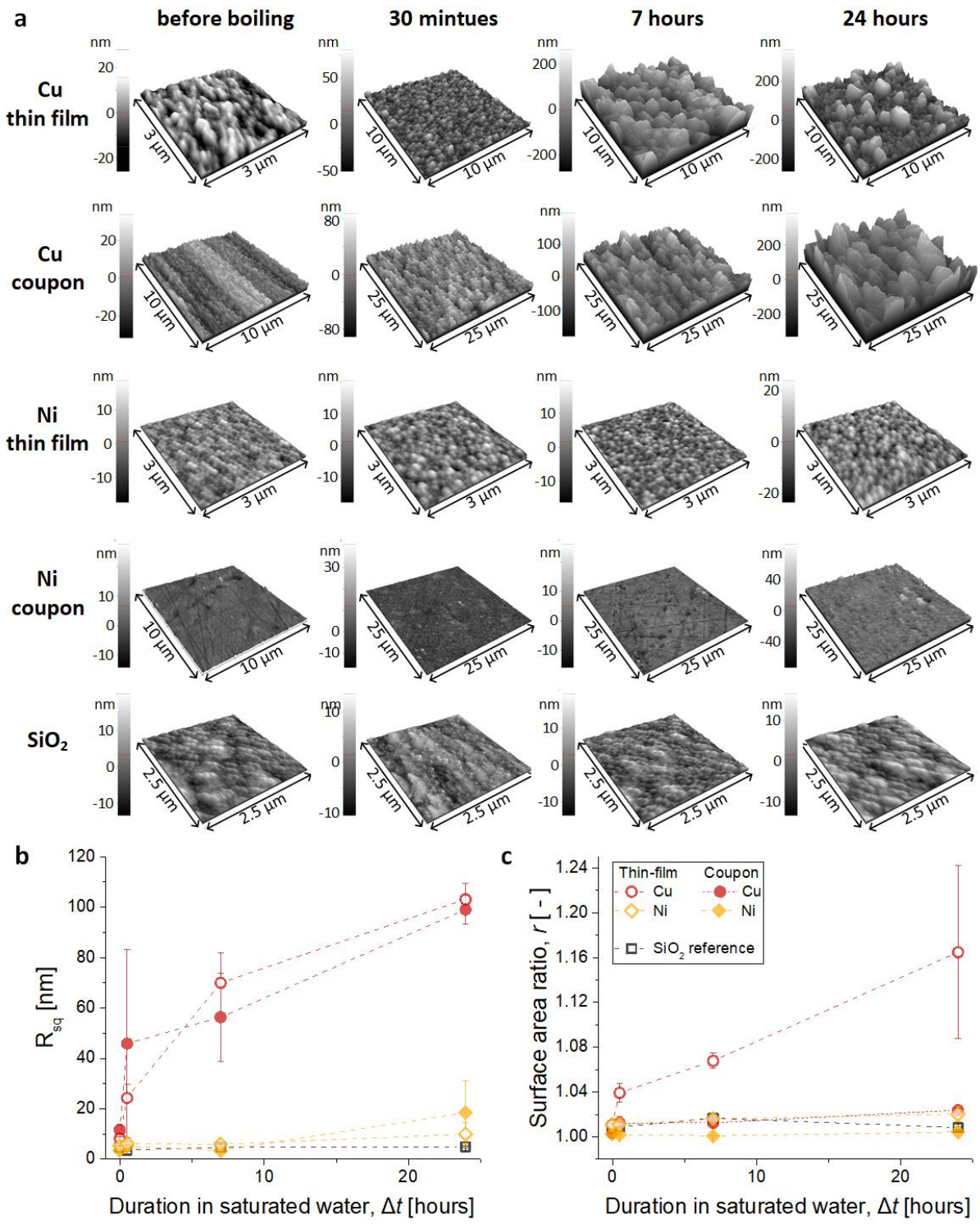

Figure 3.8. Three-dimensional surface profile measurements by AFM. (a) Three-dimensional profile images. Changes in root-mean-square roughness (b) and surface area ratio (c) as a function of Δt. Error bars represent standard deviations of measurements in three different spots.

3.3.5 Change in surface material composition

To observe the chemical oxidation states, we characterized surface material composition after boiling experiments using XPS equipped with a monochromated Al Kα X-ray source (Versaprobe II XPS, Physical Electronics). The angle between the surface plane and the analyzer was 45°. All samples were sputtered with argon ions in the XPS chamber before the measurements to remove carbonaceous species from surfaces. We collected principal Cu LMM Auger peaks on Cu thin films (Figure 3.9a) and coupons (Figure 3.9b) and plotted the normalized intensity as a function of kinetic energy (KE) of ejected Auger electrons. Here the kinetic energy was converted from the electron binding energy (BE) and the energy of incident X-ray ($h\nu = 1486.6$ eV), *i.e.*, $KE = h\nu - BE$. Both Cu thin films and coupons showed apparent shifts of Cu LMM peaks from Cu metal (~918.6 eV) to Cu_2O (~916.8 eV), indicating all Cu surfaces were oxidized in boiling water. In particular, the broad Cu LMM peak, spanning between Cu metal and Cu_2O peaks, of the 30 min Cu thin film represents the presence of CuO (~917.7 eV), which implies that the oxidation of Cu thin film surfaces transitions from CuO to Cu_2O as Δt increased.

The oxidation states of Ni thin films (Figure 3.9c) and Ni coupons (Figure 3.9d) were analyzed by the Ni2p spectra. While it is difficult to distinguish Ni2p multiplet-split peaks of Ni metal, Ni oxide (NiO), and Ni hydroxide ($Ni(OH)_2$), the clear appearance of NiO and $Ni(OH)_2$ satellite peaks on surfaces after boiling suggests that all Ni surfaces were oxidized in boiling water. Interestingly, the 24 h Ni coupon showed the presence of $Ni(OH)_2$ on the surface, whereas the other Ni surfaces showed the spectra of NiO only. This formation of $Ni(OH)_2$ could be originated from outgassed hydrogen from the Ni coupons. Bulk metals usually have dissolved hydrogens within their dislocation substructure [102], which can react with surface nickel to form $Ni(OH)_2$ when there is sufficient time for hydrogen to diffuse towards the surface. Considering that the 24 h Ni coupon also showed a notably

higher CHF value than the other Ni surfaces, we attributed this result to be related to the material property of $Ni(OH)_2$. The primary material property that affects the CHF is known to be surface wettability as discussed in Chapter 1.2.2. To see the wettability difference between NiO and $Ni(OH)_2$, we measured advancing and receding contact angles by infusing and withdrawing water through a syringe, respectively, on 7 h and 24 h Ni coupon surfaces (Figure 3.9e and 3.9f). While both surfaces showed extremely small receding contact angles ($\lesssim 5°$), the advancing contact angle on the 24 h Ni coupon ($\approx 25°$) was smaller than that of the 7 h Ni coupon ($\approx 40°$), indicating that better wettability of $Ni(OH)_2$ compared with NiO could contribute to the increase in CHF observed on the 24 h Ni coupon. Alternatively, the outgassing hydrogen, *per se*, could also affect the measured CHF value by disrupting the nucleation behavior and bubble dynamics. Understanding this higher CHF value found on $Ni(OH)_2$ than NiO warrants further investigation in future work.

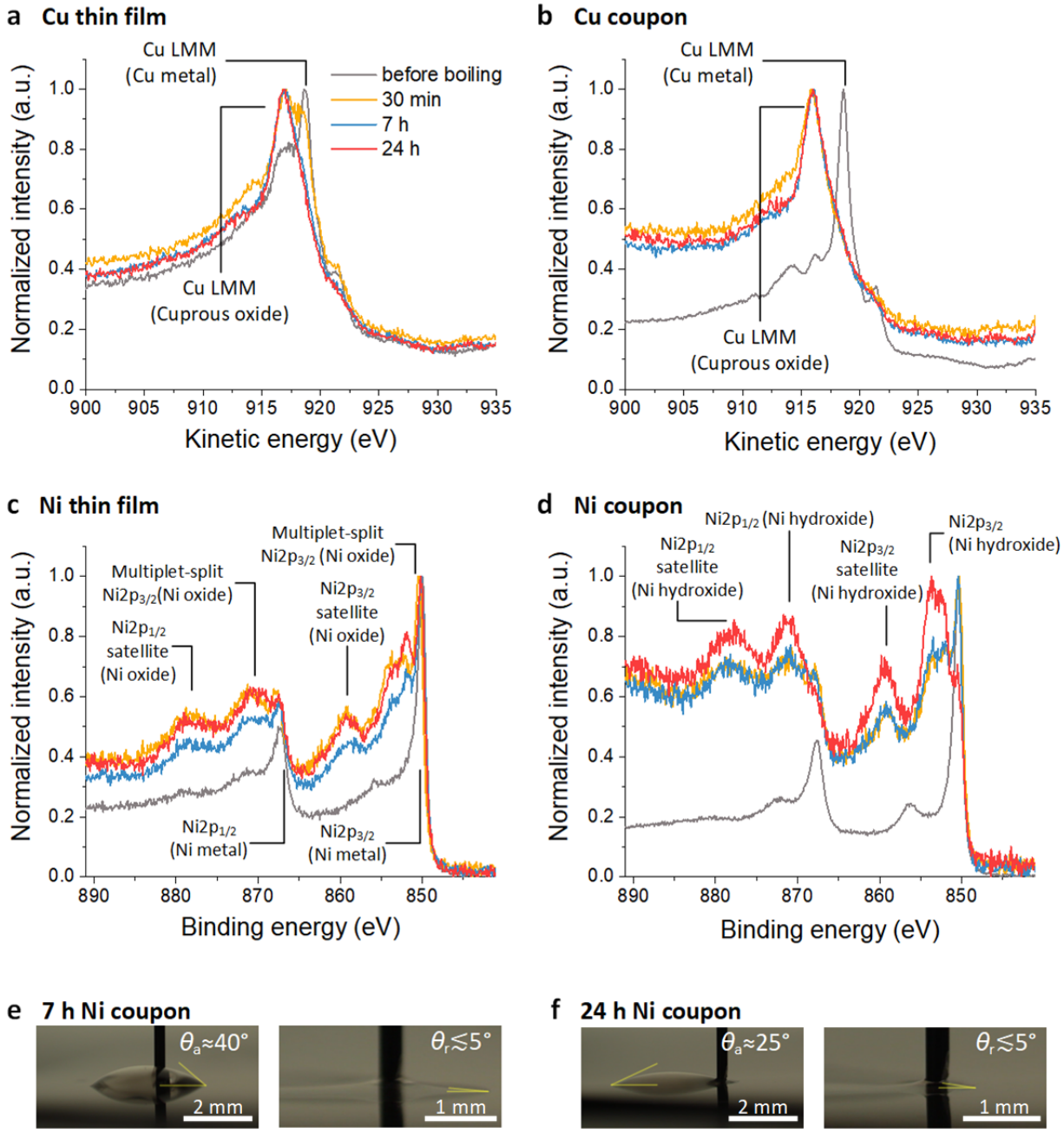

Figure 3.9. XPS analysis of Cu and Ni surfaces before and after boiling. (a, b) Cu LMM Auger peaks on Cu thin films on coupons. All Cu surfaces showed evidence of Cu_2O. The surface composition of 30 min Cu thin film was under transition from CuO to Cu_2O. (c, d) Ni2p peaks on Ni thin films and coupons. All Ni surfaces showed evidence of oxidation. Particularly, the surface of 24 h Ni coupon was found to be $Ni(OH)_2$, while the other Ni surfaces were NiO. (e, f) Advancing and receding contact angles of water on the 7 h and 24 h Ni coupon surfaces.

3.4 Summary

In Chapter 3.2, we addressed the discrepancy in experimentally measured CHF values of pool boiling of water on flat SiO_2 surfaces by accounting for hydrocarbon contamination on boiler surfaces. Flat SiO_2 surfaces were first cleaned with argon plasma then exposed to laboratory air for different periods of time before pool boiling experiments. Pool boiling results along with XPS analysis showed that the amount of adsorbed hydrocarbon on a surface increased with exposure time in air, which led to the decrease in CHF values due to decreased surface wettability. The measured CHF values (71 – 107 W/cm^2) fall within the spread of CHF values reported in literature (58 – 107 W/cm^2).

In Chapter 3.3, the even wider discrepancy in reported CHF values on flat Cu and Ni surfaces was addressed with the oxidation of metallic surfaces during boiling. We prepared 100 nm sputtered thin films and bulk metal coupons for Cu and Ni. Metallic surfaces were immersed in saturated water for different periods of time before pool boiling experiments. Along with pool boiling experiments, we analyzed the morphology of the surfaces using SEM and AFM and the chemical composition using XPS. The experimental results showed that pool boiling on metallic surfaces could be dependent on the samples' duration in saturated water. In the case of Cu surfaces, the roughness increased with residence time in saturated water by forming Cu_2O nanostructures, which led to an increase in CHF values due to the structural effects. The CHF and morphology of Ni surfaces were stable compared to Cu samples, with the exception of the 24 h Ni coupon, which exhibited a notably high CHF that could not be attributed to morphology. XPS analysis suggested the difference in CHF was likely due to a different surface chemical composition; the surface of the 24 h Ni coupon contained $Ni(OH)_2$, while the surfaces of the other Ni samples were primarily NiO. The reason why the $Ni(OH)_2$ surface exhibited a higher CHF than NiO surfaces could be attributed to its higher affinity for water, but this phenomenon requires further investigation. The

results of our study confirm that consistent control of samples' duration in saturated water is critical to achieve consistent measurements of pool boiling of water on metallic surfaces. In addition, we recommend that researchers characterize the morphology and chemical compositions of metallic surfaces before and after boiling to further investigate how changes in surface conditions affect the boiling heat transfer.

This work has important implications for understanding the spread in CHF values reported in literature and may serve as a guideline for the preparation of boiling surfaces to achieve consistent experimental results. In the following chapters, we used Si or SiO_2 surfaces cleaned with argon plasma to avoid unexpected alterations in CHF values caused by hydrocarbon contamination or surface oxidation.

Chapter Four

Unified descriptor for enhanced pool boiling CHF of hemi-wicking surfaces

4.1 Introduction

Enhancing CHF has been widely investigated to extend the operational limit and allow for larger safety margins for boiling systems [103, 104], by engineering boiling surface structures, *e.g.*, micropillar, microchannel, microridge, and nanowire [24, 27, 29, 46, 105]. Meanwhile, fundamental understanding of the mechanism for enhanced CHF on such structured surfaces has been a subject of debate for over half a century. A force balance model on a static bubble, for example, attributes the CHF enhancement on structured surfaces to the augmented three-phase contact line length along the structures [24]. This static force balance model proposes surface roughness, r, the ratio of actual surface area to the projected area, as a key structural property determining CHF that shows a reasonable correlation with experimentally measured CHF values [24, 34]. Another major group of CHF models attributes the CHF enhancement to the improved liquid rewetting by capillary

pumping through surface structures, *i.e.*, wickability. Structured surfaces that exhibit capillary-induced wicking are referred to as hemi-wicking surfaces. This capillary-induced flow occurs when the critical contact angle of a structured surface, $\theta_c = \cos^{-1}[(1-\varphi)/(r-\varphi)]$, becomes larger than the intrinsic contact angle, θ, where φ is the solid fraction at the solid-liquid interface. Most previous wickability-based models express the CHF of a hemi-wicking surface as the sum of the flat surface CHF, $q"_{\text{flat}}$, and an additional evaporation heat flux from a wicked liquid, $q"_{\text{w}}$, *i.e.*, $q"_{\text{CHF}} = q"_{\text{flat}} + q"_{\text{w}}$. In this case, $q"_{\text{w}}$ has been characterized by a separate experimental measurement such as capillary rise height [106], spreading or absorption of liquid droplets [25, 42], and volumetric wicking flux of a pendant droplet [26, 30]. In addition to CHF models based on the experimentally characterized $q"_{\text{w}}$, a semi-analytical CHF model has been proposed by characterizing the surface wickability using Darcy's law [27]. The model derived a property related to the surface wickability: $P_{\text{cap}}K_{\text{B}}$ that determines CHF values of hemi-wicking surfaces. Here P_{cap} is the capillary pressure and K_{B} is the effective permeability (a permeability that incorporates shear stress from the bottom surface).

While CHF models based on roughness and wickability show good agreement with the corresponding experimental data, neither r (Figure 4.1a) nor $P_{\text{cap}}K_{\text{B}}$ (Figure 4.1b) can provide a general correlation for CHF, if we combine the existing literature data on Si and SiO_2 hemi-wicking surfaces. Inconsistent surface preparation (as discussed in Chapter 3) or different boiling characterization methods across the literature may partly explain the discrepancy among different data sets [37, 107]; nonetheless, the unclear correlations of CHF values with roughness or wickability suggest that a single property, *i.e.*, roughness or wickability, is insufficient to describe CHF values of hemi-wicking surfaces. Recently, wickability-based models have included the structural effects on evaporation [108, 109]. In particular, an analytical model has proposed that the competition between evaporation and wicking fluxes associated with a varying dry area determines the CHF [109]. This model provides an important insight into the structural effects on evaporation; however, the model

is highly sensitive to empirical parameters that are difficult to measure, *e.g.*, bubble base diameter, accommodation coefficient, and thin-film thickness. Apart from roughness and wickability, a few studies have suggested that the boiling crisis is a critical phenomenon associated with stochastic bubble interactions [110-115]. Specifically, a machine learning-aided analysis has revealed that fundamental boiling parameters, *e.g.*, nucleation site density, bubble departure frequency, growth time, and bubble base radius, need to be taken into account for the stochastic bubble interactions and the resulting CHF [114]. The structural effects on those fundamental boiling parameters, however, need further investigation.

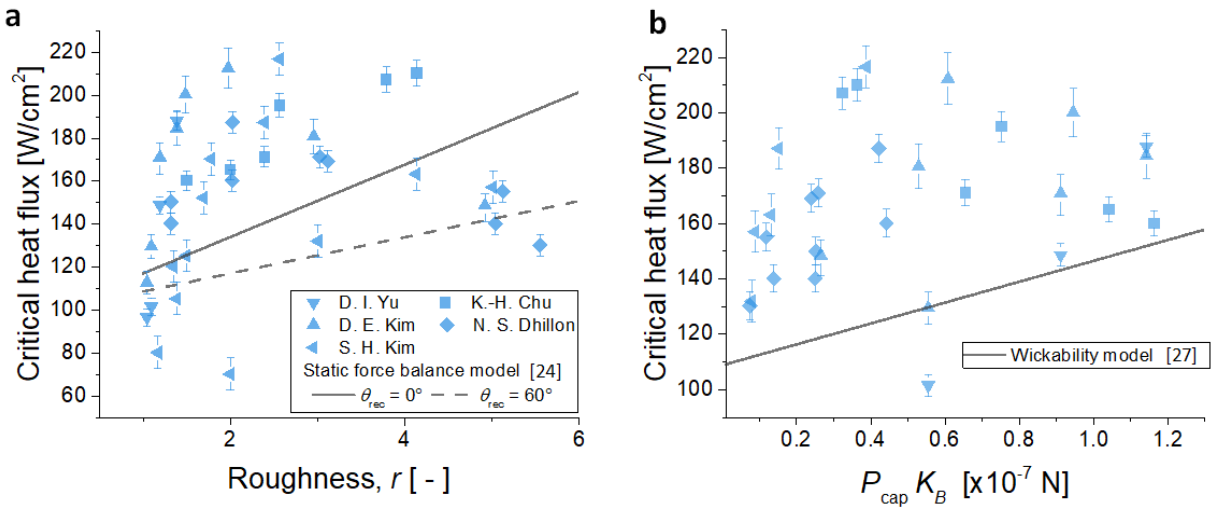

Figure 4.1. CHF data of hemi-wicking micropillar surfaces across the literature plotted with representative CHF models based on the (a) roughness r and (b) the product of capillary pressure and effective permeability $P_{cap}K_B$. The plots show no clear correlation between CHF values and r or $P_{cap}K_B$. Table 8.2 in Supplementary Information summarizes all of the data points in the plots.

In this chapter, we revisit the validity of previous roughness- and wickability-based CHF models using micropillar surfaces with systematically controlled roughness and wickability. By testing micropillar surfaces with a fixed roughness while varying wickability, and vice versa, we decoupled effects of each parameter on CHF values. Further, by leveraging

our experimental results and previous visualization studies of boiling bubbles [110, 116, 117], we derived a unified descriptor using a scaling analysis. CHF values of our experiments and the literature data confirmed the scaling analysis. This work provides physical insights into the structural effects on CHF, which can offer more general guidelines for the design of surface structures for high flux boiling applications.

4.2 Design and fabrication of micropillars

Roughness is quantified as the ratio of actual surface area (A_{actual}) to projected area (A_{prj}) by $r = \frac{A_{\text{actual}}}{A_{\text{prj}}} = 1 + \frac{\pi dh}{p^2}$ for square micropillar arrays, where d, h, and p are the diameter, height, and pitch (pillar center-to-center distance) of micropillars (Figure 4.2a). Wicking performance is characterized as a product of the capillary pressure P_{cap} and the effective permeability K_{B} according to the previous semi-analytical model for CHF [27]. The capillary pressure is evaluated based on the liquid meniscus shape around micropillars that minimizes free energy: $P_{\text{cap}} = -\Delta E/\Delta V$, where ΔE and ΔV are the change in the free energy and volume due to the liquid filling into a unit cell of the micropillar array, respectively (detailed expressions appear in Section 8.1 of the Supplementary Information) [109, 118]. We adopted the permeability correlation proposed by Yazdchi et al. [119], which combines the correlations developed by Gebart et al. [120], and Drummond and Tahir [121]. The permeability correlation proposed by Yazdchi et al., shows good agreement with experiments for the entire range of porosity ε [122], where the porosity is calculated as $\varepsilon = 1 - \frac{\pi d^2}{4p^2}$ for square micropillar arrays. Since this permeability K is developed for pillar arrays with unbounded top and bottom conditions, an additional term is required for our micropillar surfaces to account for the shear stress from the bottom surface. The effective permeability K_{B} accounting for viscous resistances from both the bottom surface and pillar

sidewalls, can be derived by solving the Brinkman equation with a no-slip condition at the bottom surface [109, 123].

$$K_{\mathrm{B}} = K\left[1 - \frac{\tanh(h\sqrt{\varepsilon/K})}{h\sqrt{\varepsilon/K}}\right]. \tag{4.1}$$

Detailed analysis on permeability is available in Section 8.2 of the Supplementary Information [109, 119, 122]. Previous representative CHF models describe the CHF value as a function of either roughness or surface wickability. In fact, roughness and wickability depend on each other to some extent. For example, with the increase in the structural packing density, roughness generally increases, while liquid wicking speed increases and then decreases, leading to an optimal value due to the competition between capillary pressure and viscous resistance [118]. Therefore, decoupling the effect of roughness or wickability on CHF has not been straightforward. To investigate the decoupled effects of roughness and wickability on CHF values during pool boiling, we systematically designed a set of micropillar surfaces with varying r for a specific $P_{\mathrm{cap}}K_{\mathrm{B}}$, and vice versa. For example, we designed four different micropillar arrays with a similar r~2.0, while changing $P_{\mathrm{cap}}K_{\mathrm{B}}$ from 0.81×10^{-7} to 1.22×10^{-7} N (Sample #1, 2, 3, and 7). Likewise, we designed three different micropillar arrays with a similar $P_{\mathrm{cap}}K_{\mathrm{B}}$ value of ~0.81×10^{-7} N, while changing r from 1.5 to 3.0 (Sample #1, 4, and 5). In addition, a micropillar arrays with extremely high r but low $P_{\mathrm{cap}}K_{\mathrm{B}}$ was included to investigate a wider range of structural effects. Table 4.1 summarizes the dimensions and properties of all samples. We fabricated micropillar arrays through photolithography and deep reactive-ion etching (DRIE) processes on silicon wafers. At the end of the fabrication process, we etched away a C_4F_8 DRIE passivation layer by O_2 plasma and deposited a 60 nm SiO_2 layer over the entire surface by atomic layer deposition to ensure uniform hydrophilicity over the surface. Details of the fabrication process are available in Section 8.3 of the Supplementary Information. Figure 4.2 shows SEM images of the fabricated micropillar arrays with the highest $P_{\mathrm{cap}}K_{\mathrm{B}}$ (Figure 2a, sample #3) and the highest r (Figure 2b, sample #6) among all samples.

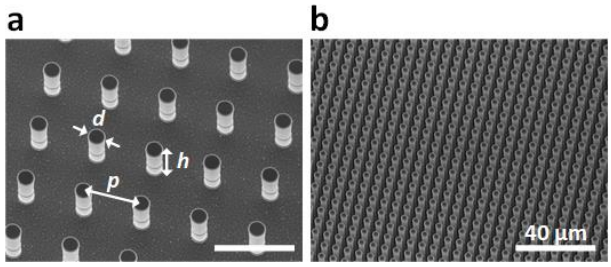

Figure 4.2. SEM images of micropillar arrays with dimensions of (a) d = 12 μm, p = 30 μm, h = 30 μm, and (b) d = 3 μm, p = 6 μm, h = 30 μm. The micropillar arrays in (a) and (b) have the highest $P_{cap}K_B$ and r, respectively, among seven different micropillar surfaces fabricated.

Table 4.1. Dimensions and properties of micropillar arrays. The roughness (r) and porosity (ε) are calculated as $r = 1 + \pi dh/p^2$ and $\varepsilon = 1 - \pi d^2/(4p^2)$, respectively. Two wicking properties are characterized, where $P_{cap}K_B$ and $P_{cap}K_Bh$ are related to the speed of the wicking liquid front and volumetric wicking flow rate, respectively.

Sample #	d [μm]	p [μm]	h [μm]	r [-]	ε [-]	$P_{cap}K_B$ [$\times 10^{-7}$ N]	$P_{cap}K_Bh$ [$\times 10^{-12}$ N·m]
1	4	20	30	1.9	0.968	0.81	4.56
2	7	25	30	2.0	0.938	1.05	6.06
3	12	30	30	2.2	0.874	1.22	7.24
4	3	23	30	1.5	0.987	0.75	3.41
5	11	23	30	3.0	0.820	0.86	6.26
6	3	6	30	8.8	0.804	0.21	4.56
7	8	30	30	1.8	0.944	1.20	6.25

4.3 Boiling results

For each micropillar geometry, we measured CHF values with two different samples. Figure 4.3 shows the average CHF values as a function of r and $P_{\mathrm{cap}}K_{\mathrm{B}}$. Our boiling results show no clear correlation between CHF values and r and $P_{\mathrm{cap}}K_{\mathrm{B}}$, which confirms that the discrepancy between the literature data and previous CHF models (Figure 4.1) cannot be attributed to inconsistent surface conditions or boiling characterization methods across the literature only. Rather, the results directly show that CHF values on hemi-wicking surfaces cannot be described by either r or $P_{\mathrm{cap}}K_{\mathrm{B}}$ alone. Interestingly, however, CHF values generally increase with either r or $P_{\mathrm{cap}}K_{\mathrm{B}}$ when the other parameter is fixed, indicating that r and $P_{\mathrm{cap}}K_{\mathrm{B}}$ may have separate effects on CHF values. In Figure 4.3a, for example, the micropillar arrays with a similar r value ($r \approx 2$ for sample #1, 2, 3, and 7, colored in red) shows an increase in CHF values as $P_{\mathrm{cap}}K_{\mathrm{B}}$ increases except for one case (sample #7). Likewise, we found higher CHF values for micropillar arrays with higher r when $P_{\mathrm{cap}}K_{\mathrm{B}}$ remained similar ($P_{\mathrm{cap}}K_{\mathrm{B}} \approx 0.8 \times 10^{-7}$ N for sample #1, 4, and 5, colored in blue) as shown in Figure 4.3b.

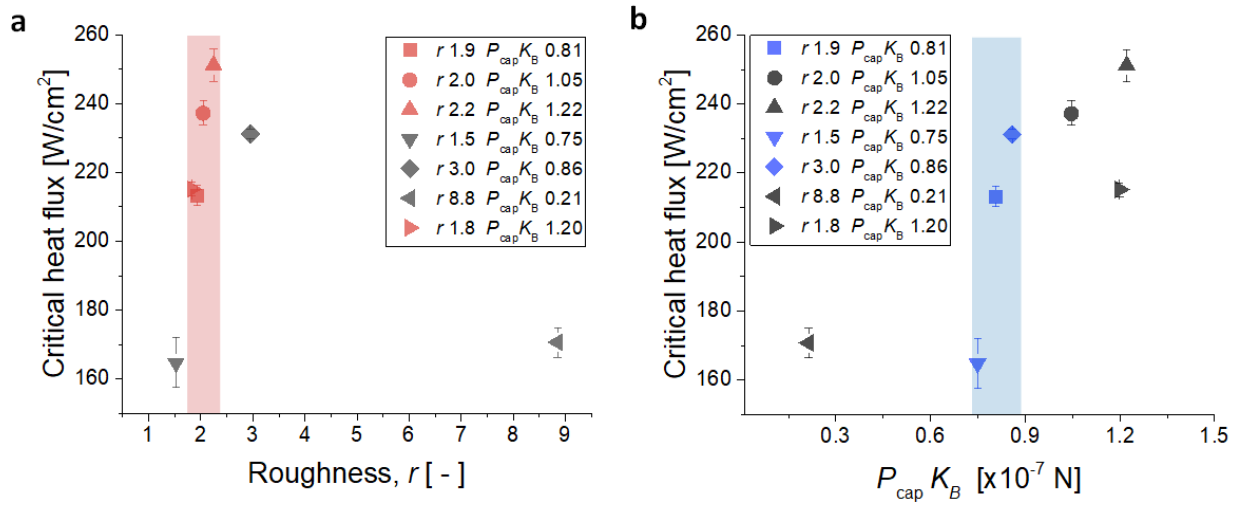

Figure 4.3. CHF values of micropillar arrays as a function of (a) r and (b) $P_{cap}K_B$. Data points show the average CHF values measured from two different samples for each pillar array. CHF values showed no clear correlation with both parameters. (a) For micropillar arrays with a similar r (colored in red), however, higher $P_{cap}K_B$ generally resulted in higher CHF values. (b) Likewise, higher r resulted in higher CHF values for micropillar arrays with a similar $P_{cap}K_B$ (colored in blue). The error bars were deviations of measurements on each sample from the average.

4.4 Scaling approach

Although it is possible to understand the structural effects using a varying-dry-area model [109], this approach is highly sensitive to several empirical parameters such as bubble base diameter, accommodation coefficient, and thin-film thickness, which makes it challenging to directly assess the structural effects shown in our experiments. Alternatively, we applied a scaling approach to interpret our experimental results with minimal uncertainties from the empirical parameters. Considering that the contribution of convective heat transfer by single-phase liquid to the total boiling heat flux is insignificant near CHF [124, 125], CHF can be expressed as $q"_{CHF} \approx \rho_l h_{fg} N" f V_{l,CHF}$, where ρ_l, h_{fg}, $N"$, f, and $V_{l,CHF}$ are the density of liquid, latent heat of vaporization, bubble nucleation site density, bubble departure frequency, and volume of evaporating liquid per bubble at CHF, respectively. Since structural

dimensions of micropillars do not affect the nucleation site density significantly near CHF [108], we consider the nucleation site density roughly constant and scale the heat flux near CHF as $q"_{\mathrm{CHF}} \sim f V_{\mathrm{l,CHF}}$.

4.4.1 Bubble departure frequency and thin film density

The bubble departure frequency f describes how quickly bubbles nucleate and depart from a boiling surface. Specifically, if we assume bubbles depart at a characteristic volume V_{d}, at which buoyancy overcomes the surface tension force and drag force, V_{d} can be expressed as $V_{\mathrm{d}} = q"_{\mathrm{ev}} \frac{\tau_{\mathrm{d}} A_{\mathrm{b}}}{\rho_{\mathrm{v}} h_{\mathrm{fg}}}$, where $q"_{\mathrm{ev}}$, τ_{d}, A_{b}, and ρ_{v} are evaporation heat flux under a bubble, bubble departure period, bubble base area, and the density of vapor, respectively [126]. Assuming the thermophysical properties of water are constant, the departure frequency scales as $f = \frac{1}{\tau_{\mathrm{d}}} \sim q"_{\mathrm{ev}}$, *i.e.*, surface structures with stronger evaporation can have higher bubble departure frequency. Given the high thermal conductivity of silicon, we can expect that dense micropillar arrays may provide effective heat transfer for evaporation. In addition, when bubbles nucleate on micropillar surfaces (Figure 4.4a), the three-phase contact line pins at the top of micropillars and forms thin liquid films around the micropillars (Figure 4.4b – 4.4d). This thin film provides efficient heat transfer paths through their thin thickness (≤ 1 μm). Since the density of thin films (ξ) (shaded red regions in Figure 4.4b (top view) and 4.4c (cross-section view)) scales with the density of micropillars, *i.e.*, $\xi \approx \frac{\pi d \delta_{\mathrm{tf}}}{p^2} \sim \frac{d \delta_{\mathrm{tf}}}{p^2}$, where δ_{tf} is the thin-film thickness threshold, the evaporation heat flux is expected to scale with the density of the thin film. Here the thin film density ξ is similar to roughness r, where both capture the structural packing density, but ξ is not dependent on the micropillar height. To confirm the scaling between the thin film density and evaporation heat flux, we modeled the thin-film evaporation in the unit cell of micropillar array (Figure 4.4c).

The heat transfers from the boiling surface at the wall temperature (T_w) to the vapor bubble at the saturation temperature (T_{sat}) passing a silicon micropillar and bulk liquid water. Due to the orders of magnitude higher thermal conductivity of silicon ($k_{Si} \approx 113$ W/(mK) at 100 ℃) than that of water ($k_w \approx 0.68$ W/(mK)), we simplified the heat transfer path to be a one-dimensional resistance network including a micropillar and the surrounding thin liquid film. The conduction resistance through a micropillar is $R_{Si} = \frac{4h}{\pi d^2 k_{Si}}$.

The thin liquid film region around the pillar top provides an efficient heat transfer path because of its microscale thickness. In this calculation, we define the upper bound of this highly evaporative region thickness δ_{tf} (accounting for over 50% of the total evaporative flux) as 1 μm [109, 127]. When the thickness of liquid film is close to that of a few molecules, on the other hand, attractive forces between molecules in the liquid and solid surface form a non-evaporating film known as the adsorbed film. In the case of water, the thickness of the adsorbed film (δ_{ads}) is ~ 0.3 nm [128]. Therefore, we define the thin-film region as the liquid film with a thickness 0.3 nm $\leq \delta \leq$ 1 μm. We model the meniscus shape as spherical with the contact angle (θ) at the micropillar top surface, which results in the liquid film thickness δ as a function of the distance from the micropillar top z: $\delta(z) = \frac{s}{2} - \sqrt{\frac{s^2}{4} - z^2 - zs\tan\theta}$, where s is the spacing between pillars, *i.e.*, $s = p - d$ (Figure 4.4d). The experimentally obtained receding contact angle of water on a SiO_2 surface is ~10° [107]. The thin-film resistance is calculated by integrating the conduction resistances of infinitesimal thin-liquid film slices that are in parallel along the thin-film profile as $R_{tf} = \left[2k_w\pi \int_{z_{ads}}^{z_{tf}} \frac{(\delta+\frac{d}{2})\sqrt{1+\left(\frac{d\delta}{dz}\right)^2}}{\delta} dz\right]^{-1}$ [129], where z_{tf} and z_{ads} are z values corresponding to a thin-film thickness threshold (δ_{tf}) and adsorbed layer thickness (δ_{ads}), respectively.

The interfacial resistance is estimated using the Schrage equation as $R_{\text{int}} = \frac{1}{A_{\text{int}}}\left(\frac{2-\chi}{2\chi}\right)\left(\frac{T_{\text{v}}v_{\text{lv}}}{h_{\text{fg}}^2}\right)\left(\frac{2\pi\bar{R}T_{\text{v}}}{\bar{M}}\right)^{1/2}\left(1-\frac{P_{\text{v}}v_{\text{lv}}}{2h_{\text{fg}}}\right)^{-1}$, where A_{int} and χ are the thin-film interfacial area and accommodation coefficient, respectively. The accommodation coefficient is set to 0.03 in our calculations [130]. T_{v}, P_{v}, and v_{lv} are the vapor temperature, vapor pressure, and specific volume difference between the vapor and liquid phases, respectively. $\bar{R}$ is the universal gas constant (8.314 J/(molK)) and $\bar{M}$ is the molar mass of water (0.01801 kg/mol). The interfacial area A_{int} is calculated by the surface area of revolution: $A_{\text{int}} = 2\pi\int_{z_{\text{ads}}}^{z_{\text{tf}}}\left(\frac{d}{2}+\delta(z)\right)\sqrt{1+\left(\frac{d\delta}{dz}\right)^2}\,dz$. The effective thermal resistance (R_{tot}) in one unit cell is then evaluated as $R_{\text{tot}} = R_{\text{Si}} + R_{\text{tf}} + R_{\text{int}}$, where the evaporation heat flux through one unit cell is $q"_{\text{ev}} = \frac{T_{\text{w}}-T_{\text{sat}}}{R_{\text{tot}}p^2}$. The wall superheat $T_{\text{w}} - T_{\text{sat}}$ is set to 30°C for this calculation. We evaluated $q"_{\text{ev}}$ and ξ for micropillar arrays with a fixed height of 30 μm, while changing the pitch for pillar diameters of 5, 7, and 10 μm. The resulting plot of $q"_{\text{ev}}$ normalized by the CHF value on a flat surface ($q"_{\text{flat}} = 99.45$ W/cm^2) as a function of ξ (Figure 4.4e) monotonically increase while the derivative of the function decreases. Based on the shape of the curves, we scale the evaporation heat flux as $q"_{\text{ev}} \sim \xi^{\text{n}}$ with $0 < n < 1$. Note that we do not determine the value of the exponent n based on the modeling results, because the model depends on empirical parameters such as contact angle, accommodation coefficient, and thin-film thickness. Instead, we leave the exponent to be determined by the experimental results. Consequently, the departure frequency can be scaled to yield

$$f \sim q"_{\text{ev}} \sim \xi^{\text{n}}, \text{ where } 0 < n < 1 \tag{4.2}$$

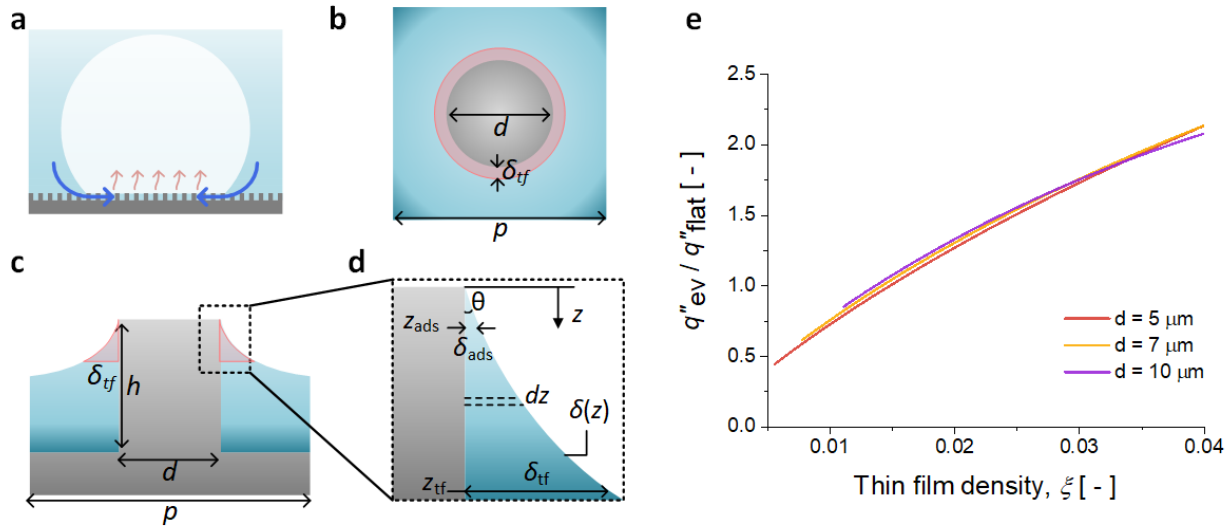

Figure 4.4. Structural effects on evaporation and rewetting under a boiling bubble on a hemi-wicking surface. (a) A schematic of a bubble nucleating on a hemi-wicking surface. Evaporation (red arrows) occurs from a liquid layer at the bubble base, while capillary-driven wicking (blue arrows) supplies the liquid from the circumference to the center of bubble base. (b) Top-view and (c) cross-section view schematics of thin-film evaporation in the unit cell of micropillar array. Shaded red area represent the thin-film region. (d) A magnified view of the thin-film region. (e) Evaporation heat flux normalized by the CHF value on a flat surface (q''_{ev}/q''_{flat}) as a function of thin film density, $\xi \sim d\delta_{tf}/p^2$. The plot shows an increase in evaporation heat flux with thin film density, *i.e.*, $q''_{ev} \sim \xi^n$ with $0 < n < 1$.

4.4.1.1 Scale analysis of evaporation heat flux and thin film density

In this section, we explain the validity and limitation of scaling relationship between the evaporation heat flux and the thin film density, *i.e.*, $q"_{ev} \sim \xi^n$. For typical dimensions of silicon micropillar arrays used for a boiling surface, *e.g.*, ~3 μm ≤ d ≤ ~80 μm and ~10 μm ≤ h ≤ ~30 μm, we performed an order of magnitude analysis of the thermal resistances: R_{Si}, R_{tf}, and R_{int}. The thin film resistance R_{tf} is not highly dependent on micropillar dimensions and its order of magnitude ranges from $\mathcal{O}(10^2)$ to $\mathcal{O}(10^3)$ K/W. The conduction resistance through a micropillar R_{Si} scales as $R_{Si} \sim \frac{h}{d^2 k_{Si}}$, which results in an order of magnitude of R_{Si} ranging from $\mathcal{O}(10^2)$ to

$\mathcal{O}(10^4)$ K/W. Lastly, the interfacial resistance can be simplified as $R_{\mathrm{int}} = \frac{K}{A_{int}}$, where K is the thermo-physical property of water independent of surface structures $K = \left(\frac{2-\chi}{2\chi}\right)\left(\frac{T_{\mathrm{v}} v_{\mathrm{lv}}}{h_{\mathrm{fg}}^2}\right)\left(\frac{2\pi \bar{R} T_{\mathrm{v}}}{\bar{M}}\right)^{1/2}\left(1 - \frac{P_{\mathrm{v}} v_{\mathrm{lv}}}{2h_{\mathrm{fg}}}\right)^{-1}$. Depending on micropillar dimensions, the order of magnitude of R_{int} is between $\mathcal{O}(10^4)$ and $\mathcal{O}(10^5)$ K/W. The orders of magnitude of thermal resistances show that R_{tf} is negligible and R_{int} is dominant in most cases. Therefore, we scaled $R_{\mathrm{tot}} \sim R_{\mathrm{int}} \sim \frac{1}{A_{\mathrm{int}}}$, which led to $q''_{ev} = \frac{\Delta T_{\mathrm{w}}}{R_{\mathrm{tot}} p^2} \sim \frac{1}{A_{\mathrm{int}} p^2} \sim (\frac{d\delta_{\mathrm{tf}}}{p^2})^{\mathrm{n}} \sim \xi^{\mathrm{n}}$, where the exponent *n* works as a fitting parameter for a given experimental data set considering the uncertainty of the accommodation coefficient and thin film thickness threshold. This scaling, however, can be limited if R_{Si} becomes comparable to R_{int} when the aspect ratio of a micropillar is high (small *d* and tall *h*). For example, in the extreme case, when *d*, *p*, and *h* are 3, 30, and 30 μm, respectively, $R_{\mathrm{Si}} \sim 0.4 R_{\mathrm{int}}$ as shown in Figure 4.5a at $d/p = 0.1$. In this case, approximating $R_{\mathrm{tot}} \sim R_{\mathrm{int}}$ will underestimate the total resistance by 40%. In most cases in Figure 4.5a, however, shows $R_{\mathrm{int}}/R_{\mathrm{Si}} \geq 10$, where approximating $R_{\mathrm{tot}} \sim R_{\mathrm{int}}$ can provide a reasonable estimation. The ratio of interfacial resistance to pillar conduction resistance becomes larger when copper (Cu) is used, which is another common material used for a boiling surface (Figure 4.5b). For example, in the extreme case of *d*, *p*, and *h* are 3, 30, and 30 μm, respectively, $R_{\mathrm{Cu}} \sim 0.1 R_{\mathrm{int}}$, indicating $R_{\mathrm{tot}} \sim R_{\mathrm{int}}$ will underestimate the total resistance only by 10%.

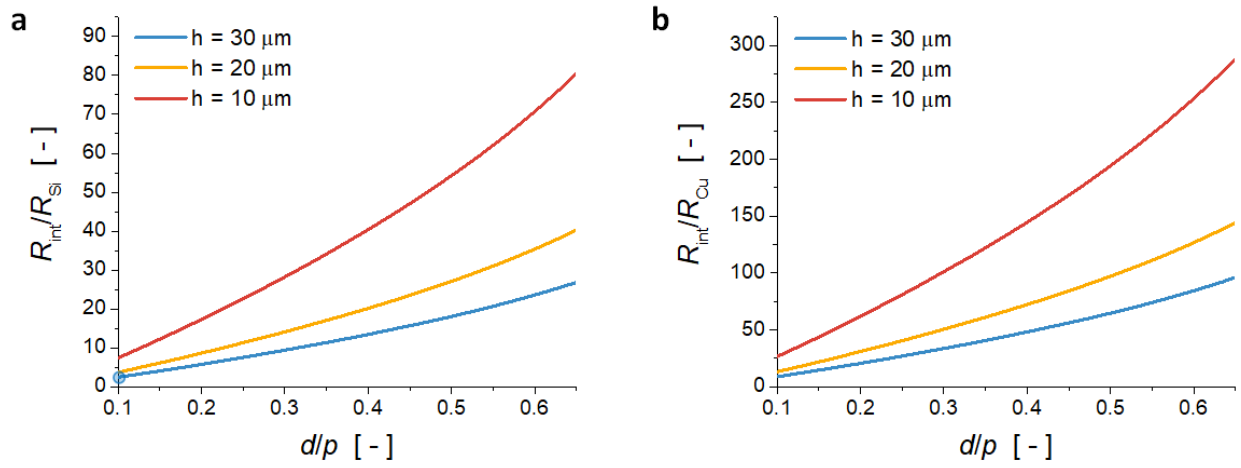

Figure 4.5. The ratio of interfacial resistance to conduction resistance through a pillar. (a) For a silicon pillar and (b) a copper pillar. The plot is created by calculating R_{int} and R_{Si} for a constant d of 3 μm while varying p for three different heights.

4.4.2 Maximum volume of evaporating liquid and volumetric wicking rate

Past synchrotron X-ray visualization of boiling bubbles on hemi-wicking surfaces has revealed that hemi-wicking surfaces maintain liquid layers under the boiling bubbles (as shown in Figure 4.4a) until a heat flux reaches CHF, where the bubble base dries out leading to the boiling crisis [117]. Combining this observation with stochastic bubble interaction models [110, 114], we presume that hemi-wicking surfaces may delay the boiling crisis by maintaining a liquid layer under bubbles. Once the wicked liquid layer dries out, however, much more dry areas are suddenly created by the stochastic bubble interactions whereby the boiling crisis occurs. This capability of maintaining the liquid layer depends on the volumetric wicking flow rate. Therefore, we scale the volume of evaporating liquid at CHF ($V_{l,CHF}$) as

$$V_{\mathrm{l,CHF}} \sim P_{\mathrm{cap}} K_{\mathrm{B}} h, \tag{4.3}$$

where $P_{\mathrm{cap}} K_{\mathrm{B}} h$ dictates the volumetric wicking flow rate of a hemi-wicking surface and h is the thickness of wicked liquid layer, *i.e.*, micropillar height [131]. Note that there can be exceptional cases such as hemi-wicking surfaces with artificial cavities, *e.g.*, microtube structures that we are going to discuss in Chapter 5, where the extensive bubble coalescence due to high nucleation site density can limit the liquid supply, before capillary wicking becomes limiting, and trigger the boiling crisis [132]. Combining Equation 4.2 and 4.3, we obtain a unified descriptor of the CHF,

$$q''_{\mathrm{CHF}} \sim \xi^{\mathrm{n}} P_{\mathrm{cap}} K_{\mathrm{B}} h. \tag{4.4}$$

4.4.3 Scaling results

Figure 4.6a shows our CHF data as a function of the unified descriptor $\xi^{\mathrm{n}} P_{\mathrm{cap}} K_{\mathrm{B}} h$. The plot shows a clear positive correlation between our CHF data and $\xi^{\mathrm{n}} P_{\mathrm{cap}} K_{\mathrm{B}} h$, where n of 0.46 showed the best fit with our dataset. We also included literature data in Figure 4.6b using the same n, which confirms the positive linear relationship in a broader range. The exponent n, as previously discussed, depends on experimental and environmental parameters, so it may differ for different literature data sets. Nonetheless, the improved correlation between CHF values with $\xi^{\mathrm{n}} P_{\mathrm{cap}} K_{\mathrm{B}} h$ (Figure 4.6) when compared to the correlations with r or $P_{\mathrm{cap}} K_{\mathrm{B}}$ alone (Figure 4.1) supports our scaling analysis; that is, the combined effect of thin film density and volumetric wicking rate affect CHF values by enhancing bubble departure frequency and delaying the growth of dry area, respectively. In fact, the scaling-driven descriptor $\xi^{\mathrm{n}} P_{\mathrm{cap}} K_{\mathrm{B}} h$ has the combined effects of previous roughness- and wickability-based models, which becomes more obvious by rearranging the parameters as $(\xi^{\mathrm{n}} h)(P_{\mathrm{cap}} K_{\mathrm{B}})$. Here $\xi^{\mathrm{n}} h$ is a parameter similar to roughness r, where their roles for enhanced CHF are essentially

the extension of contact line, and $P_{cap}K_B$ is the key parameter used in the wickability-based model. This explains why the previous models could work for specific data sets. The roughness-based model could work when the effect of extended contact line length is dominant, while the wickability-based model could work better if the wickability effect is dominant.

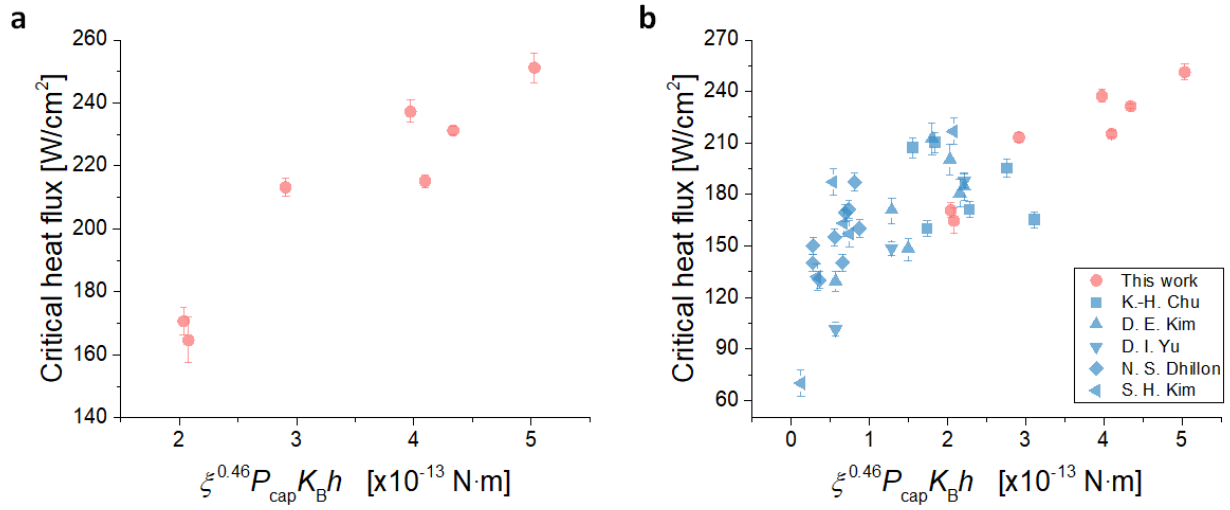

Figure 4.6. Experimentally measured CHF values versus $\xi^{0.46}P_{cap}K_Bh$, where 0.46 is the exponent that fits best for our measurement. (a) CHF scaling results with our data and (b) including the literature data.

4.4.3.1 Sensitivity of thin film density exponent n

The ξ^n term was derived from the scaling analysis with the evaporation heat flux and thin film density, where n of 0.4 showed the best fit for the model when the thin-film thickness, accommodation coefficient, and receding contact angle values were defined as 1 μm, 0.03, and 10°, respectively. Our experimental CHF data, on the other hand, showed the best fit with n of 0.46. In Figure 4.7, we plotted our CHF data as a function of $\xi^nP_{cap}K_Bh$ with three

different n values of 0.25, 0.46, and 0.7 to see the sensitivity of exponent value on the CHF – $\xi^{\mathrm{n}} P_{\mathrm{cap}} K_{\mathrm{B}} h$ correlation. The plots show that, as n value increases, the weight of thin film density values on the correlation increases. This dependency can be found clearly when we compare $\xi^{\mathrm{n}} P_{\mathrm{cap}} K_{\mathrm{B}} h$ values of the surfaces with the smallest (sample #4, r1.5 $P_{\mathrm{cap}} K_{\mathrm{B}}$0.75) and highest (sample #6, r8.8 $P_{\mathrm{cap}} K_{\mathrm{B}}$0.21) roughness. Here we can consider $\xi \sim r$ as the micropillar height is constant. We expect this n value can change for different experimental environments that can affect the evaporation heat flux such as the degree of surface contamination and actual contact angle. This uncertainty associated with experimental conditions is even found on CHF values of flat surfaces as we discussed in Chapter 3. Nonetheless, all three plots show generally a positive correlation between CHF and $\xi^{\mathrm{n}} P_{\mathrm{cap}} K_{\mathrm{B}} h$, indicating both thin film density and volumetric wicking rate are important for CHF.

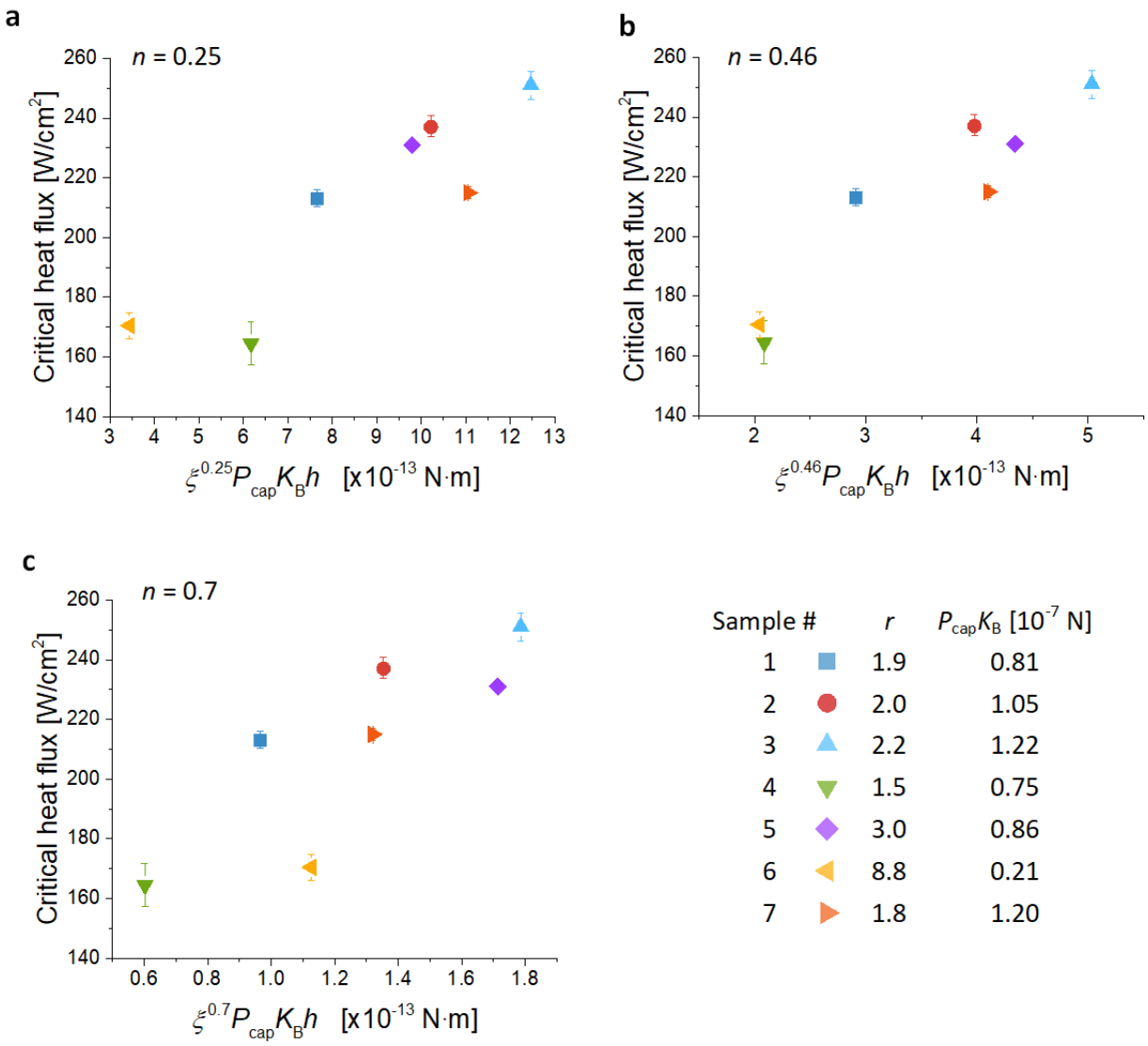

Figure 4.7. Sensitivity of exponent n on the CHF $-\xi^{n}P_{cap}K_{B}h$ correlation.

4.5 Conclusions

In this chapter, we showed that existing CHF correlations which used roughness or wickability as a single descriptor were limited to specific data sets. To investigate the effects of roughness and wickability on CHF values independently, we designed micropillar arrays with a fixed r while varying $P_{cap}K_{B}$, and vice versa. The experimentally measured CHF values

on those micropillar arrays showed that, although there were no clear correlations of CHF values with either r or $P_{\mathrm{cap}}K_{\mathrm{B}}$ overall, CHF values generally increased with either r or $P_{\mathrm{cap}}K_{\mathrm{B}}$ when the other was fixed. This result directly showed that CHF is not solely a function of either r or $P_{\mathrm{cap}}K_{\mathrm{B}}$; instead, each parameter has separate effects on CHF. To understand the structural effects on CHF values, we performed a scaling analysis to derive a relationship for CHF with a new unified descriptor, $q"_{\mathrm{CHF}} \sim \xi^{\mathrm{n}} P_{\mathrm{cap}}K_{\mathrm{B}}h$. Here ξ^{n} and $P_{\mathrm{cap}}K_{\mathrm{B}}h$ affect CHF values by promoting bubble departure frequency and delaying the expansion of dry area, respectively. The scaling analysis was confirmed with CHF values from our experiments and literature data. CHF values from our experiments showed a positive linear correlation with $\xi^{0.46}P_{\mathrm{cap}}K_{\mathrm{B}}h$, which also agreed with existing literature data. Our work elucidate the separate roles of thin film density and wickability in enhancing CHF values, which can enable improved designs of boiling surfaces for a variety of high heat flux applications.

Intentionally blank page

Chapter Five

Engineering surface structures for simultaneous enhancement of HTC and CHF

5.1 Introduction

Previous studies have shown that engineered surfaces can significantly enhance boiling performance (see Chapter 1.2.3). A representative example of surface structure that effectively enhance HTC is the microcavity (Figure 5.1a) [20, 23]. Microcavities can trap vapor embryo that promotes nucleation. Hemi-wicking surfaces such as micropillars and nanowires [24, 26, 27, 43] (Figure 5.1b), on the other hand, enhance CHF by harnessing the thin-film evaporation around pillars and capillary-fed rewetting through the structures (as discussed in Chapter 4). The simultaneous enhancement of CHF and HTC, however, remains challenging despite of state-of-art surface structuring. In this chapter, we developed surface structures that can achieve the simultaneous and significant enhancement of CHF and HTC.

5.2 Microtube arrays and tube-clusters in pillars (TIP)

5.2.1 Surface design and fabrication

We designed and investigated precisely controlled microtube structures (Figure 5.1c), where a cavity is defined at the center of a pillar, as a microscale structural building block to enhance HTC and CHF values simultaneously. Cavities are designed to induce vapor trapping and bubble nucleation for HTC enhancement, while the sidewalls of the microtube arrays provide CHF enhancement as micropillar arrays. Moreover, the designed microtube arrays enable effective separation of vapor and liquid paths during the bubble generation and departure cycles, where bubbles nucleate at the top of the microtubes while liquid rewets the surface through the microtube sidewalls. The separation of vapor and liquid paths was demonstrated to be effective for boiling enhancement on copper surfaces with modulated porous-layer coatings of spherical copper particles and contoured microchannels [133, 134]. In addition to uniform microtube arrays, we designed surfaces with microtube clusters interspersed with micropillars, referred to as tube-clusters in pillars (TIP), to reduce the coalescence of bubbles from the micro-tubes. While microtube arrays may enhance HTC and CHF values compared to a flat surface, we postulated that uniform microtube arrays might not achieve as high CHF values as micropillar arrays due to the drastically higher nucleation site density. Previous studies have suggested that the boiling crisis may be a result of the stochastic interaction of bubbles; in other words, an excessive nucleation site density, *i.e.*, cavity density, may lead to an earlier boiling crisis [110-112, 135].

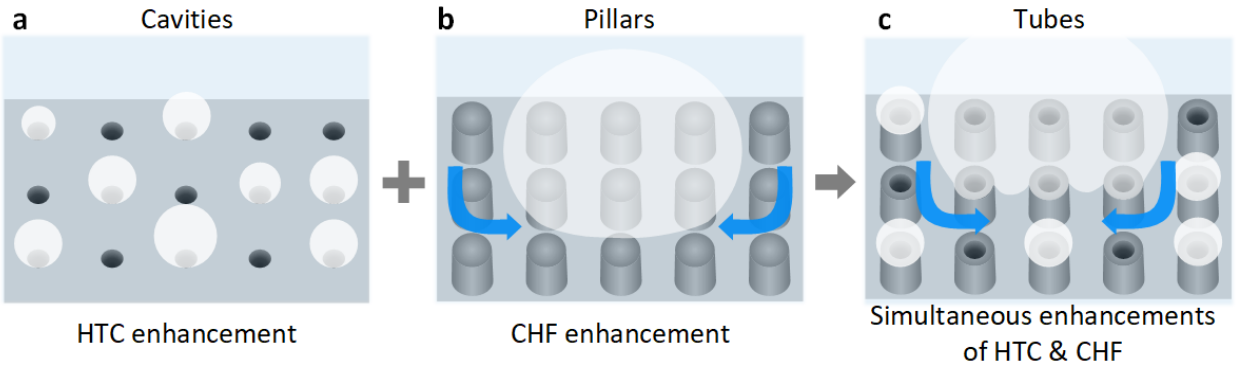

Figure 5.1. Microsurfaces and their effects on pool boiling heat transfer enhancement. (a) Cavities promote vapor bubble nucleation and enhance HTC values. (b) Pillar arrays provide enhanced CHF values by contact line augmentation and capillary-fed rewetting. (c) Tube arrays, where a cavity is defined at the center of a pillar, enable simultaneous enhancement of both HTC and CHF values.

To investigate the effects of microtube surface structures on pool boiling heat transfer compared to other structures, we fabricated micropillar, microcavity, microtube arrays, and TIP surfaces by photolithography and deep reactive-ion etching processes on silicon wafers (Figure 5.2). The surfaces were coated with a 100-nm-thick SiO_2 layer at the end of the fabrication process by plasma-enhanced chemical vapor deposition to ensure uniform hydrophilicity over the entire surface. The outer diameter (d), height (h), and pitch (p) of micropillar (Figure 5.2a) and microtube (Figure 5.2d and 5.2e) arrays were 22, 30, and 40 μm, respectively. The depth of the microcavity arrays was ~30 μm (Figure 5.2b). The cavity diameter (d_c) of microcavity and microtube arrays is directly related to the excess pressure in a bubble embryo ($\Delta P = \sigma/d_c$, where σ is liquid-vapor surface tension) required to initiate nucleate boiling. Combined with the Clausius-Clapeyron relation, the excess pressure can be expressed as the wall superheat for the onset of nucleate boiling, *i.e.*, $\Delta T_{ONB} \approx \frac{2\sigma T_{sat}}{h_{fg}\rho_g(d_c/2)}$, where h_{fg} and ρ_g are latent heat of vaporization and vapor density, respectively [136]. The inverse relation between ΔT_{ONB} and d_c plotted in Figure 5.2c shows that bubbles can more readily nucleate on a larger cavity as long as the cavity radius is much smaller than the

thermal boundary layer thickness δ_t, *e.g.*, $\delta_t \sim \mathcal{O}(10^{-4})$ m for saturated water at atmospheric pressure, which is an order of magnitude larger than d_c ($\mathcal{O}(10^{-6})$ - $\mathcal{O}(10^{-5})$ m) [137]. We fabricated microcavity and microtube arrays with d_c of 5 μm and 12 μm, which correspond to ΔT_{ONB} of 11℃ and 5℃, respectively, to investigate the effects of cavity size. A TIP surface with microtube clusters (300 × 300 μm^2) that were 2 mm apart from each other with micropillars between clusters is shown in Figure 5.2f, where the cluster-to-cluster pitch of 2 mm is based on the capillary length of water $l_c = \sqrt{\sigma/(\Delta\rho g)} \approx 2.5$ mm which was found to be efficient to separate nucleating bubbles [64, 138]. We named each surface according to its structure and cavity size as shown in Figure 5.2.

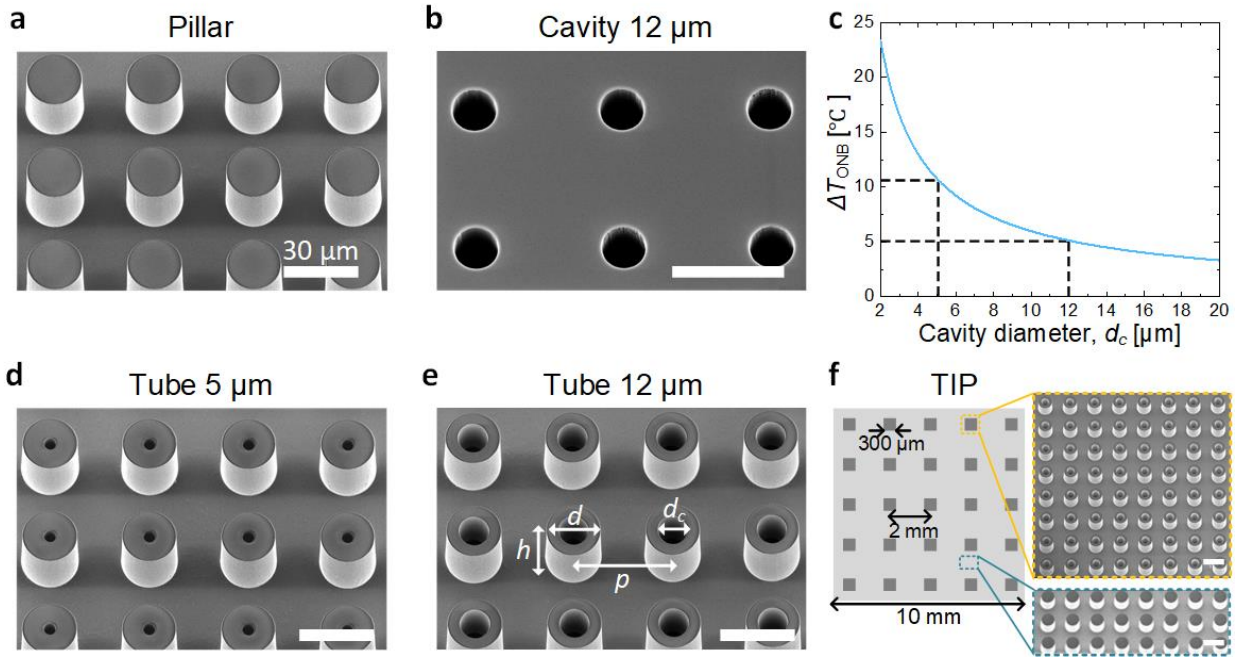

Figure 5.2. SEM images of fabricated microsurfaces and the onset of nucleate boiling temperature relationship with cavity diameter. (a) Micropillar arrays. (b) Microcavity arrays with 12 μm diameter. (c) Onset of nucleate boiling temperature as a function of cavity diameter. Microtube arrays with the cavity diameter of 5 μm (d) and 12 μm (e). (f) Schematics of boiling are of TIP surface where microtube clusters are separated from each other by cluster-to-cluster pitch of 2 mm with micropillars between the clusters. All SEM images are taken with 20° tilt angle and all scale bars are 30 μm.

5.2.2 Results and discussion

Figure 5.3a shows pool boiling curves for different surfaces. HTC is also plotted as a function of heat flux for a heat flux over 25 W/cm^2 in Figure 5.3b. In the plots, the structures with cavities, *e.g.*, microcavity, microtube, and TIP surfaces, have open data symbols, where the open area of the data symbols represent the cavity size, *i.e.*, the large and small open area represent the 12 μm and 5 μm cavity diameters, respectively. Compared to a flat surface, all structured surfaces showed enhancement of either or both HTC and CHF. As expected, we observed distinctly different effects of cavity and pillar structures on boiling behavior. The boiling curves of cavity arrays showed significantly steeper slopes, *i.e.*, higher HTC values, than that of flat and pillar surfaces, while their CHF values remained very close to the flat surface. Also, the larger cavity of 12 μm resulted in a higher HTC value than the smaller cavity of 5 μm near the onset of nucleate boiling, which was consistent with the theoretical prediction of the ΔT_{ONB}. Micropillar surfaces, on the other hand, showed significant enhancement of CHF, but no enhancement of HTC up to the wall superheat of ~30°C due to the absence of artificial nucleation sites. The uniform microtube arrays, which were designed to exploit the combined effects of cavity and pillar structures, enhanced HTC and CHF values simultaneously. Similar trends of HTC with uniform cavity arrays were observed, for example, the lower ΔT_{ONB} of tubes with 12 μm cavity than 5 μm. Compared to the flat surface, the HTC values of Tube 5 μm and Tube 12 μm at CHF points (h_{CHF}) were enhanced ~220% and ~244%, respectively. Moreover, Tube 5 μm and Tube 12 μm surfaces achieved 60% and 62% CHF enhancement, respectively, compared to the flat surface, presumably due to the additional microlayer evaporation (q''_{ml}) around the sidewalls of microtubes (Figure 5.3c) [27, 46, 127]. The experimental results show that the CHF enhancement of microtube arrays was not as significant as that of micropillar arrays even though they both have the same surface wickability due to their identical sidewall geometries. For microtube surfaces, the

high nucleation site density and excessive coalescence of bubbles may lead to the earlier boiling crisis than that with micropillar surfaces.

Boiling curves of TIP surfaces that separated microtube nucleation clusters from each other by 2 mm and included micropillar arrays between clusters corroborated our hypothesis. Both TIP surfaces showed slightly higher CHF values than that of uniform pillar arrays by minimizing bubble coalescence and fully exploiting the role of micropillars for CHF enhancement. Micropillar arrays, TIP 5 μm, and TIP 12 μm surfaces showed ~110%, ~138% and ~129% CHF enhancement, respectively. The additional CHF enhancement of TIP surfaces compared to micropillar arrays can be attributed to two factors: additional evaporation of penetrated liquid in the microtube cavities (Figure 5.3d) and effective separation of liquid and vapor paths, *i.e.*, the bubble nucleation and departure regions are separated from the paths of the rewetting liquid (Figure 5.3e). The volume of penetrated liquid (ΔV_{liq}) during the rewetting of liquid and additional heat flux from its evaporation is, however, negligibly small (~0.06 W/cm^2) compared to the enhancement (27.2 W/cm^2 and 17.1 W/cm^2 for TIP 5 μm and TIP 12 μm, respectively). The additional CHF enhancement is therefore attributed to effective separation of liquid and vapor paths, where a similar phenomenon has been observed in literature [31]. On TIP surfaces, bubbles are generated on top of microtube clusters; consequently, rewetting liquids may come from the top of micropillar arrays to under the bubbles with minimal disturbance. In contrast, uniform micropillar arrays have preferred nucleation sites at the bottom corners of pillars due to the local temperature concentration. Therefore, nucleating bubbles can block the paths of rewetting liquids during the bubble growth period, which would adversely affect CHF enhancement. We show CHF values of all surfaces in Figure 5.3f and their enhancement mechanisms.

It is also interesting to note that the boiling curves of TIP surfaces showed two different regimes due to two surface features (Figure 5.3a). In the early stage of nucleate boiling, ΔT_w

< ~30℃, promotion of nucleation from microtubes is dominant, which leads to a HTC enhancement compared to uniform pillar arrays. When ΔT_w > ~30℃, the TIP boiling curves overlap with the boiling curve of the micropillars, which suggests that the evaporative heat transfer from the sidewalls of the micropillars is dominant. In addition, the results suggest that by controlling the cluster-to-cluster pitch, we can design TIP surfaces with a boiling curve located in between the uniform microtube arrays and the TIP surface with the cluster-to-cluster pitch of 2 mm (shaded red area). As the pitch becomes shorter and the density of microtube, *i.e.*, nucleation sites, is higher, the effects of promoting bubble nucleation from microtubes become more dominant and the surface will enhance HTC more effectively than CHF; the opposite holds for the wider pitch and lower nucleation site density. This controllability may offer surface design flexibility to achieve a desired boiling curve according to the application.

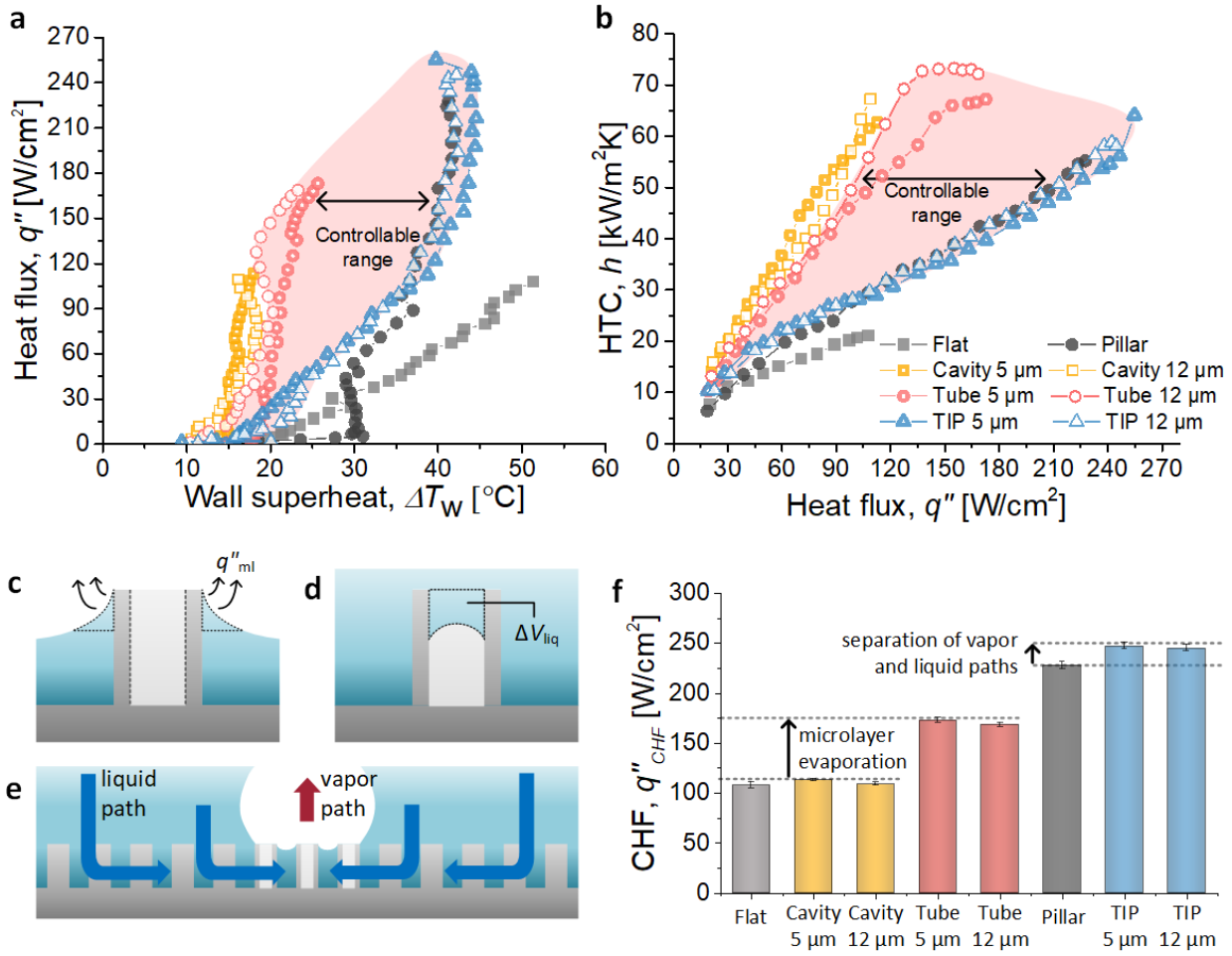

Figure 5.3. Pool boiling results and enhancement mechanisms of microtube and TIP surfaces. (a) Pool boiling curves of water on different surface structures. (b) Heat transfer coefficients as a function of boiling heat flux. For (a) and (b), the experimental uncertainty is smaller than the marker size. Shaded red areas show the range of boiling curves that can be obtained by controlling the cluster-to-cluster pitch of a TIP surface. (c – d) Schematics of cross-section view of a microtube during boiling. (c) Evaporative heat flux from the microlayer around the sidewalls of microtubes (q''_{ml}), which provides additional heat flux to microtube arrays compared to microcavity arrays. (d) Penetrated liquid with volume of ΔV_{liq} in a microtube cavity during the rewetting of liquid. Analytical estimation suggests that the evaporation of the penetrated liquid has minimal effects on CHF enhancement of TIP surfaces. (e) Schematic of the separated liquid and vapor paths on TIP surfaces. Bubbles are generated on top of microtube clusters, while rewetting liquids come from the outside of microtube clusters with minimal disturbance from growing bubbles. (f) CHF values for different surface structures and CHF enhancement mechanisms.

Imaging of the bubble dynamics (Figure 5.4) of different surface structures captured by a high-speed camera (Phantom v7.1, Vision Research) supports the boiling curve analysis. Each row shows the bubble dynamics at different heat flux ranges, *e.g.*, ~ 3 – 8 W/cm^2, ~34 – 40 W/cm^2, and at CHF points, respectively, while each column represents different surface structures, *e.g*., Pillar, Cavity 12 μm. Tube 12 μm, and TIP 12 μm (from left to right). At the very early stage of nucleate boiling (q'' < 10 W/cm^2), the micropillar surface had noticeably different bubble dynamics compared to the other surfaces having artificial nucleation sites. Since the surfaces with cavities nucleated at very low superheat, there were small bubbles with high nucleation site density; in particular, TIP 12 μm showed separated bubbles nucleated from microtube clusters. The micropillar surface, on the contrary, had a large single bubble at this stage. The surface without artificial nucleation sites such as micropillar array generally required high wall superheat for nucleation, which led to the large bubble size since the inertia-driven bubble growth became more dominant [139]. Similar trends continued when the heat flux increased to ~34 – 40 W/cm^2 but the higher heat flux generated more active nucleation sites with higher bubble departure frequency. The bubble snapshots at CHF illustrated the CHF enhancement mechanisms on different surface structures. According to previous studies, the boiling crisis may be the result of stochastic interaction of bubbles, where active nucleation site density, bubble departure diameter, and departure frequency are important parameters for the interactions [110-112, 135]. In the cases of Cavity 12 μm and Tube 12 μm, the coalesced bubbles formed vapor films over the boiling surfaces at CHF due to their extensively dense nucleation sites, which suggests that the high nucleation site density was the dominant triggering mechanism of the boiling crisis on these surfaces. The snapshots of micropillar arrays and TIP 12 μm showed, on the other hand, that boiling areas were not entirely covered by a vapor film; instead, parts of the boiling areas remained wet. This result suggests that, in addition to nucleation site density, other parameters such as bubble departure diameter and frequency also play important roles on determining CHF. In particular, TIP 12 μm showed that the majority of bubbles were

generated at microtube clusters even at CHF. Separated liquid and vapor paths facilitated rewetting of liquids in between the tube clusters and accelerated bubble departure from the clusters. This high-speed imaging analysis supports our findings from the boiling curve data that the additional CHF enhancement compared to uniform pillar arrays is attributed to effective separation of liquid and vapor paths of TIP surfaces.

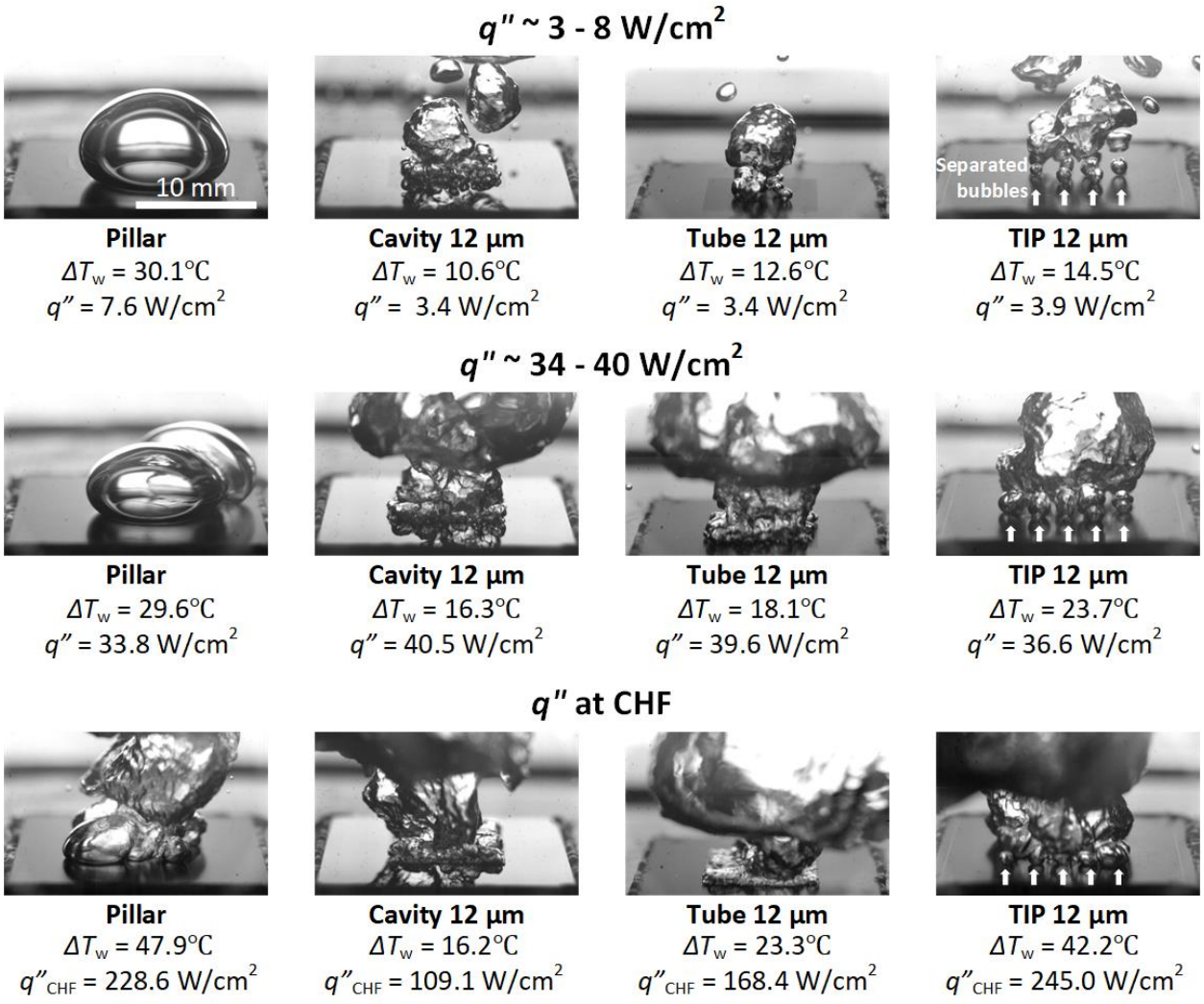

Figure 5.4. Images of boiling captured by a high-speed camera with up to 4000 frames per second. Each row shows the bubble dynamics at different heat flux ranges and each column represents different surface structures. TIP 12 μm surface shows separated bubbles from microtube clusters, which are highlighted with white arrows. All images have the same scale and were taken with 19° tilt angle.

5.3 Hierarchically structured tube arrays and TIP

Uniform microtube arrays TIP surfaces have shown the potential for systematic control of a boiling curve associated with the tube cluster-to-cluster pitch. The simultaneous and significant enhancement of HTC and CHF, however, has been limited due to the intrinsic trade-off between HTC and CHF associated with the nucleation site density.

5.3.1 Multi-scale control of vapor nucleation

In this section, we demonstrate an approach to achieve simultaneous extreme enhancement of HTC and CHF by overcoming this trade-off. By designing a hierarchically structured TIP surface (h-TIP), we can control vapor nucleation at multiple length-scales while providing capillary wicking (Figure 5.5). For CHF enhancement, we minimized bubble coalescence and exploited capillary wicking based on the TIP structure, that is, by defining separated nucleation sites with tube clusters (shaded dark-red area in Figure 5.5a). For HTC enhancement, on the other hand, we promoted vapor nucleation with microscale cavity (Figure 5.5b), where evaporation could be further enhanced by extending the liquid-vapor interfaces on nanostructures (Figure 5.5c). Our strategy to enhance HTC does not have the detrimental effect of continuing to increase the nucleation site density and as a result, prevent the liquid rewetting processes.

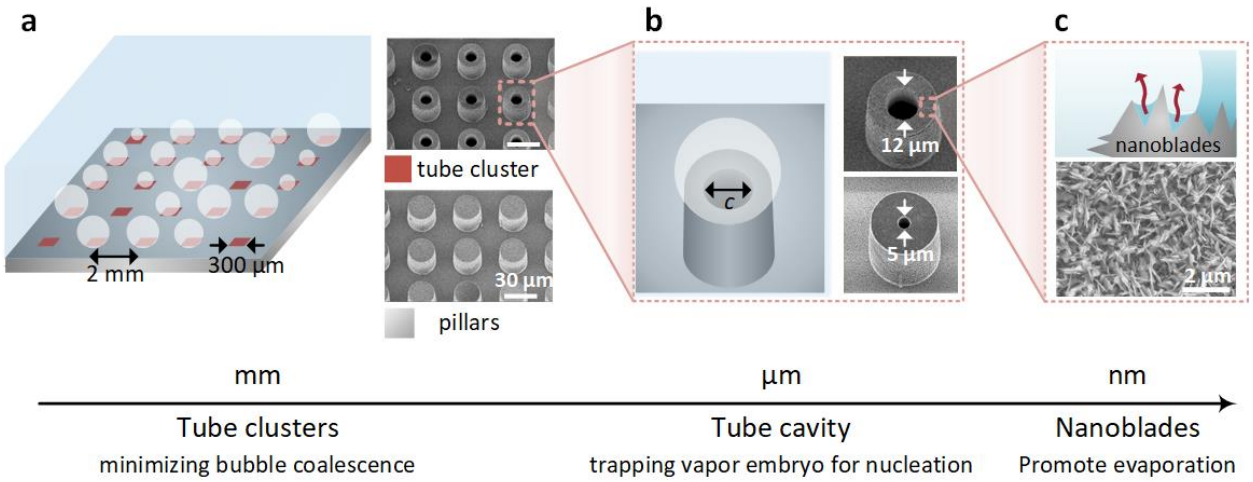

Figure 5.5. Schematics and SEM images of a hierarchically structured TIP surface (h-TIP) that exhibits capillary wicking while controlling vapor nucleation using multiple length-scales. (a) The h-TIP surface consists of hierarchical tube clusters interspersed in hierarchical pillar arrays. Left panel: 2 mm pitch between the tube clusters separates bubbles and minimizes bubble coalescence. The dark-red patterned regions represent the hierarchical tube clusters whereas the grey region is covered by hierarchical pillar structures. Right panel: SEM images of the hierarchical tube structures (top) and hierarchical pillar structures (bottom). Scale bars are 30 µm. (b) Microscale cavity at the center of tube structure traps vapor embryo and promotes nucleation. Left panel: schematic of bubble nucleation on the top of a tube structure. Right panel: SEM images of a hierarchical tube with a cavity diameter of 12 µm (top) and 5 µm (bottom). (c) Nanoblades on top of microstructures augment liquid evaporation under the bubbles. Top panel: schematic of the extended liquid-vapor interface on the nanostructures. Bottom panel: SEM image of the nanostructures created all over the surface: tubes, pillars, and flat base surfaces.

5.3.2 Surface fabrication and formation of nanostructures

We fabricated uniform arrays of hierarchically structured tubes (h-Tube), which consist of only tubes but pillars, along with hierarchically structured TIP surfaces (h-TIP) to investigate the effectiveness of bubble separation by TIP structures in the presence of nanostructures. First, microscale structures were created through the same processes as in Chapter 5.2 with the same microscale dimensions, *e.g.*, outer diameter, height, and pitch of microtubes and micropillars were 22, 30, and 40 µm, respectively. For both h-Tube and h-TIP surfaces, two

cavity diameters of 5 and 12 μm were fabricated (SEM images in Figure 5.5b). The cluster-to-cluster pitch was also set to the same value of 2 mm based on the capillary length of water (≈ 2.5 mm) (Figure 5.5a) [64, 132, 138]. On top of the microstructured surfaces, sharp blade-like cupric oxide (CuO) nanostructures were created by sputtering a 500 nm copper layer over the microstructures followed by an oxidation in an alkali solution ($NaClO_2$, NaOH, Na_3PO_4, and deionized water with 3.75:5:10:100 wt.%) at 95°C for 2 minutes (SEM image in Figure 5.5c) [140]. At the end, we deposited a 20 nm SiO_2 layer using atomic layer deposition to ensure uniform hydrophilicity along the entire hierarchical structures.

5.3.3 Results and discussion

Figure 5.6a shows pool boiling curves of h-TIP and h-Tube surfaces along with microstructured surfaces along with the microstructured surfaces with the same microscale dimensions such as micropillars, microtubes, and TIP surfaces from the previous chapter for comparison [132]. Each surface is named with its structure and the cavity diameter; for example, h-TIP 12 μm is a h-TIP surface that has 12 μm diameter cavity in each tube clusters. We also plotted HTC as a function of heat flux in Figure 5.6b. All hierarchical structures showed enhanced HTC and CHF values compared with their microstructure counterparts without nanostructures. For example, h-TIP surfaces significantly enhanced HTC values while maintaining the high CHF of TIP surfaces. Compared with up to 209% enhancement (relative to a flat surface) of maximum HTC (h_{max}) on normal TIP surfaces, h-TIP 5 μm and h-TIP 12 μm achieved 289 and 389% enhancement, respectively. At the same time, CHF values of h-TIP 5 μm and h-TIP 12 μm were enhanced 138 and 125%, respectively. In fact, the boiling curves of h-TIP surfaces shifted left of the boiling curves of normal TIP surfaces. This simultaneous enhancement of HTC and CHF on h-TIP

structures was achieved because the nanostructures extended liquid-vapor interfaces. As a result, this effect promoted evaporation and enhanced HTC. Meanwhile, the nucleation site density was maintained (Figure 5.6c and 5.6d) to prevent hindering of the liquid rewetting, which would limit CHF enhancement. Also, nanostructures on top of the pillars can involve the pillars, in addition to tube clusters, into HTC enhancement when bubbles grow over the pillars. We expect there are two mechanisms with in the nanostructures that promote evaporation and bubble departure frequency. First, the liquid imbibed in the nanostructures can evaporate quickly under the vapor bubbles because of the nanoscale liquid film thickness (mechanism (1) in Figure 5.6d). Second, when the nanostructures are filled with vapor, the vapor can diffuse and merge with a growing bubble above them, which will accelerate the bubble growth and departure frequency (mechanism (2) in Figure 5.6d).

A similar enhancement was observed on h-Tube surfaces compared with normal microtube surfaces due to the enhanced evaporation from the nanostructures. The maximum HTC value of h-Tube 5 μm and h-Tube 12 μm, for example, were 351 and 448% enhancement, respectively. This result is significant improvement compared with the 244% enhancements of h_{max} on normal microtube arrays. In addition to the HTC enhancement, h-Tube surfaces demonstrated higher CHF enhancement than microtube surfaces, where h-Tube 5 μm and h-Tube 12 μm achieved 78 and 82% CHF enhancement, respectively, while Tube 12 μm showed 62% CHF enhancement. Because the extensively high nucleation site density primarily triggered the boiling crises on h-Tube and microtube surfaces, the addition of nanostructures was able to enhance CHF as well as HTC by providing additional evaporation heat flux for a similar nucleation site density near CHF. Yet, the CHF enhancement was still limited compared to TIP and h-TIP surfaces. The pool boiling results of h-TIP and h-Tube surfaces confirm that our h-TIP surfaces maintained the high CHF values of

TIP surfaces while significantly improving the HTC because of the effective separation of liquid and vapor paths during boiling, which also allows surfaces to exploit the capillary wicking completely (Figure 5.6c).

Another interesting observation to note was that hierarchical surfaces with 12 μm cavity diameters (h-Tube 12 μm and h-TIP 12 μm) showed a decrease in wall superheat near 20℃ while the heat flux increased, a phenomenon known as boiling inversion. However, a similar phenomenon was not observed on hierarchical surfaces with the 5 μm cavity diameter. While previous works attributed the boiling inversion primarily to enhanced macro-convection driven by effective separation of liquid-vapor paths [141], understanding the boiling inversion mechanism is still limited and needs further investigation.

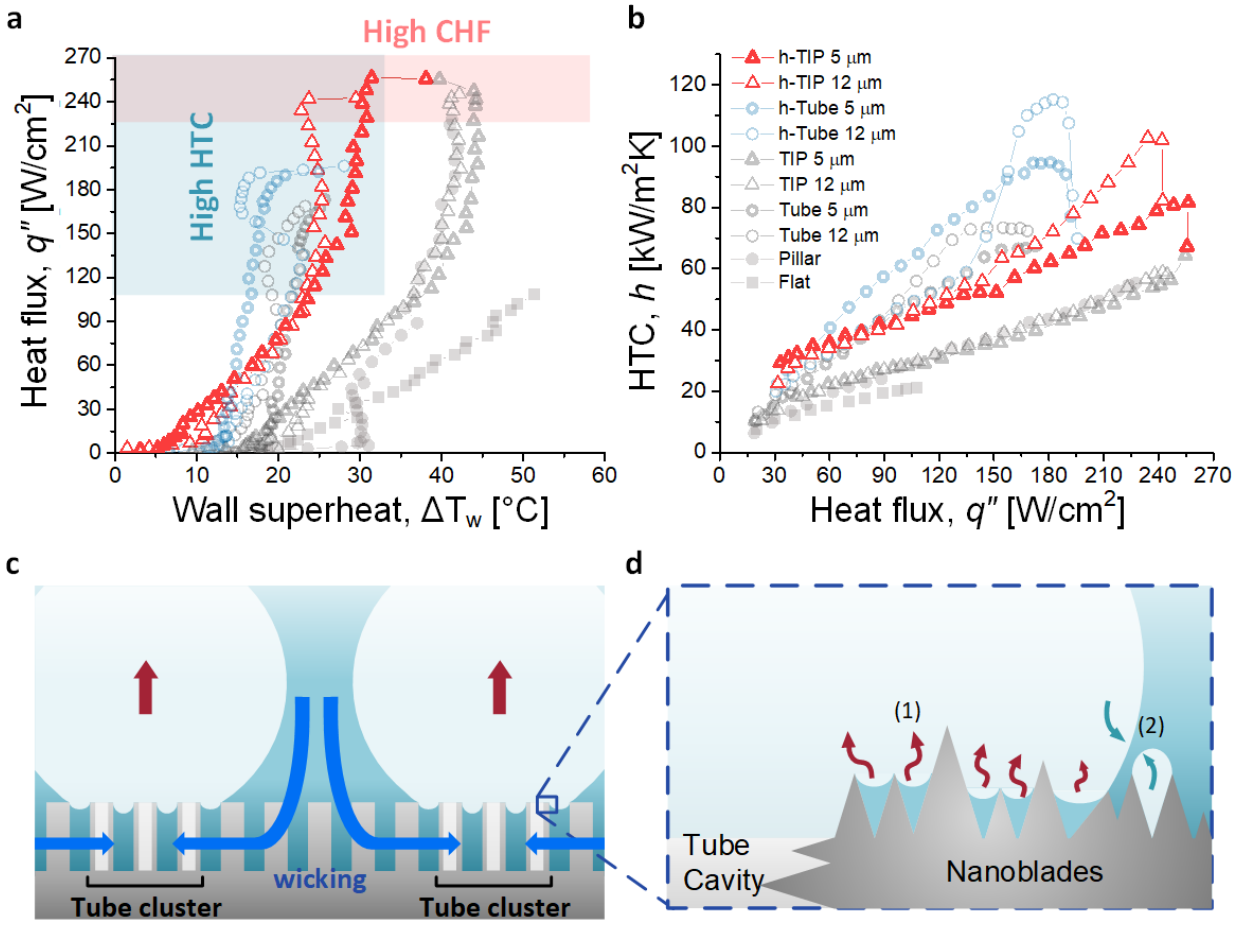

Figure 5.6. Pool boiling results and schematics of boiling heat transfer enhancement on h-TIP surfaces. (a) Pool boiling curves of saturated water on h-Tube and h-TIP surfaces compared with microstructured surfaces without nanostructures. (b) HTC as a function of heat flux. The experimental uncertainty is smaller than the marker size. (c) Schematic of the separated liquid-vapor paths during boiling on an h-TIP surface. Bubbles grow on top of and depart from tube clusters, while liquids coming outside tube clusters rewet the surface by capillary wicking. (d) Schematic explaining the two mechanisms for the nanostructure-induced evaporation: (1) rapid evaporation of thin liquid films due to their nanoscale thickness and (2) diffusion of vapor trapped in nanostructures, which accelerates bubble growth and departure.

We confirmed the different behavior of bubble interactions on h-Tube and h-TIP surfaces by capturing the bubble dynamics with a high-speed camera (Phantom v7.1, Vision Research) up to 4000 frames per second. Figure 5.7 shows images capturing the bubble dynamics on h-Tube and h-TIP surfaces at a moderate heat flux of ~40 W/cm^2 (the first row

of Figure 5.7) and at CHF (the second row of Figure 5.7). Since microscale cavities promote nucleation, significantly higher nucleation site densities were observed on h-Tube surfaces compared to h-TIP surfaces. Accordingly, bubbles on h-Tube surfaces showed intensive interactions with each other. In the case of h-TIP surfaces, on the contrary, bubbles nucleated from spatially separated tube clusters, which led to a reduced bubble coalescence. This behavior continued to until CHF was reached. We observed that vapor filmed formed over h-Tube surfaces at CHF, which suggests that CHF enhancement was limited because of the high nucleation site density. The separation of nucleating bubbles on h-TIP surfaces, on the other hand, was effective even at CHF; therefore, the CHF on h-TIP surfaces was enhanced until it was limited by capillary wicking. This observation supports our boiling curve analysis that h-TIP surfaces enhanced HTC without increasing the nucleation site density, resulting in simultaneous enhancement of HTC and CHF.

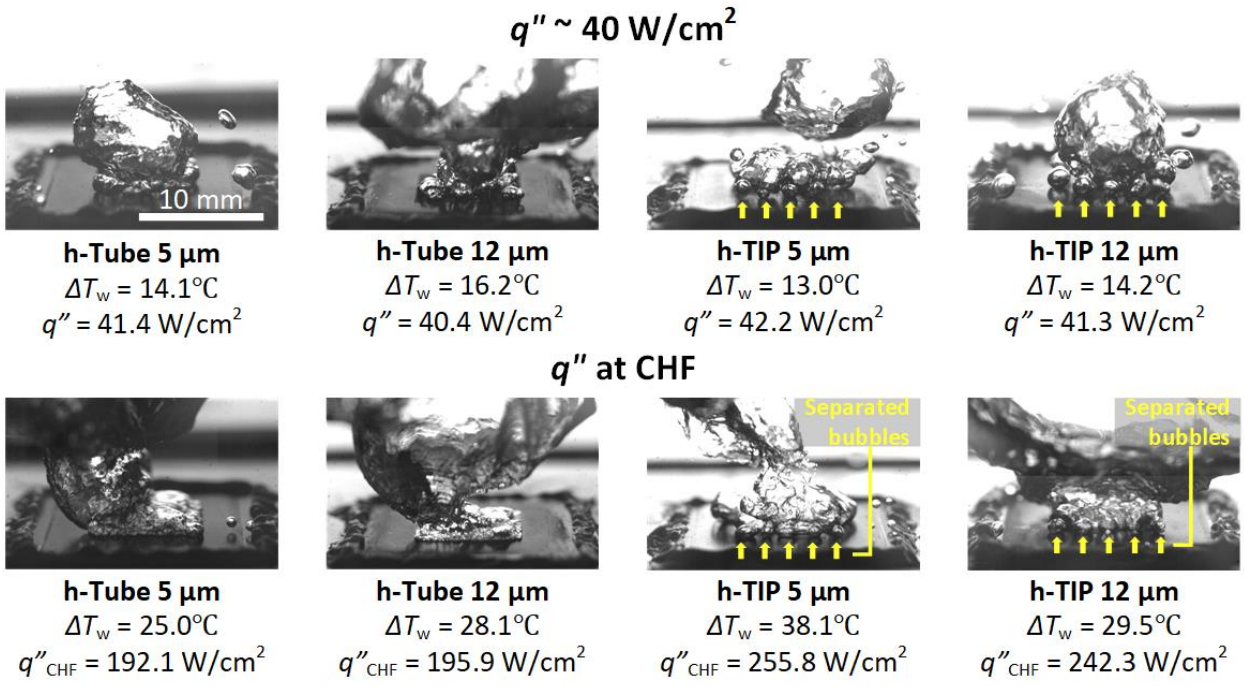

Figure 5.7. Images of bubbles on h-Tube and h-TIP surfaces during boiling captured by a high-speed camera with a 19° tilt angle and up to 4000 frames per second. First and second rows show bubble dynamics at a heat flux of ~40 W/cm^2 and at CHF, respectively. h-TIP surfaces showed effectively separated bubbles even at CHF (highlighted with yellow arrows), while h-Tube surfaces showed extensive bubble coalescence which leads to the formation of vapor films at CHF.

5.3.4 Regime map of CHF and HTC values of different micro/nano structures

In Figure 5.8, we compared CHF ($q"_{CHF}$) and the maximum HTC (h_{max}) values of uniform microtube arrays, TIP, h-Tube, and h-TIP surfaces with different micro/nano structures from the literature. The structures from the literature include micropillar [24, 142], hierarchically structured pillar (h-Pillar) [34], nanowire [38, 43, 143, 144], microcavity [22, 132], microridge [41], and microchannel [22, 105]. All data shown in Figure 5.8 are summarized in Supplementary Information Table 8.3. Since surface wettability can also affect boiling

performance, we included the data of SiO_2 surfaces to compare the sole effect of surface structure, except nanowires based on silicon. Microcavity, channel, and ridge structures generally provide significant enhancement of HTC values, but CHF enhancement remains limited to ~70%. On the contrary, micropillars can enhance CHF values more than 100%, but the enhancement of HTC values is not as high as in cavity, channel, and ridge structures. The uniform microtube arrays and TIP surfaces show the highest simultaneous enhancement of CHF and HTC values among microstructured surfaces. Most of all, our h-TIP surfaces showed the highest simultaneous enhancement of HTC and CHF among all other structures, as shown on the top-right corner of the plot. Yet, there are opportunities for further enhancement of h-TIP surfaces by optimizing microscale structure dimensions such as the outer diameter, pitch, and height of hierarchical tube and pillars, which were fixed in this work.

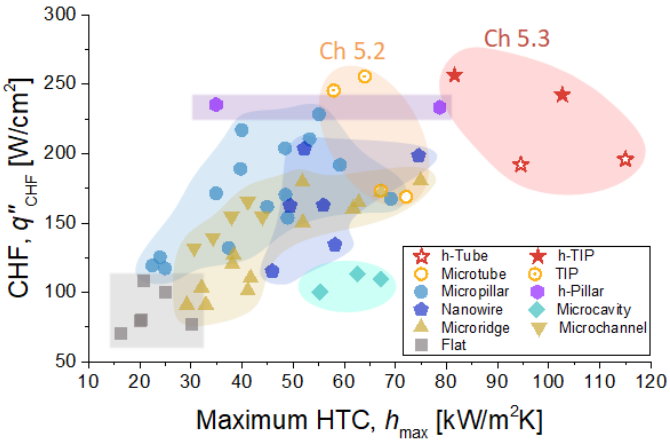

Figure 5.8. Regime map of CHF (q''_{CHF}) and maximum HTC (h_{max}) values of different SiO_2 micro/nano structures and Si nanowires. This work with h-TIP shows the highest performance (upper right region) with simultaneous CHF and HTC enhancement.

5.4 Summary

In Chapter 5.2, we designed microtube structures for simultaneous enhancement of CHF and HTC values during pool boiling heat transfer. We analyzed pool boiling results and analyzed enhancement mechanisms with high-speed imaging. Uniform microtube arrays demonstrated simultaneous enhancement of CHF and HTC values up to 62% and 244%, respectively. The enhancement of HTC is attributed to active bubble nucleation from microtube cavities, while CHF enhancement is a result of microlayer evaporation around microtube sidewalls. Moreover, higher CHF values were achieved than that of uniform micropillar arrays with TIP surfaces by separating microtube clusters by 2 mm from each other within micro-pillars arrays. As a result, the earlier boiling crisis due to extensive bubble coalescence could be prevented. By changing the cluster-to-cluster pitch, our approach can be used to design TIP surfaces with boiling curves in between those of uniform micropillars and the TIP surface with the cluster-to-cluster pitch of 2 mm.

In Chapter 5.3, we incorporated nanostructures on top of TIP surfaces that achieved superior pool boiling performance via multi-scale control of vapor nucleation on hemi-wicking surfaces. Our strategy included the minimization of bubble coalescence, promoting vapor nucleation and enhancing evaporation by engineering surfaces with separated tube clusters, microscale cavities, and nanostructures, respectively, Meanwhile, capillary wicking performance was maintained in the presence of dynamically interacting boiling bubbles. Our hierarchical TIP surfaces (h-TIP) achieved significant CHF enhancement up to 138% as well as 389% HTC enhancement. The enhanced boiling performance promises significant energy savings in various boiling applications.

Chapter Six

Enhancement of boiling with scalable sandblasted surfaces

6.1 Introduction

In previous chapters, we investigated the structural effects on the boiling heat transfer enhancement systematically using clean-room processed micro- and nano-structures. These clean-room processed surfaces are great for fundamental research but not suitable for industry-scale applications due to the limited scalability. Solution-based surface modifications such as surface oxidation, wet etching, synthesis of nanowires, and coatings of nanoporous layers may provide a better scalability than clean-room processes [43, 140, 145-148]; however these approaches are often limited to a specific material due to the need for chemical compatibility, and nanomaterials have limited durability that may preclude use in industrial applications [149].

In this chapter, we propose a sandblasting process as a scalable surface structuring technique for the enhancement of pool boiling heat transfer for industry-scale boiling

applications. Sandblasting is a pure physical bombardment process free of chemical compatibility constraints; therefore, it is applicable to versatile materials including Zircaloy-4, which is a commonly used material for nuclear reactor applications [150]. In fact, sandblasting has already been utilized as a physical texturing method to study the effects of surface roughness on boiling heat transfer in previous studies [151-158]. The detailed analysis on the structural characteristics of sandblasted surfaces and their effects on boiling heat transfer, however, are still lacking. In this work, we investigate the enhancement of pool boiling heat transfer by sandblasting boiling surfaces. The pool boiling experiments are conducted with water on silicon surfaces sandblasted by aluminum oxide (Al_2O_3). The abrasive media size was varied with 25, 50, 100, and 150 μm. Surface morphology and capillary-wicking performance are characterized by an optical profilometer and capillary-rise tests. Surfaces sandblasted by larger abrasives (up to 150 μm) exhibit higher roughness and volumetric wicking rate, resulting in greater enhancements of CHF and HTC values.

6.2 Sandblasting process

Sandblasted boiling samples were prepared based on a 650 μm-thick silicon wafer with thermally grown 1 μm SiO_2 layers on both sides. The top SiO_2 layer was completely etched by reactive-ion etching to expose underlying silicon before sandblasting with a laboratory-scale sandblaster (AccuFlo AF10 Standard Tank, Comco Inc.). A schematic of the sandblasting process is shown in Figure 6.1. The blasting nozzle was mounted on an XY linear stage and rasters over the surfaces with a constant line-pitch (p_l) of 1.1 mm and a sweeping speed (v) of 6.1 cm/s, where its motion is controlled with a microcontroller (Arduino Uno). The nozzle-to-sample distance (d_n) and blasting pressure (P) were fixed at 12.7 mm and 827 kPa (120 psi), respectively. In order to create different structural features, Al_2O_3 abrasives with four different nominal sizes (25, 50, 100, and 150 μm) were tested.

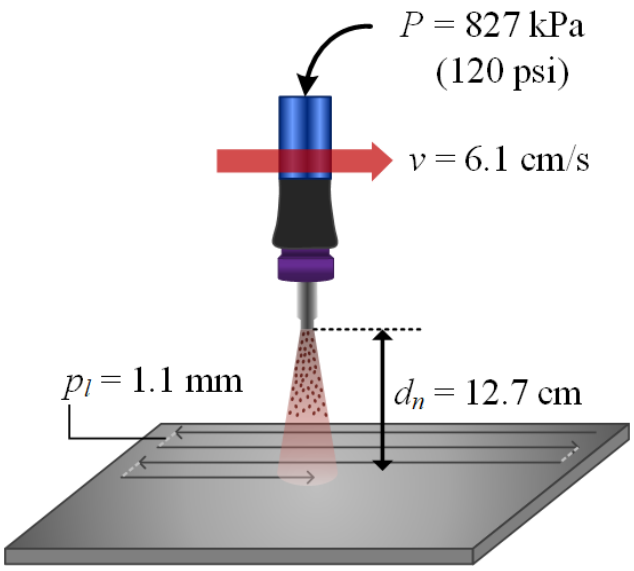

Figure 6.1. A schematic of the sandblasting process. Sandblasting pressure (P), sweeping speed (v), line-pitch (p_l), and nozzle-to-sample distance (d_n) were fixed while changing the Al_2O_3 abrasive size from 25 to 150 µm.

6.3 Morphology of sandblasted surfaces

The surface structures created by the sandblasting process were analyzed quantitatively by an optical profilometer (Non-contact 3D profiler CCI, Taylor Hobson) as shown in Figure 6.2. Figure 6.2a – d show the three-dimensional profile images of surfaces sandblasted by 25, 50, 100, and 150 µm, respectively. Figure 6.2e shows the change in r along with the arithmetic-mean roughness (R_a) and root-mean-square roughness (R_q) as a function of blasting abrasive size. We measured the roughness parameters at ten different randomly selected positions on each surface. The average and standard deviation values were used as data points and error bars, respectively. All three parameters increased noticeably as abrasive size increased from 25 to 100 µm, while the differences of parameters between the cases of 100 and 150 µm abrasives were insignificant and within an error bar range. The plots of surface profiles in a horizontal direction are shown in Figure 6.2f – h. Grey regions represent the overlapped

profiles over the other horizontal direction, from which the peak-to-valley amplitude Δ*z* was characterized. The peak-to-valley amplitude increased with the abrasive size. A blue line in each plot shows a typical profile at a specific position in the other horizontal direction.

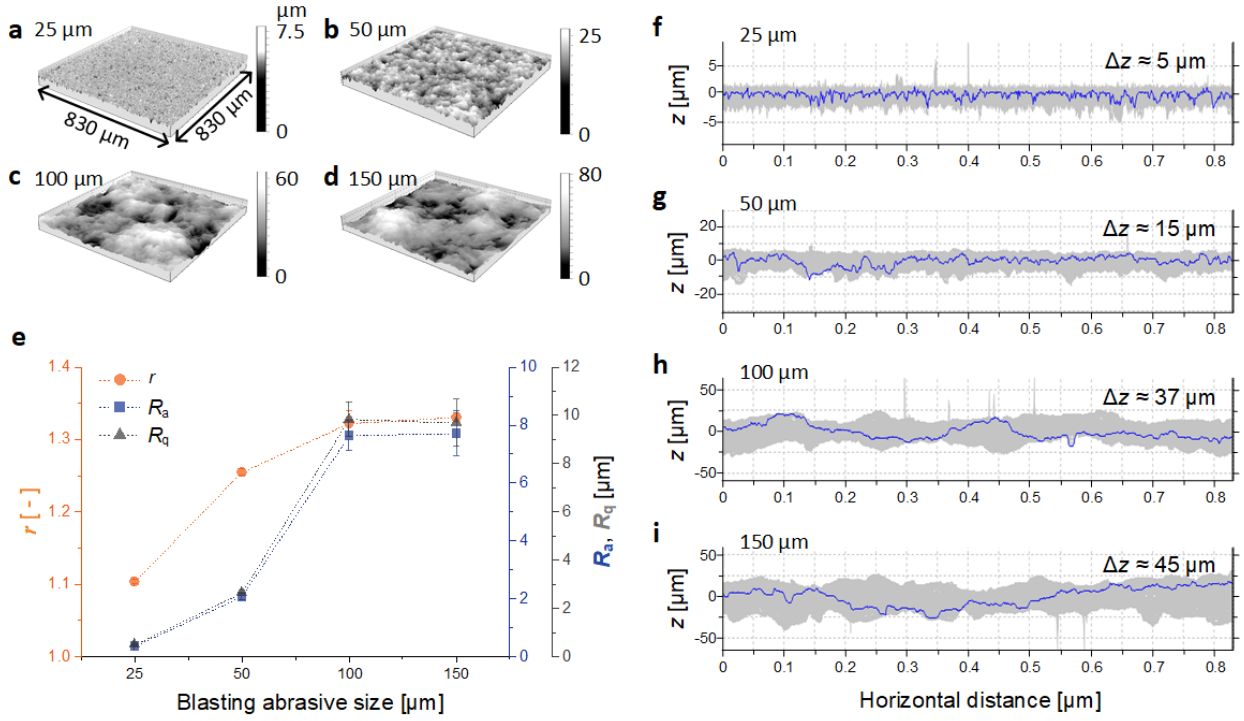

Figure 6.2. Surface structures characterized by an optical profilometer. (a – d) Three-dimensional profiles of surfaces sandblasted by 25, 50, 100, and 150 µm, respectively. (e) Surface area ratio (*r*, orange circles), arithmetic-mean roughness (R_a, blue squares), and root-mean-square roughness (R_q, gray triangles) as functions of blasting abrasive size. Error bars represent the standard deviations of ten different measurements at random positions on each surface. (f – i) Profile plots in one of the horizontal directions of surfaces sandblasted by 25, 50, 100, and 150 µm, respectively. The blue line and grey region indicate a profile at a fixed position and overlaps of profiles in the perpendicular horizontal direction, respectively. The peak-to-valley amplitude Δ*z* was characterized based on the gray region.

The SEM images in Figure 6.3a show the effects of abrasive sizes on surface structures qualitatively. The EDS images of silicon (Figure 6.3b) and aluminum (Figure 6.3c) taken at the same spots of each surface reveal that the sandblasting on silicon surfaces can create not

only cavities by etching the surfaces but also protruded structures with the implanted abrasives. The EDS mapping of silicon (Figure 6.3b) shows that most exposed area is composed of the base material: silicon. Spots where aluminum is detected, on the other hand, indicate protruded structures created by implanted Al_2O_3 abrasives. The resulting cavity and protruded surface structures can promote bubble nucleation and exhibit superhydrophilicity during pool boiling, which can enhance HTC and CHF values, respectively.

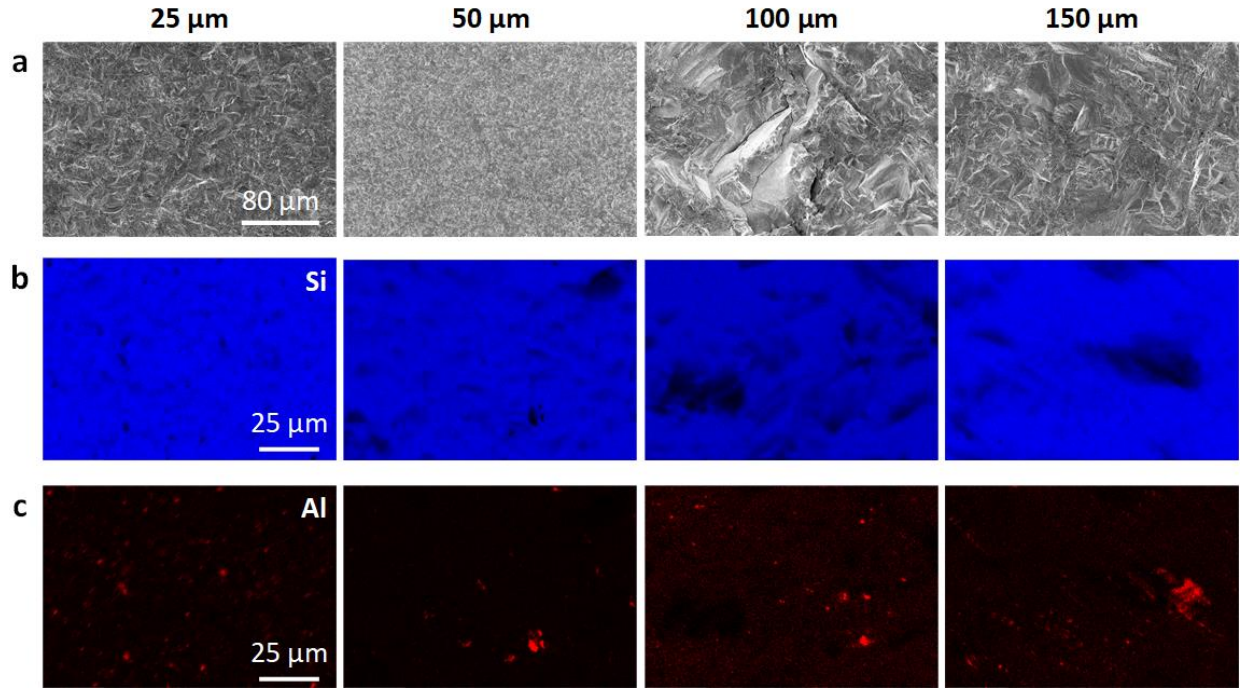

Figure 6.3. Morphology and chemical compositions of sandblasted surfaces. Each column shows a surface sandblasted by a specific abrasive size. (a) SEM images. (b, c) EDS images of silicon (blue) and aluminum (red), respectively. EDS images of aluminum show the presence of Al_2O_3 abrasives on surfaces after the sandblasting process.

6.4 Wickability of sandblasted surfaces

In addition to surface roughness *r*, we characterized the wickability of sandblasted surfaces by capillary rise tests (Figure 6.4a). A sample was moved vertically toward the reservoir of water until it came in contact, resulting in upward capillary rise flow through the sandblasted surface. The propagation speed of the capillary rise was captured with a digital camera at 30 frames per second. Figure 6.4b shows the time-lapse images of propagating wicking front on the surface sandblasted by 150 μm abrasives as an example. Once the sample contacts the surface of water, a capillary meniscus forms (highlighted in white dashed lines) first, and liquid propagates (wicking front shown with yellow dashed lines) upward with the speed (u) associated with the balance between capillary pressure and viscous resistance. This liquid propagation through porous sandblasted structures can be described by Darcy's law (or Brinkman equation if viscous shearing from the bottom surface is comparable to structural permeability effects) as

$$\frac{dx}{dt} = \frac{K_{\mathrm{B}}}{\mu}\frac{\Delta P_{\mathrm{cap}}}{x}. \tag{6.1}$$

Here x, t, and μ are the propagation distance, time, and dynamic viscosity of liquid. By solving the equation with initial condition $x(t = 0) = 0$, the propagation distance (x) can be expressed as a square root function of time (t) with a propagation coefficient G as a proportional coefficient [118], *i.e.*,

$$x = \sqrt{\frac{2P_{\mathrm{cap}}K_{\mathrm{B}}}{\mu}t} = \mathrm{G}\sqrt{t}. \tag{6.2}$$

The measured propagation distances are shown in Figure 6.4c as a function of time along with fittings of square root function (solid lines). Propagation coefficient G values derived from curve fittings (shown next to each curve) increase with the abrasive size, indicating a

silicon surface sandblasted by larger abrasives (up to 150 μm) can exhibit better surface wickability.

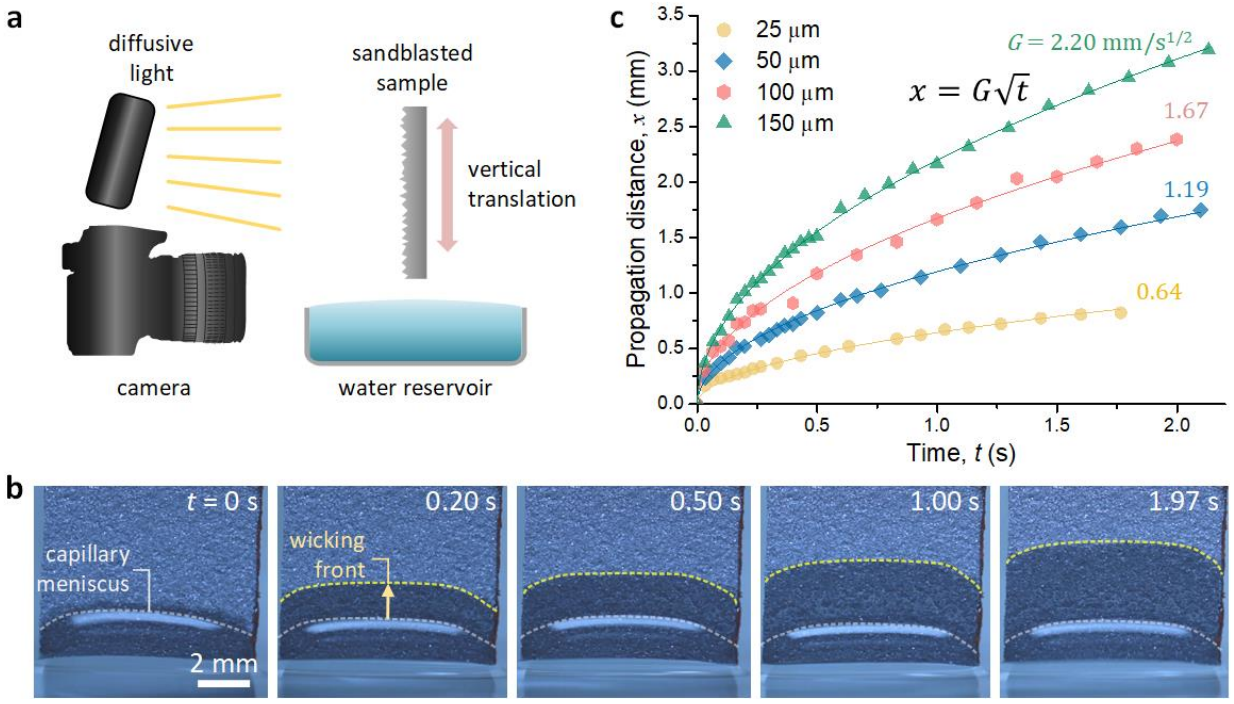

Figure 6.4. Surface wickability measurements of sandblasted surfaces. (a) Schematic of experimental setup for wickability measurement. A sandblasted surface is immersed vertically into the reservoir of water while a digital camera captures the speed of capillary rise at 30 frames per second. (b) Time-lapse images show an example of the wicking front of water on the surface sandblasted by 150 μm Al_2O_3 abrasives. (c) The propagation distance (x) of capillary rise plotted as a function of time (t). The data points and lines are experimental measurements and the fitting of square root functions, respectively. Propagation coefficient (G) for each surface are shown next to the corresponding case.

6.5 Results and discussion

Figure 6.5a shows pool boiling curves of a flat and sandblasted silicon surfaces. During the experiments, we gradually increased the input heat flux up to a CHF point, where thermal

runaway occurred as indicated with an arrow in the plot. HTC is also plotted as a function of heat flux in Figure 6.5b. All sandblasted surfaces demonstrated significant CHF and HTC enhancements compared to the flat surface. As the sandblasting abrasive size increased, CHF values monotonically increased from 65.1 W/cm^2 for the flat surface to 103.8, 135.0, 160.1, and 190.5 W/cm^2 for 25, 50, 100, and 150 μm abrasives, respectively, resulting up to 192.6% CHF enhancement. While there was a region ($\Delta T_W < \sim 25$°C), where the surface sandblasted by 50 μm abrasives showed higher HTC values than the surface sandblasted by 100 μm abrasives, HTC values at CHF points showed a similar trend with CHF, *i.e.*, an increase in HTC with increasing abrasive size. The maximum HTC value at CHF was 14.3 kW/m^2 for the flat silicon, which increased to 29.3, 41.6, 52.6, and 76.3 kW/m^2 for surfaces sandblasted by 25, 50, 100, and 150 μm abrasives, respectively, resulting in up to 433.6% enhancement. The CHF and HTC enhancements achieved with sandblasted silicon surfaces were comparable to that of clean-room processed surfaces [22, 24, 27, 132], indicating promise for the use of a sandblasting process as a scalable surface engineering technique for enhanced boiling heat transfer.

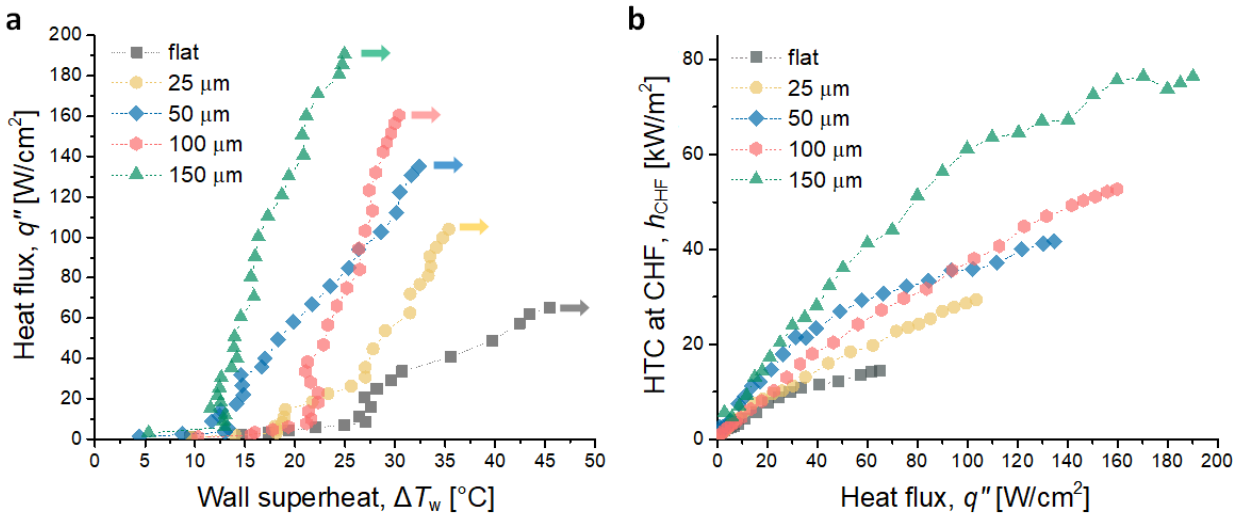

Figure 6.5. Pool boiling results of a flat and sandblasted silicon surfaces. (a) Pool boiling curves of water. (b) Heat transfer coefficient as a function of heat flux. The experimental uncertainty is smaller than the marker size.

In Chapter 4, we have shown that both thin film density (ξ) and volumetric wicking rate ($P_{\mathrm{cap}}K_{\mathrm{B}}h$, where h is the thickness of wick layer) are important structural features that affect the CHF enhancement of hemi-wicking surfaces, where CHF values show a positive linear correlation with the unified descriptor $\xi^{\mathrm{n}}P_{\mathrm{cap}}K_{\mathrm{B}}h$. Sandblasted surfaces have artificial nucleation sites such as cavities as opposed to micropillar arrays, which can exhibit more complex CHF enhancement mechanisms associated with the increased nucleation site density [132]. Nonetheless, CHF values of sandblasted surfaces exhibited a consistent monotonic increase with the unified descriptor as shown in Figure 5. Here we approximated $\xi^{\mathrm{n}}h$ as surface roughness r and $P_{\mathrm{cap}}K_{\mathrm{B}}$ is obtained from the capillary-rise test according to Darcy's law as $P_{\mathrm{cap}}K_{\mathrm{B}} = \mu G^2/2$, where μ is the dynamic viscosity of water.

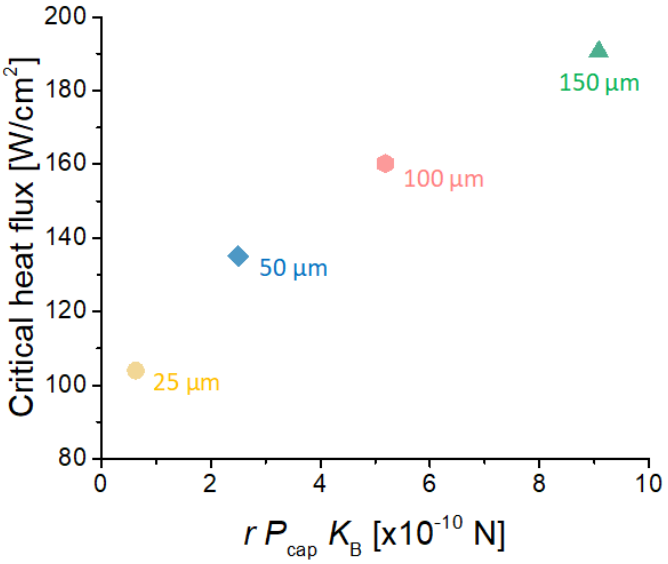

Figure 6.6. Relationship of critical heat flux with the unified descriptor ($rP_{cap}K_B$) of sandblasted surfaces. Sandblasting abrasive size is indicated next to each data point.

6.6 Summary

In this chapter, we tested uses of a sandblasting process as a surface engineering technique for enhancement of pool boiling heat transfer in industry-scale applications. We fabricated sandblasted silicon surfaces using Al_2O_3 abrasives with four different sizes, *i.e.*, 25, 50, 100, and 150 µm. The morphology of sandblasted surfaces was quantitatively characterized using an optical profilometer, all three types of roughness (r, R_a, and R_q) values increased noticeably as blasting abrasive size increased from 25 to 100 µm, while the difference of roughness parameters between 100 and 150 µm cases is marginal. Surface wickabilities characterized as a propagation coefficient of one-dimensional capillary flow show a gradually increasing trend with the increase of abrasive size. Pool boiling performance of sandblasted surfaces was characterized with high-purity deionized water at saturated atmospheric conditions. Sandblasted surfaces demonstrated significant CHF and HTC enhancements compared to a flat surface. The highest enhancement was achieved with the

surface sandblasted by 150 μm abrasives, where CHF and HTC were enhanced up to 192.6% and 433.6%, respectively. The relationship between structural properties and the CHF enhancement was consistent with the previous study: CHF increased with the unified descriptor associated with surface roughness and wickability. Furthermore, we expect that further enhancements can be achieved by investigating an optimal sandblasting condition. For example, we tested the abrasive size up to 150 μm in this study, but there can be an optimal abrasive size larger than 150 μm. In addition, an optimal boiling surface with higher roughness and volumetric wicking rate can be found through a parametric study including the other sandblasting parameters such as pressure (P), sweeping speed (v), line-pitch (p_l), and nozzle-to-sample distance (d_n). Nevertheless, the significant enhancement of boiling heat transfer demonstrated in this work promises the potential of a sandblasting process for industry-scale boiling applications.

Intentionally blank page

Chapter Seven

Concluding remarks

7.1 Thesis summary

This thesis focused on investigating the role of surface properties and structures on pool boiling heat transfer. Despite significant research in pool boiling heat transfer in the past decades, the large deviations of reported pool boiling CHF values on flat surfaces of the same material across the literature have not been investigated in detail. In Chapter 3, we first addressed this large discrepancy of CHF values by accounting for hydrocarbon adsorption and oxidation of metallic surfaces during boiling. Pool boiling results along with XPS analysis on SiO_2 surfaces showed that the hydrocarbon adsorption on a surface could lead to the decrease in CHF values due to decreased surface wettability. Even wider variations in reported CHF values on flat Cu and Ni surfaces cannot be explained by this hydrocarbon contamination alone. AFM and XPS analysis along with pool boiling experiments showed that the metallic surfaces could be oxidized during boiling, which led to changes in surface conditions and alterations of CHF values. Subsequently in Chapter 4, we investigated the effects of surface structures on enhanced CHF during pool boiling of hemi-wicking surfaces. The pool boiling results of systematically designed micropillar surfaces directly showed that the CHF enhancement on hemi-wicking surfaces cannot be attributed to a single parameter

such as roughness or wickability. We performed a scaling analysis to derive a relationship for CHF with a new unified descriptor, which represents the combined effects of the extended contact line length (which leads to the increase in thin film density) and volumetric wicking rate. The scaling analysis was confirmed with CHF values from our experiments and literature data. This work elucidates the distinct roles of thin film density and wickability in enhancing CHF values, which can enable improved designs of boiling surfaces for a variety of high heat flux applications.

Next, in Chapter 5, we engineered boiling surfaces to achieve simultaneous enhancement of CHF and HTC. We first developed a microtube structure, where a cavity is defined at the center of a pillar, as a structural building block to enhance the heat transfer characteristics in controllable manner. In addition to uniform microtube arrays, we designed a surface with microtube clusters interspersed with micropillars, referred to as tube-clusters in pillars (TIP), to mitigate the earlier boiling crisis of uniform microtube arrays due to the extensive bubble coalescence. While uniform microtube arrays and TIP surfaces showed significant enhancement of both CHF and HTC compared to a flat surface, there was an intrinsic trade-off between CHF and HTC associated with nucleation site density. We overcame this trade-off by incorporating nanostructures on top of TIP surfaces. This hierarchical TIP (h-TIP) surfaces control vapor nucleation with multi-scale structures while providing capillary wicking. These surfaces showed CHF and HTC enhancements up to 138 and 389%, respectively, compared to a flat surface. The enhanced boiling performance may provide significant energy savings and better safety in boiling applications. In addition, we expect, the extreme boiling performance achieved with h-TIP surfaces may open up unexplored opportunities in boiling applications that have been limited by boiling performance.

Finally, in Chapter 6, we investigated the use of sandblasting as a scalable surface engineering technique for enhanced pool boiling heat transfer for industry-scale

applications. Pool boiling results along with surface characterizations on silicon surfaces showed that surface roughness and volumetric wicking rates increased with the sandblasting abrasive size. All sandblasted surfaces demonstrated significant CHF and HTC enhancements compared to a flat surface. The highest enhancement was achieved with the surface sandblasted by 150 μm abrasives, where CHF and HTC were enhanced up to 192.6 and 433.6%, respectively. This enhancement is comparable to that of clean-room processed surfaces, which confirms the potential of sandblasting as a scalable surface structuring technique for enhanced boiling heat transfer.

This thesis provides important insights to understanding the role of surface properties and structures on pool boiling heat transfer, thereby providing guidelines for the surface preparation methods to achieve consistent measurements and the systematic design of surface structures for enhanced pool boiling heat transfer.

7.2 Future directions

The contributions of this thesis can be classified largely into two: (1) physical insights to the role of surface properties and structures and (2) surface structuring technique for enhanced boiling heat transfer. We expect that, in particular, the physical insights obtained in this thesis can be extended through two future studies. First, in Chapter 4, our scaling analysis showed that both surface thin film density, *i.e.*, structural packing density, and wickability are important parameters for enhanced CHF on hemi-wicking surfaces. This study can be further improved to a more accurate CHF prediction model by accounting for the effects of surface structures on stochastic bubble interactions (Figure 7.1). In fact, recent advancements in bubble visualization techniques combined with stochastic analysis of bubble interactions have shown that the boiling crisis is a percolatvie and scale-free

phenomenon [110]. This understanding enabled an accurate analysis of boiling curves by heat flux partitioning combined with experimentally measured fundamental boiling parameters, *e.g.*, bubble base diameter, growth time, departure frequency, and nucleation site density [159], which provides a solid connection between the right two panels in Figure 7.1. To achieve a boiling curve or CHF prediction model based on boiling surface features, we need a better understanding of the effects of surface properties and structures on fundamental boiling parameters, which connects the left two panels in Figure 7.1. A few studies have shown structural dependency of boiling parameters, however, they are often contradictory or applicable to limited regimes [116, 160]. Improved understanding on surface property and structural effects on the boiling parameters will ultimately lead to the prediction of boiling curves combined with the stochastic analysis.

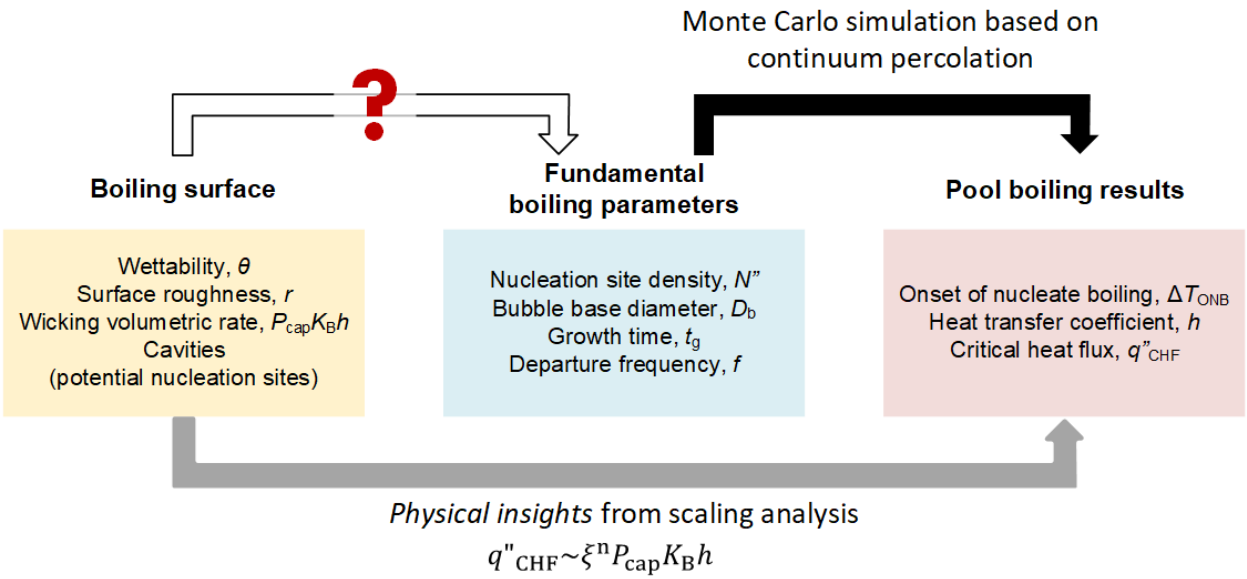

Figure 7.1. Path towards an accurate CHF prediction model.

A completely different approach to achieve the accurate prediction of boiling heat transfer is to harness recent advancements in machine learning (ML) technology. In fact, the

incorporation of ML models to boiling heat transfer has just kicked off. A few recent studies have improved our understanding of bubble dynamics and its effects on boiling heat transfer, *i.e.*, the connection between the right two panels of Figure 7.1, by harnessing ML models. For examples, ML models could predict a boiling curve or a boiling crisis with the imaging or sound of boiling bubbles as an input [161, 162]. These models may be used as an assistive tool to prevent the boiling crisis by the real-time characterization of boiling bubbles during operations; however, these ML models are not capable of predicting a boiling curve and boiling crisis before actually running the experiments. Instead, we expect the development of ML models that can understand the role of surface features on enhanced boiling heat transfer will be a disruptive innovation. This can be achieved, for example, by feeding a ML model with sufficient data sets of experimentally measured surface morphology with associated boiling curves, where the ML model will learn important surface features for boiling heat transfer. Once the ML model can predict a boiling curve with a surface profile as the sole input along with a substrate material-working fluid combination, it can ultimately be used to design an optimal boiling surface. The optimal surface designs without trial-and-error-based experiments or extensive computations may lead to significant innovations in ubiquitous boiling applications and the development of disruptive energy technologies.

Supplementary information

8.1 Capillary pressure calculations

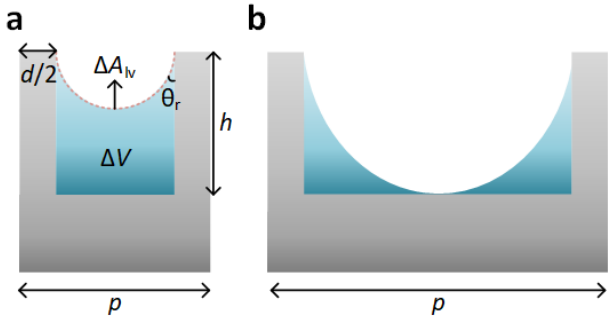

Figure 8.1. A unit cell of a micropillar array filled by liquid with the volume ΔV. The liquid pins at the top of the micropillar with the receding contact angle θ_r that creates a liquid-vapor interface with an area of ΔA_{lv}. (a) Dense micropillar arrays form the liquid-vapor meniscus above the bottom surface between micropillars. (b) Sparse micropillar arrays with the meniscus touching the bottom surface.

We determined the capillary pressure, P_{cap}, in square micropillar arrays using the thermodynamic approach [118]. When the liquid fills the micropillar array, it forms a meniscus shape that minimizes the free energy of the system. Here the capillary pressure can be expressed as

$$P_{cap} = -\Delta E/\Delta V, \tag{8.1}$$

where ΔE and ΔV are the free energy difference before and after the liquid filling the unit cell of micropillar arrays and the corresponding liquid volume filling the unit cell, respectively. The change in free energy is $\Delta E = \sigma_{sl}\Delta A_{sl} + \sigma_{sv}\Delta A_{sv} + \sigma_{lv}\Delta A_{lv}$, where σ_{sl}, σ_{sv}, and σ_{lv} are the interfacial energies at solid-liquid, solid-vapor, and liquid-vapor interfaces, respectively.

ΔA_{sl}, ΔA_{sv}, and ΔA_{lv} are the changes in solid-liquid, solid-vapor, and liquid-vapor interfacial areas before and after the liquid filling, respectively. As the liquid fills in the micropillar arrays, the liquid-vapor interface is created between pillars and the solid-vapor interface turns into the solid-liquid interface, *i.e.*, $\Delta A_{\mathrm{sl}} = -\Delta A_{\mathrm{sv}} = (rf)\pi dh + (p^2 - \frac{\pi d^2}{4})$, where d, h, and p are the diameter, height, and pitch of micropillar, respectively. rf is the roughness factor $\pi/2$ considering scallops created on the sidewalls from the etching process [118]. Combined with Young's equation $\sigma_{\mathrm{sv}} - \sigma_{\mathrm{sl}} = \sigma_{\mathrm{lv}} \cos\theta$, where θ is the intrinsic contact angle, Equation 8.1 can be expressed as

$$P_{cap} = -\frac{\Delta E}{\Delta V} = \frac{\sigma_{lv}[(rf)\cos\theta\,\pi dh + \cos\theta\,(p^2 - \pi d^2/4) - \Delta A_{lv}]}{\Delta V} \tag{8.2}$$

The shape of meniscus and corresponding ΔA_{lv} and ΔV are obtained from Surface Evolver simulation [118].

$$\begin{aligned}\Delta A_{\mathrm{lv}} = \left(p^2 - \frac{\pi d^2}{4}\right)\Bigg[&0.43 + 0.73(rf)\cos\theta + 3.76\left(\frac{d}{p}\right) - 0.046(rf\cos\theta)^2 - 5.53(rf\cos\theta)\left(\frac{d}{p}\right) - 4.05\left(\frac{d}{p}\right)^2 \\ &- 0.124(rf\cos\theta)^3 + 1.77(rf\cos\theta)^2\left(\frac{d}{p}\right) + 4.66(rf\cos\theta)\left(\frac{d}{p}\right)^2\Bigg]\end{aligned} \tag{8.3}$$

$$\begin{aligned}\Delta V = h\left(p^2 - \frac{\pi d^2}{4}\right) - \Bigg[&-0.175 - 0.345(rf)\cos\theta + 4.07\left(\frac{d}{p}\right) + 0.924(rf\cos\theta)^2 - 5.83(rf\cos\theta)\left(\frac{d}{p}\right) - 2.80\left(\frac{d}{p}\right)^2 \\ &- 0.439(rf\cos\theta)^3 + 2.41(rf\cos\theta)^2\left(\frac{d}{p}\right) + 2.71(rf\cos\theta)\left(\frac{d}{p}\right)^2\Bigg]\left(p^2 - \frac{\pi d^2}{4}\right)(p - d)\end{aligned} \tag{8.4}$$

Considering the maximum capillary pressure is exerted when the meniscus is fully stretched, we used the receding contact angle, θ_r, for θ in this capillary pressure evaluation. Equations 8.2 – 8.4 are valid when the liquid meniscus between pillars does not touch the bottom surface (Figure 8.1a). In the case of meniscus touching the bottom surface because of short height or large pitch of micropillar arrays (Figure 8.1b), *i.e.*, $h < \frac{p-d}{2\cos\theta_{\mathrm{r}}}$, we adopted a simplified P_{cap} expression by Hu et al [109].

$$P_{\mathrm{cap}} = \frac{\sigma_{\mathrm{lv}}(rf)\pi d\cos\theta}{p^2 - \pi d^2/4} - \frac{\sigma_{\mathrm{lv}}(\cos\theta - 1)r_{\mathrm{area}}}{h}, \tag{8.5}$$

where r_{area} is the ratio of the wetted area to the total area of the bottom surface. Approximating the non-wetted area as $\pi p^2/4$ results in $r_{\text{area}} = 1 - \frac{\pi p^2}{4(p^2 - \pi d^2/4)}$.

8.2 Permeability calculation

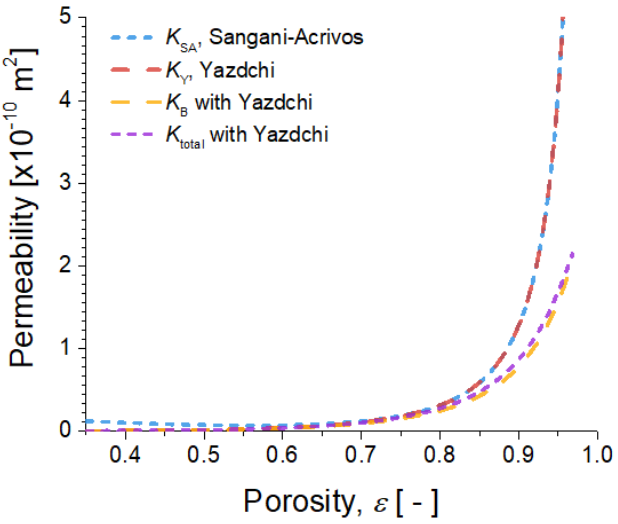

Figure 8.2. Comparison of permeability correlations over the wide porosity range. The correlation by Sangani and Acrivos, K_{SA}, overestimates the permeability in the low porosity range ($\varepsilon < 0.75$) compared with K_Y. K_B and K_{total} show a marginal difference to each other. Incorporation of the bottom shear stress becomes critical for the large porosity range ($\varepsilon > 0.8$). In the main text analysis, we use K_B as it shows the best agreement with experimental data.

We adopted the permeability correlation proposed by Yazdchi et al. [119], K_Y, that combines the correlations developed by Gebart et al., K_G^s (Equation 8.6) [120], and Drummond and Tahir, K_D^s (Equation 8.7) [121]. Yazdchi's correlation, K_Y (Equation 8.8), has shown a good agreement with experiments for the entire range of porosity, ε [122], where the porosity is calculated as $\varepsilon = 1 - \frac{\pi d^2}{4p^2}$ for square micropillar arrays.

$$K_{\mathrm{G}}^{S} = \frac{4d^2}{9\pi\sqrt{2}}\left(\sqrt{\frac{1-\varepsilon_{\mathrm{c}}}{1-\varepsilon}} - 1\right)^{5/2}, \text{where } \varepsilon_c = 1 - \pi/4 \tag{8.6}$$

$$K_{\mathrm{D}}^{S} = \frac{d^2}{32(1-\varepsilon)}\left[\ln\left(\frac{1}{1-\varepsilon}\right) - 1.476 + \frac{2(1-\varepsilon) - 0.796(1-\varepsilon)^2}{1 + 0.489(1-\varepsilon) - 1.605(1-\varepsilon)^2}\right] \tag{8.7}$$

$$K_{\mathrm{Y}} = K_{\mathrm{G2}}^{S} + (K_{\mathrm{D}}^{S} - K_{\mathrm{G2}}^{S})m(\varepsilon), \text{where } K_{\mathrm{G2}}^{S} = \frac{K_{\mathrm{G}}^{S}}{1+0.336(\varepsilon-\varepsilon_{\mathrm{c}})} \text{ and } m(\varepsilon) = \frac{1+\tanh(\frac{\varepsilon-0.75}{0.037})}{2}. \tag{8.8}$$

Since K_{Y} was developed for square pillar arrays with unbounded top and bottom conditions, an additional term is required to account for the shear stress from the bottom surface. The effective permeability, K_{B}, that incorporates the viscous resistances from the bottom surface and pillar sidewalls, can be derived in terms of K_{Y} by solving the Brinkman equation in the radial direction with a no-slip condition at the bottom surface as [109, 123]

$$K_{\mathrm{B}} = K_{\mathrm{Y}}\left[1 - \frac{\tanh(h\sqrt{\varepsilon/K_{\mathrm{Y}}})}{h\sqrt{\varepsilon/K_{\mathrm{Y}}}}\right] \tag{8.9}$$

Alternatively, we can also combine K_{Y} with the permeability of a flat surface, K_{plate}, to include the viscous resistance from the bottom surface. The combined permeability that is non-dimensionalized by d^2, K_{total}^{*} can be expressed as

$$K_{\mathrm{total}}^{*} = \left(\frac{1}{K_{\mathrm{Y}}^{*}} + \frac{1}{K_{\mathrm{plate}}^{*}}\right)^{-1}, \tag{8.10}$$

where $K_{\mathrm{plate}}^{*} = \frac{1}{3}\left(\frac{h}{d}\right)^2 \varepsilon$ [163]. In Figures 8.2, we compare the permeability correlations proposed by Yazdchi (K_{Y}) with Sangani and Acrivos (K_{SA}) [164], which is a widely used correlation for large porosity cases ($\varepsilon > 0.75$). The plot shows that K_{SA} overestimates the permeability in the low porosity range ($\varepsilon < 0.75$) compared with K_{Y}. We also compare K_{B} and K_{total}, which shows a marginal difference to each other. The plot shows that both K_{B} and K_{total} effectively account for the shear stress from the bottom surface, especially when the bottom shear stress becomes dominant over the viscous resistance from the pillar sidewalls in the large porosity range ($\varepsilon > 0.8$). In the main text analysis, we use K_{B} as an effective

permeability of micropillar surfaces as it shows the best agreement with experimental data [109, 122].

8.3 Fabrication of microscale structured surfaces

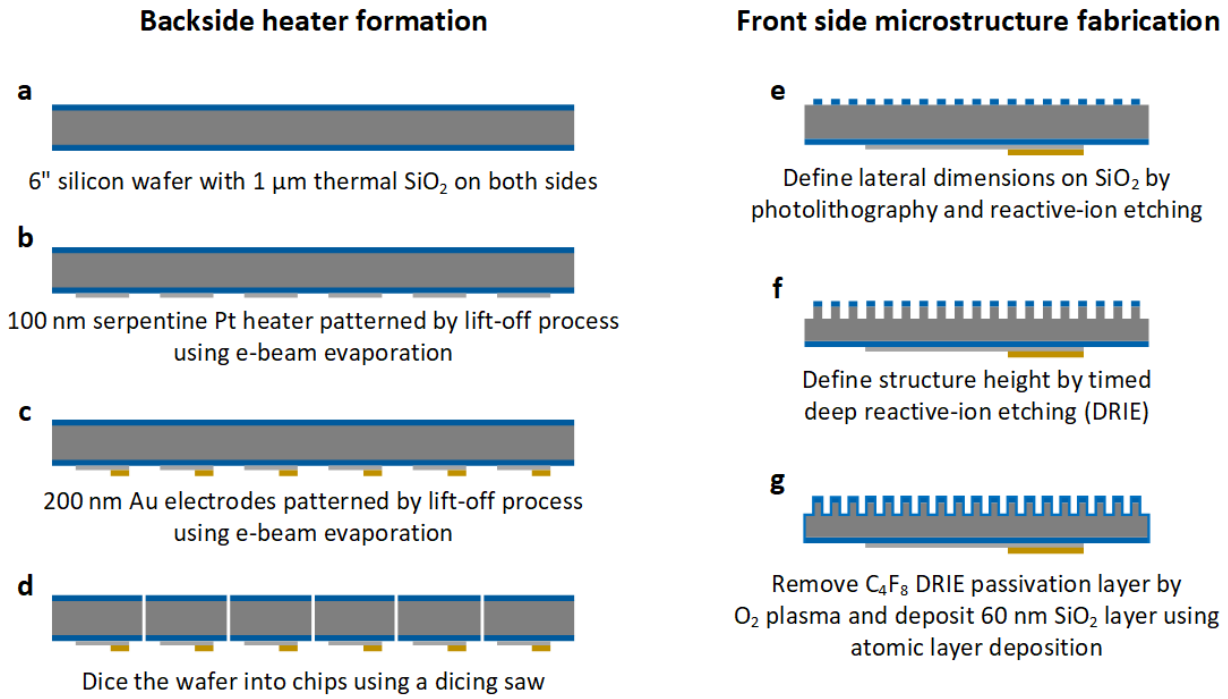

Figure 8.3. Fabrication flow chart of microscale structured surfaces (not to scale). (a – d) Thin-film heaters were first created on the backside of a silicon wafer by lift-off processes. (e – g) Microstructurs were fabricated on the front side of each sample using photolithography, reactive-ion etching, and deep reactive-ion etching, and atomic layer deposition of SiO_2 layer.

All silicon-based samples were fabricated based on six-inch silicon wafers covered with 1 µm thermal SiO_2 on both sides (Figure 8.3a). First, Pt serpentine heaters and Au electrodes were patterned on the backside of the wafers. A ~1 µm photoresist (SPR 700, Microposit) layer was spin coated with 3600 rpm for 30 seconds followed by the prebaking in a box

furnace at 95 ℃ for 30 min. The photoresist was exposed to define serpentine heater patterns using a Heidelberg MLA150 Maskless Aligner. The resist was then developed (CD26, Microposit). A 100 nm Pt layer was deposited with a 10 nm Ti adhesion layer underneath by an e-beam evaporation. The whole wafers were then immersed in the acetone bath with sonication for the lift-off process, which completed the Pt serpentine heater formation (Figure 8.3b). On top of the serpentine heaters, 200 nm Au electrodes were created through the same lift-off process (Figure 8.3c). After creating the heater and electrodes, the wafers were cut into boiling samples (12×18.5 mm^2 for Chapter 4 and 20×20 mm^2 for the other chapters) using a dicing machine (Figure 8.3d).

Microstructures were fabricated on the front side. Using the same photolithography process, a photoresist layer was patterned to define the lateral dimensions of microstructures, *e.g.,* diameter, pitch, and cavity diameter. The photoresist patterns were then transferred into the underlying SiO_2 layer by a reactive-ion etching (RIE) process (Precision 5000, Applied Materials) with CF_4 as a primary gas (Figure 8.3e). Then, the microstructures were etched in the bulk silicon with deep reactive-ion etching (DRIE, MESC Multiplex ICP, STS) based on SF_6 and C_4F_8 (Figure 8.3f). The micropillar height was controlled by a timed etch on a sample-by-sample basis. The processed samples were loaded into the RIE chamber again to remove the C_4F_8 DRIE passivation layers and organic contaminants by O_2 plasma. Finally, a 60 nm SiO_2 layer (20 nm for Chapter 5.3) was deposited over the entire surfaces by atomic layer deposition (Figure 8.3g).

8.4 Literature surveys

8.4.1 CHF values on flat surfaces

CHF values used in Figure 3.1 are summarized in Table 8.1.

Table 8.1. CHF values of saturated pool boiling of water on flat Ni, Cu, Si, and SiO_2 surfaces.

Material	$q"_{CHF}$ [W/cm^2]	Reference
Ni	78	M. M. Rahman et al. [39]
Ni	81	Y.-Y. Li et al. [51]
Ni	84	E. Forrest et al. [52]
Ni	105	Y. H. Maeng et al. [53]
Ni	150	W. Bailey et al. [54]
Ni	168	H. Kim et al. [55]
Cu	60	J. S. Coursey and J. Kim [56]
Cu	92	A. M. Gheitaghy et al. [57]
Cu	100	S. Mori et al. [58]
Cu	101	S. M. Kawrk et al. [59]
Cu	110	L. Liao et al. [60]
Cu	110	N. Zuber [61]
Cu	112	G. Chen and C. H. Li [62]
Cu	116	C. H. Li and R. P. Rioux [63]
Cu	120	M. M. Rahman et al. [64]
Cu	121	W. Wu et al. [65]
Cu	135	Y. Takata et al. [66]
Cu	139	H. Auracher and W. Marquardt [67]
Cu	142	C. H. Li and G. P. Peterson [68]

Cu	150	C. Li and G. P. Peterson [69]
Cu	157	L. Bai et al. [70]
Si	67	Z. Yao et al. [38]
Si	70	S. H. Kim et al. [40]
Si	88	D. I. Shim et al. [29]
Si	89	A. Zou and S. C. Maroo [41]
Si	91	B. S. Kim et al. [42]
Si	93	R. Chen et al. [43]
Si	100	N. S. Dhillon et al. [27]
SiO_2	58	A. R. Betz et al. [21]
SiO_2	65	A. R. Betz et al. [44]
SiO_2	67	H. S. Ahn et al. [45]
SiO_2	78	K.-H. Chu et al. [24]
SiO_2	79	A. Zou et al. [46]
SiO_2	80	H. Jo et al. [47]
SiO_2	80	H. S. Ahn et al. [48]
SiO_2	80	H. Seo et al. [49]
SiO_2	81	H. Jo et al. [31]
SiO_2	100	D. E. Kim et al. [22]
SiO_2	101	H. O'Hanley et al. [50]
SiO_2	107	R. Chen et al. [43]

8.4.2 CHF values of hemi-wicking surfaces

All data used in Figure 4.1 are summarized in Table 8.2. We collected the literature data that are based on Si and SiO_2 and satisfy the hemi-wicking criterion.

Table 8.2. CHF values of saturated pool boiling of water on Si and SiO_2 hemi-wicking surfaces.

Ref	Material properties		Micropillar structure			Structural effects			Boiling
	Material	θ_{rec} [deg]	d [μm]	p [μm]	h [μm]	Hemi-wicking	r [-]	$P_{cap}K_B h$ [$\times 10^{-12}$ N·m]	q''_{CHF} [W/cm²]
This work	SiO_2	10	flat						99.45
			4	20	30	Yes	1.94	4.56	213
			7	25	30	Yes	2.06	6.06	237
			12	30	30	Yes	2.26	7.24	251
			3	23	30	Yes	1.53	3.41	164.5
			11	23	30	Yes	2.96	6.26	231
			3	6	30	Yes	8.85	4.56	170.5
			8	30	30	Yes	1.84	6.25	215
K.-H. Chu [24]	SiO_2	0	Flat						77
			10	25	10	Yes	1.50	1.17	160
			10	25	20	Yes	2.00	2.09	165
			5	15	20	Yes	2.40	1.31	171
			10	20	20	Yes	2.57	1.51	195
			10	15	20	Yes	3.79	0.65	207
			5	10	20	Yes	4.14	0.73	210
D. E. Kim [108]	SiO_2	20**	Flat						110
			4	8	20	Yes	4.93	0.54	148.3
			4	16	20	Yes	1.98	1.22	212.2
			8	16	20	Yes	2.96	1.06	180.5
			8	32	20	Yes	1.49	1.90	200
			40	80	20	Yes	1.39	2.29	184.3
			40	160	20	Yes	1.10	1.11	129.3
			80	160	20	Yes	1.20	1.83	170.7

			80	320	20	*No****	1.05	-	112.5
D. I. Yu [117]	SiO_2	20	Flat						84.2
			40	80	20	Yes	1.39	2.29	187.7
			40	160	20	Yes	1.10	1.11	101.3
			80	160	20	Yes	1.20	1.83	148.5
			80	320	20	*No****	1.05	-	96.4
N. S. Dhillon [27]*	Si	30	Flat						100
			10	11.7	15.6	Yes	5.56	0.12	130
			10	13	17.1	Yes	5.05	0.24	140
			10	12.6	16.4	Yes	5.13	0.20	155
			10	15.5	12.2	Yes	3.03	0.32	171
			10	15.1	12.1	Yes	3.12	0.29	169
			10	20.9	11.2	Yes	2.02	0.50	160
			10	20.4	10.7	Yes	2.03	0.45	187
			10	35.6	10.3	Yes	1.32	0.26	150
			10	35.4	10.2	Yes	1.32	0.26	140
S. H. Kim [116]	Si	61.7**	Flat						70
			20	25	10	Yes	2.00	0.06	70
			20	40	10	*No****	1.39	-	105
			20	60	10	*No****	1.17	-	80
			20	25	20	Yes	3.01	0.16	131.8
			20	40	20	*No****	1.78	-	170
			20	60	20	*No****	1.35	-	120
			20	25	40	Yes	5.02	0.37	156.9
			20	40	40	Yes	2.57	1.56	216.5
			20	60	40	*No****	1.70	-	152
			5	10	20	Yes	4.14	0.27	163
			5	15	20	Yes	2.40	0.31	187
			5	25	20	*No****	1.50	-	125

* Dhillon et al. used square (not cylindrical) micropillar arrays. P_{cap} and K_B were calculated based on the equations presented in their paper.

** The contact angle value at the saturation condition was not reported. We determined the value by matching the CHF on a flat surface with the contact angle-based CHF model [15].

***Surfaces not satisfying the hemi-wicking criterion were not included in the plots.

8.4.3 CHF and HTC values of structured surfaces

All data used in Figure 5.8 are summarized in Table 8.3.

Table 8.3. CHF and HTC values of different micro/nano structures

Material	Structure	q''_{CHF} [W/cm²]	h_{max} [kW/m²K]	Reference
SiO_2	Microtube 5 μm	173	67	Chapter 5.2
SiO_2	Microtube 12 μm	168	73	
SiO_2	TIP 5 μm	255	64	
SiO_2	TIP 12 μm	245	58	
SiO_2	Micropillar	228	55	
SiO_2	Microcavity	113	63	
SiO_2	Microcavity	109	67	
SiO_2	h-TIP 5 μm	256	82	Chapter 5.3
SiO_2	h-TIP 12 μm	242	103	
SiO_2	h-Tube 5 μm	192	95	
SiO_2	h-Tube 12 μm	196	115	
SiO_2	Micropillar	210	53	K.-H. Chu et al. [24]
SiO_2	Micropillar	170	48	
SiO_2	Micropillar	203	48	
SiO_2	Micropillar	191	59	
SiO_2	Micropillar	167	69	
SiO_2	Micropillar	132	37	S. H. Kim et al. [142]
SiO_2	Micropillar	171	35	
SiO_2	Micropillar	117	25	
SiO_2	Micropillar	153	49	
SiO_2	Micropillar	216	40	
SiO_2	Micropillar	119	22	
SiO_2	Micropillar	161	45	
SiO_2	Micropillar	189	40	

SiO_2	Micropillar	125	24	
SiO_2	Hierarchical pillar	235	35	K.-H. Chu et al. [34]
SiO_2	Hierarchical pillar	233	79	
Si	Nanowire	198	75	R. Chen et al.[43]
Si	Nanowire	203	52	B. Kim et al.[42]
Si	Nanowire	162	56	M. Lu et al. [144]
Si	Nanowire	162	50	
Si	Nanowire	134	58	Z. Yao et al. [38]
Si	Nanowire	115	46	
SiO_2	Microcavity	100	55	D. Kim et al. [22]
SiO_2	Microchannel	154	44	
SiO_2	Microchannel	132	31	H. Kim et al. [105]
SiO_2	Microchannel	139	34	
SiO_2	Microchannel	154	38	
SiO_2	Microchannel	165	41	
SiO_2	Microridge	180	75	A. Zou et al. [46]
SiO_2	Microridge	172	67	
SiO_2	Microridge	110	41	
SiO_2	Microridge	127	38	
SiO_2	Microridge	164	63	
SiO_2	Microridge	91	33	
SiO_2	Microridge	91	29	
SiO_2	Microridge	120	38	
SiO_2	Microridge	160	62	
SiO_2	Microridge	101	41	
SiO_2	Microridge	103	32	
SiO_2	Microridge	150	52	
SiO_2	Microridge	179	52	

Intentionally blank page

Bibliography

[1] Bp statistical review of world energy 2020, BP p.l.c, London, UK, 2021.
[2] Annual energy outlook 2020, Washington, DC, 2020.
[3] T. Mattila-Sandholm, G. Wirtanen, Biofilm formation in the industry: A review, Food Rev. Int., 8(4) (1992) 573-603.
[4] A. Haryanto, S. Fernando, N. Murali, S. Adhikari, Current status of hydrogen production techniques by steam reforming of ethanol: A review, Energy & Fuels, 19(5) (2005) 2098-2106.
[5] T. Humplik, J. Lee, S.C. O'Hern, B.A. Fellman, M.A. Baig, S.F. Hassan, M.A. Atieh, F. Rahman, T. Laoui, R. Karnik, E.N. Wang, Nanostructured materials for water desalination, Nanotechnology, 22(29) (2011) 292001.
[6] J.D. Hansen, J.A. Johnson, D.A. Winter, History and use of heat in pest control: A review, Int. J. Pest Manage., 57(4) (2011) 267-289.
[7] A. Royne, C.J. Dey, D.R. Mills, Cooling of photovoltaic cells under concentrated illumination: A critical review, Sol. Energy Mater. Sol. Cells, 86(4) (2005) 451-483.
[8] Y. Liu, Y. Zhu, Y. Cui, Challenges and opportunities towards fast-charging battery materials, Nature Energy, 4(7) (2019) 540-550.
[9] K. Ebrahimi, G.F. Jones, A.S. Fleischer, A review of data center cooling technology, operating conditions and the corresponding low-grade waste heat recovery opportunities, Renewable and Sustainable Energy Reviews, 31 (2014) 622-638.
[10] L.L. Vasiliev, Heat pipes in modern heat exchangers, Appl. Therm. Eng., 25(1) (2005) 1-19.
[11] S. Nukiyama, The maximum and minimum values of the heat q transmitted from metal to boiling water under atmospheric pressure, J. Jpn. Soc. Mech. Eng., 37 (1934) 367-374.
[12] H.J. Cho, D.J. Preston, Y. Zhu, E.N. Wang, Nanoengineered materials for liquid–vapour phase-change heat transfer, Nat. Rev. Mater., 2(2) (2016) 16092.
[13] D.J. Preston, D.L. Mafra, N. Miljkovic, J. Kong, E.N. Wang, Scalable graphene coatings for enhanced condensation heat transfer, Nano Lett., 15(5) (2015) 2902-2909.
[14] K.L. Wilke, D.J. Preston, Z. Lu, E.N. Wang, Toward condensation-resistant omniphobic surfaces, ACS Nano, 12(11) (2018) 11013-11021.
[15] S.G. Kandlikar, A theoretical model to predict pool boiling chf incorporating effects of contact angle and orientation, J. Heat Transfer, 123(6) (2001) 1071-1079.
[16] I.L. Pioro, W. Rohsenow, S.S. Doerffer, Nucleate pool-boiling heat transfer. I: Review of parametric effects of boiling surface, Int. J. Heat Mass Transfer, 47(23) (2004) 5033-5044.
[17] Y. Nam, E. Aktinol, V.K. Dhir, Y.S. Ju, Single bubble dynamics on a superhydrophilic surface with artificial nucleation sites, Int. J. Heat Mass Transfer, 54(7) (2011) 1572-1577.
[18] L. Cheng, D. Mewes, A. Luke, Boiling phenomena with surfactants and polymeric additives: A state-of-the-art review, Int. J. Heat Mass Transfer, 50(13) (2007) 2744-2771.

[19] H.J. Cho, D.J. Preston, Y. Zhu, E.N. Wang, Nanoengineered materials for liquid–vapour phase-change heat transfer, Nat. Rev. Mater., 2 (2016) 16092.
[20] Y. Liu, J. Tang, L. Li, Y.N. Shek, D. Xu, Design of cassie-wetting nucleation sites in pool boiling, Int. J. Heat Mass Transfer, 132 (2019) 25-33.
[21] A.R. Betz, J. Jenkins, C.-J.C. Kim, D. Attinger, Boiling heat transfer on superhydrophilic, superhydrophobic, and superbiphilic surfaces, Int. J. Heat Mass Transfer, 57(2) (2013) 733-741.
[22] D.E. Kim, S.C. Park, D.I. Yu, M.H. Kim, H.S. Ahn, Enhanced critical heat flux by capillary driven liquid flow on the well-designed surface, Appl. Phys. Lett., 107(2) (2015) 023903.
[23] C.K. Yu, D.C. Lu, T.C. Cheng, Pool boiling heat transfer on artificial micro-cavity surfaces in dielectric fluid fc-72, J. Micromech. Microeng., 16(10) (2006) 2092-2099.
[24] K.-H. Chu, R. Enright, E.N. Wang, Structured surfaces for enhanced pool boiling heat transfer, Appl. Phys. Lett., 100(24) (2012) 241603.
[25] H.S. Ahn, H.J. Jo, S.H. Kang, M.H. Kim, Effect of liquid spreading due to nano/microstructures on the critical heat flux during pool boiling, Appl. Phys. Lett., 98(7) (2011) 071908.
[26] M.M. Rahman, E. Ölçeroğlu, M. McCarthy, Role of wickability on the critical heat flux of structured superhydrophilic surfaces, Langmuir, 30(37) (2014) 11225-11234.
[27] N.S. Dhillon, J. Buongiorno, K.K. Varanasi, Critical heat flux maxima during boiling crisis on textured surfaces, Nat. Commun., 6 (2015) 8247.
[28] Q.N. Pham, S. Zhang, S. Hao, K. Montazeri, C.-H. Lin, J. Lee, A. Mohraz, Y. Won, Boiling heat transfer with a well-ordered microporous architecture, ACS Appl. Mater. Interfaces, 12(16) (2020) 19174-19183.
[29] D.I. Shim, G. Choi, N. Lee, T. Kim, B.S. Kim, H.H. Cho, Enhancement of pool boiling heat transfer using aligned silicon nanowire arrays, ACS Appl. Mater. Interfaces, 9(20) (2017) 17595-17602.
[30] H.S. Ahn, G. Park, J.M. Kim, J. Kim, M.H. Kim, The effect of water absorption on critical heat flux enhancement during pool boiling, Exp. Therm Fluid Sci., 42 (2012) 187-195.
[31] H. Jo, D.I. Yu, H. Noh, H.S. Park, M.H. Kim, Boiling on spatially controlled heterogeneous surfaces: Wettability patterns on microstructures, Appl. Phys. Lett., 106(18) (2015) 181602.
[32] G. Choi, D.I. Shim, D. Lee, B.S. Kim, H.H. Cho, Enhanced nucleate boiling using a reduced graphene oxide-coated micropillar, Int. Commun. Heat Mass Transfer, 109 (2019) 104331.
[33] C.M. Patil, S.G. Kandlikar, Pool boiling enhancement through microporous coatings selectively electrodeposited on fin tops of open microchannels, Int. J. Heat Mass Transfer, 79 (2014) 816-828.
[34] K.-H. Chu, Y. Soo Joung, R. Enright, C.R. Buie, E.N. Wang, Hierarchically structured surfaces for boiling critical heat flux enhancement, Appl. Phys. Lett., 102(15) (2013) 151602.
[35] M. Može, M. Senegačnik, P. Gregorčič, M. Hočevar, M. Zupančič, I. Golobič, Laser-engineered microcavity surfaces with a nanoscale superhydrophobic coating for extreme boiling performance, ACS Appl. Mater. Interfaces, 12(21) (2020) 24419-24431.
[36] B.N. Taylor, C.E. Kuyatt, Guidelines for evaluating and expressing the uncertainty of nist measurement results, nist technical note 1297, in, National Institute of Standards and Technology, Gaithersburg, MD, 1994.
[37] M. Može, M. Zupančič, I. Golobič, Investigation of the scatter in reported pool boiling chf measurements including analysis of heat flux and measurement uncertainty evaluation methodology, Appl. Therm. Eng., 169 (2020) 114938.

[38] Z. Yao, Y.W. Lu, S.G. Kandlikar, Effects of nanowire height on pool boiling performance of water on silicon chips, Int. J. Therm. Sci., 50(11) (2011) 2084-2090.
[39] M.M. Rahman, E. Ölçeroğlu, M. McCarthy, Scalable nanomanufacturing of virus-templated coatings for enhanced boiling, Adv. Mater. Interfaces, 1(2) (2014) 1300107.
[40] S.H. Kim, G.C. Lee, J.Y. Kang, K. Moriyama, M.H. Kim, H.S. Park, Boiling heat transfer and critical heat flux evaluation of the pool boiling on micro structured surface, Int. J. Heat Mass Transfer, 91(Supplement C) (2015) 1140-1147.
[41] A. Zou, S.C. Maroo, Critical height of micro/nano structures for pool boiling heat transfer enhancement, Appl. Phys. Lett., 103(22) (2013) 221602.
[42] B.S. Kim, H. Lee, S. Shin, G. Choi, H.H. Cho, Interfacial wicking dynamics and its impact on critical heat flux of boiling heat transfer, Appl. Phys. Lett., 105(19) (2014) 191601.
[43] R. Chen, M.-C. Lu, V. Srinivasan, Z. Wang, H.H. Cho, A. Majumdar, Nanowires for enhanced boiling heat transfer, Nano Lett., 9(2) (2009) 548-553.
[44] A.R. Betz, J. Xu, H. Qiu, D. Attinger, Do surfaces with mixed hydrophilic and hydrophobic areas enhance pool boiling?, Appl. Phys. Lett., 97(14) (2010) 141909.
[45] H.S. Ahn, J.M. Kim, M. Kaviany, M.H. Kim, Pool boiling experiments in reduced graphene oxide colloids. Part i – boiling characteristics, Int. J. Heat Mass Transfer, 74 (2014) 501-512.
[46] A. Zou, D.P. Singh, S.C. Maroo, Early evaporation of microlayer for boiling heat transfer enhancement, Langmuir, 32(42) (2016) 10808-10814.
[47] H. Jo, S. Kim, H.S. Park, M.H. Kim, Critical heat flux and nucleate boiling on several heterogeneous wetting surfaces: Controlled hydrophobic patterns on a hydrophilic substrate, Int. J. Multiphase Flow, 62 (2014) 101-109.
[48] H.S. Ahn, J.M. Kim, C. Park, J.-W. Jang, J.S. Lee, H. Kim, M. Kaviany, M.H. Kim, A novel role of three dimensional graphene foam to prevent heater failure during boiling, Sci. Rep., 3 (2013) 1960.
[49] H. Seo, Y. Lim, H. Shin, I.C. Bang, Effects of hole patterns on surface temperature distributions in pool boiling, Int. J. Heat Mass Transfer, 120 (2018) 587-596.
[50] H. O'Hanley, C. Coyle, J. Buongiorno, T. McKrell, L.-W. Hu, M. Rubner, R. Cohen, Separate effects of surface roughness, wettability, and porosity on the boiling critical heat flux, Appl. Phys. Lett., 103(2) (2013) 024102.
[51] Y.-Y. Li, Z.-H. Liu, B.-C. Zheng, Experimental study on the saturated pool boiling heat transfer on nano-scale modification surface, Int. J. Heat Mass Transfer, 84 (2015) 550-561.
[52] E. Forrest, E. Williamson, J. Buongiorno, L.-W. Hu, M. Rubner, R. Cohen, Augmentation of nucleate boiling heat transfer and critical heat flux using nanoparticle thin-film coatings, Int. J. Heat Mass Transfer, 53(1) (2010) 58-67.
[53] Y.H. Maeng, S.L. Song, J.Y. Lee, Unaffectedness of improved wettability on critical heat flux enhancement with tio2 sputtered surface, Appl. Phys. Lett., 108(7) (2016) 074101.
[54] W. Bailey, E. Young, C. Beduz, Y. Yang, Pool boiling study on candidature of pentane, methanol and water for near room temperature cooling, in: Thermal and Thermomechanical Proceedings 10th Intersociety Conference on Phenomena in Electronics Systems, 2006. ITHERM 2006., 2006, pp. 599-603.
[55] H. Kim, H.S. Ahn, M.H. Kim, On the mechanism of pool boiling critical heat flux enhancement in nanofluids, J. Heat Transfer, 132(6) (2010).
[56] J.S. Coursey, J. Kim, Nanofluid boiling: The effect of surface wettability, Int. J. Heat Fluid Flow, 29(6) (2008) 1577-1585.

[57] A.M. Gheitaghy, A. Samimi, H. Saffari, Surface structuring with inclined minichannels for pool boiling improvement, Appl. Therm. Eng., 126 (2017) 892-902.
[58] S. Mori, S. Mt Aznam, K. Okuyama, Enhancement of the critical heat flux in saturated pool boiling of water by nanoparticle-coating and a honeycomb porous plate, Int. J. Heat Mass Transfer, 80 (2015) 1-6.
[59] S.M. Kwark, G. Moreno, R. Kumar, H. Moon, S.M. You, Nanocoating characterization in pool boiling heat transfer of pure water, Int. J. Heat Mass Transfer, 53(21) (2010) 4579-4587.
[60] L. Liao, R. Bao, Z. Liu, Compositive effects of orientation and contact angle on critical heat flux in pool boiling of water, Heat Mass Transfer., 44(12) (2008) 1447-1453.
[61] N. Zuber, Hydrodynamic aspects of boiling heat transfer, Ph.D. Thesis, University of California, Los Angeles, Los Angeles, California, USA, 1959.
[62] G. Chen, C.H. Li, Combined effects of liquid wicking and hydrodynamic instability on pool boiling critical heat flux by two-tier copper structures of nanowires and microgrooves, Int. J. Heat Mass Transfer, 129 (2019) 1222-1231.
[63] C.H. Li, R.P. Rioux, Independent and collective roles of surface structures at different length scales on pool boiling heat transfer, Sci. Rep., 6(1) (2016) 37044.
[64] M.M. Rahman, J. Pollack, M. McCarthy, Increasing boiling heat transfer using low conductivity materials, Sci. Rep., 5 (2015) 13145.
[65] W. Wu, H. Bostanci, L.C. Chow, Y. Hong, M. Su, J.P. Kizito, Nucleate boiling heat transfer enhancement for water and fc-72 on titanium oxide and silicon oxide surfaces, Int. J. Heat Mass Transfer, 53(9) (2010) 1773-1777.
[66] Y. Takata, S. Hidaka, M. Masuda, T. Ito, Pool boiling on a superhydrophilic surface, International Journal of Energy Research, 27(2) (2003) 111-119.
[67] H. Auracher, W. Marquardt, Experimental studies of boiling mechanisms in all boiling regimes under steady-state and transient conditions, Int. J. Therm. Sci., 41(7) (2002) 586-598.
[68] C.H. Li, G. Peterson, Experimental study of enhanced nucleate boiling heat transfer on uniform and modulated porous structures, Frontiers in Heat and Mass Transfer, 1 (2010).
[69] C. Li, G.P. Peterson, Parametric study of pool boiling on horizontal highly conductive microporous coated surfaces, J. Heat Transfer, 129(11) (2007) 1465-1475.
[70] L. Bai, L. Zhang, G. Lin, G.P. Peterson, Pool boiling with high heat flux enabled by a porous artery structure, Appl. Phys. Lett., 108(23) (2016) 233901.
[71] M.L. White, The detection and control of organic contaminants on surfaces, Marcel Dekker, New York, 1970.
[72] R.A. Erb, Wettability of metals under continuous condensing conditions, J. Phys. Chem., 69(4) (1965) 1306-1309.
[73] F.M. Fowkes, Attractive forces at interfaces, Ind. Eng. Chem., 56(12) (1964) 40-52.
[74] K.W. Bewig, W.A. Zisman, The wetting of gold and platinum by water, J. Phys. Chem., 69(12) (1965) 4238-4242.
[75] M.K. Bernett, W.A. Zisman, Confirmation of spontaneous spreading by water on pure gold, J. Phys. Chem., 74(11) (1970) 2309-2312.
[76] T. Smith, The hydrophilic nature of a clean gold surface, J. Colloid Interface Sci., 75(1) (1980) 51-55.
[77] G.L. Gaines, On the water wettability of gold, J. Colloid Interface Sci., 79(1) (1981) 295.
[78] M.E. Schrader, Wettability of clean metal surfaces, J. Colloid Interface Sci., 100(2) (1984) 372-380.

[79] S. Takeda, M. Fukawa, Y. Hayashi, K. Matsumoto, Surface oh group governing adsorption properties of metal oxide films, Thin Solid Films, 339(1) (1999) 220-224.
[80] B.R. Strohmeier, The effects of o2 plasma treatments on the surface composition and wettability of cold-rolled aluminum foil, J. Vac. Sci. Technol., A, 7(6) (1989) 3238-3245.
[81] P. Gregorčič, Comment on "bioinspired reversible switch between underwater superoleophobicity/superaerophobicity and oleophilicity/aerophilicity and improved antireflective property on the nanosecond laser-ablated superhydrophobic titanium surfaces", ACS Appl. Mater. Interfaces, (2020).
[82] A. Seshadri, E.C. Forrest, K. Shirvan, Why ionizing radiation enhances surface wettability, Appl. Surf. Sci., 514 (2020) 145935.
[83] D.V. Ta, A. Dunn, T.J. Wasley, R.W. Kay, J. Stringer, P.J. Smith, C. Connaughton, J.D. Shephard, Nanosecond laser textured superhydrophobic metallic surfaces and their chemical sensing applications, Appl. Surf. Sci., 357 (2015) 248-254.
[84] L.B. Boinovich, A.M. Emelyanenko, K.A. Emelyanenko, A.G. Domantovsky, A.A. Shiryaev, Comment on "nanosecond laser textured superhydrophobic metallic surfaces and their chemical sensing applications" by duong v. Ta, andrew dunn, thomas j. Wasley, robert w. Kay, jonathan stringer, patrick j. Smith, colm connaughton, jonathan d. Shephard (appl. Surf. Sci. 357 (2015) 248–254), Appl. Surf. Sci., 379 (2016) 111-113.
[85] J. Long, M. Zhong, P. Fan, D. Gong, H. Zhang, Wettability conversion of ultrafast laser structured copper surface, J. Laser Appl., 27(S2) (2015) S29107.
[86] V.D. Ta, A. Dunn, T.J. Wasley, J. Li, R.W. Kay, J. Stringer, P.J. Smith, E. Esenturk, C. Connaughton, J.D. Shephard, Laser textured surface gradients, Appl. Surf. Sci., 371 (2016) 583-589.
[87] X. Yan, Z. Huang, S. Sett, J. Oh, H. Cha, L. Li, L. Feng, Y. Wu, C. Zhao, D. Orejon, F. Chen, N. Miljkovic, Atmosphere-mediated superhydrophobicity of rationally designed micro/nanostructured surfaces, ACS Nano, 13(4) (2019) 4160-4173.
[88] Z. Li, Y. Wang, A. Kozbial, G. Shenoy, F. Zhou, R. McGinley, P. Ireland, B. Morganstein, A. Kunkel, S.P. Surwade, L. Li, H. Liu, Effect of airborne contaminants on the wettability of supported graphene and graphite, Nat. Mater., 12 (2013) 925.
[89] K. Xu, J.R. Heath, Contact with what?, Nat. Mater., 12 (2013) 872.
[90] D.J. Preston, N. Miljkovic, J. Sack, R. Enright, J. Queeney, E.N. Wang, Effect of hydrocarbon adsorption on the wettability of rare earth oxide ceramics, Appl. Phys. Lett., 105(1) (2014) 011601.
[91] R. Nickerson, Plasma surface modification for cleaning and adhesion, in: Polymers, Laminations & Coatings Conference, TAPPI Press, San Francisco, California, USA, 1998, pp. 1101-1108.
[92] S.Y. Kim, K. Hong, K. Kim, H.K. Yu, W.-K. Kim, J.-L. Lee, Effect of n2, ar, and o2 plasma treatments on surface properties of metals, J. Appl. Phys., 103(7) (2008) 076101.
[93] I. Umezu, K. Kohno, K. Aoki, Y. Kohama, A. Sugimura, M. Inada, Effects of argon and hydrogen plasmas on the surface of silicon, Vacuum, 66(3) (2002) 453-456.
[94] C.H. Wang, V.K. Dhir, Effect of surface wettability on active nucleation site density during pool boiling of water on a vertical surface, J. Heat Transfer, 115(3) (1993) 659-669.
[95] N.I. Kolev, How accurately can we predict nucleate boiling?, Exp. Therm Fluid Sci., 10(3) (1995) 370-378.

[96] K.M. Balss, C.T. Avedisian, R.E. Cavicchi, M.J. Tarlov, Nanosecond imaging of microboiling behavior on pulsed-heated au films modified with hydrophilic and hydrophobic self-assembled monolayers, Langmuir, 21(23) (2005) 10459-10467.
[97] I. Langmuir, The adsorption of gases on plane surfaces of glass, mica and platinum, J. Am. Chem. Soc., 40(9) (1918) 1361-1403.
[98] A. Hedin, A.J. Johansson, C. Lilja, M. Boman, P. Berastegui, R. Berger, M. Ottosson, Corrosion of copper in pure o2-free water?, Corros. Sci., 137 (2018) 1-12.
[99] N.S. Saadi, L.B. Hassan, T. Karabacak, Metal oxide nanostructures by a simple hot water treatment, Sci. Rep., 7(1) (2017) 7158.
[100] P.L. Andresen, J. Hickling, A. Ahluwalia, J. Wilson, Effects of hydrogen on stress corrosion crack growth rate of nickel alloys in high-temperature water, Corrosion, 64(9) (2008) 707-720.
[101] K.R. Khedir, Z.S. Saifaldeen, T.M. Demirkan, A.A. Al-Hilo, M.P. Brozak, T. Karabacak, Robust superamphiphobic nanoscale copper sheet surfaces produced by a simple and environmentally friendly technique, Adv. Eng. Mater., 17(7) (2015) 982-989.
[102] M.R. Louthan, J.A. Donovan, G.R. Caskey, Hydrogen diffusion and trapping in nickel, Acta Metall., 23(6) (1975) 745-749.
[103] N.E. Todreas, M.S. Kazimi, Nuclear systems volume i: Thermal hydraulic fundamentals, third edition, CRC Press, 2021.
[104] J. Buongiorno, Can corrosion and crud actually improve safety margins in lwrs?, Ann. Nucl. Energy, 63 (2014) 9-21.
[105] H. Kim, H.S. Ahn, H.J. Kwak, M.H. Kim, D.E. Kim, Boiling crisis controlled by capillary pumping and viscous friction: Liquid penetration length and dry spot diameter, Appl. Phys. Lett., 109(24) (2016) 243901.
[106] H.D. Kim, M.H. Kim, Effect of nanoparticle deposition on capillary wicking that influences the critical heat flux in nanofluids, Appl. Phys. Lett., 91(1) (2007) 014104.
[107] Y. Song, L. Zhang, Z. Liu, D.J. Preston, E.N. Wang, Effects of airborne hydrocarbon adsorption on pool boiling heat transfer, Appl. Phys. Lett., 116(25) (2020) 253702.
[108] D.E. Kim, D.I. Yu, S.C. Park, H.J. Kwak, H.S. Ahn, Critical heat flux triggering mechanism on micro-structured surfaces: Coalesced bubble departure frequency and liquid furnishing capability, Int. J. Heat Mass Transfer, 91 (2015) 1237-1247.
[109] H. Hu, J.A. Weibel, S.V. Garimella, A coupled wicking and evaporation model for prediction of pool boiling critical heat flux on structured surfaces, Int. J. Heat Mass Transfer, 136 (2019) 373-382.
[110] L. Zhang, J.H. Seong, M. Bucci, Percolative scale-free behavior in the boiling crisis, Phys. Rev. Lett., 122(13) (2019) 134501.
[111] P. Lloveras, F. Salvat-Pujol, L. Truskinovsky, E. Vives, Boiling crisis as a critical phenomenon, Phys. Rev. Lett., 108(21) (2012) 215701.
[112] T. Charignon, P. Lloveras, D. Chatain, L. Truskinovsky, E. Vives, D. Beysens, V.S. Nikolayev, Criticality in the slowed-down boiling crisis at zero gravity, Phys. Rev. E, 91(5) (2015) 053007.
[113] K. Wang, C.-Y. Li, M. Pellegrini, N. Erkan, K. Okamoto, Extended development of a bubble percolation method to predict boiling crisis of flow boiling, Int. J. Heat Mass Transfer, 165 (2021) 120660.

[114] M. Ravichandran, G. Su, C. Wang, J.H. Seong, A. Kossolapov, B. Phillips, M.M. Rahman, M. Bucci, Decrypting the boiling crisis through data-driven exploration of high-resolution infrared thermometry measurements, Appl. Phys. Lett., 118(25) (2021) 253903.
[115] L. Zhang, R. Iwata, L. Zhao, S. Gong, Z. Lu, Z. Xu, Y. Zhong, J. Zhu, S. Cruz, K.L. Wilke, P. Cheng, E.N. Wang, Nucleation site distribution probed by phase-enhanced environmental scanning electron microscopy, Cell Reports Physical Science, 1(12) (2020) 100262.
[116] S.H. Kim, G.C. Lee, J.Y. Kang, H.S. Park, M.H. Kim, A study of nucleate bubble growth on microstructured surface through high speed and infrared visualization, Int. J. Multiphase Flow, 95 (2017) 12-21.
[117] D.I. Yu, H.J. Kwak, H. Noh, H.S. Park, K. Fezzaa, M.H. Kim, Synchrotron x-ray imaging visualization study of capillary-induced flow and critical heat flux on surfaces with engineered micropillars, Science Advances, 4(2) (2018) e1701571.
[118] R. Xiao, R. Enright, E.N. Wang, Prediction and optimization of liquid propagation in micropillar arrays, Langmuir, 26(19) (2010) 15070-15075.
[119] K. Yazdchi, S. Srivastava, S. Luding, Microstructural effects on the permeability of periodic fibrous porous media, Int. J. Multiphase Flow, 37(8) (2011) 956-966.
[120] B.R. Gebart, Permeability of unidirectional reinforcements for rtm, J. Compos. Mater., 26(8) (1992) 1100-1133.
[121] J.E. Drummond, M.I. Tahir, Laminar viscous flow through regular arrays of parallel solid cylinders, Int. J. Multiphase Flow, 10(5) (1984) 515-540.
[122] S. Cho, R. Tummala, Y. Joshi, Capillary performance of micropillar arrays in different arrangements, Nanoscale and Microscale Thermophysical Engineering, 22(2) (2018) 97-113.
[123] H.C. Brinkman, A calculation of the viscous force exerted by a flowing fluid on a dense swarm of particles, Flow, Turbulence and Combustion, 1(1) (1949) 27.
[124] C. Gerardi, J. Buongiorno, L.-w. Hu, T. McKrell, Study of bubble growth in water pool boiling through synchronized, infrared thermometry and high-speed video, Int. J. Heat Mass Transfer, 53(19) (2010) 4185-4192.
[125] S.H. Kim, G.C. Lee, J.Y. Kang, K. Moriyama, H.S. Park, M.H. Kim, Heat flux partitioning analysis of pool boiling on micro structured surface using infrared visualization, Int. J. Heat Mass Transfer, 102 (2016) 756-765.
[126] H. Sakashita, A. Ono, Boiling behaviors and critical heat flux on a horizontal plate in saturated pool boiling of water at high pressures, Int. J. Heat Mass Transfer, 52(3) (2009) 744-750.
[127] S. Adera, D. Antao, R. Raj, E.N. Wang, Design of micropillar wicks for thin-film evaporation, Int. J. Heat Mass Transfer, 101 (2016) 280-294.
[128] A. Chatterjee, J.L. Plawsky, P.C. Wayner, Disjoining pressure and capillarity in the constrained vapor bubble heat transfer system, Adv. Colloid Interface Sci., 168(1) (2011) 40-49.
[129] T. Liu, M.T. Dunham, K.W. Jung, B. Chen, M. Asheghi, K.E. Goodson, Characterization and thermal modeling of a miniature silicon vapor chamber for die-level heat redistribution, Int. J. Heat Mass Transfer, 152 (2020) 119569.
[130] B. Paul, Compilation of evaporation coefficients, ARS Journal, 32(9) (1962) 1321-1328.
[131] T.P. Allred, J.A. Weibel, S.V. Garimella, A wettability metric for characterization of capillary flow on textured superhydrophilic surfaces, Langmuir, 33(32) (2017) 7847-7853.

[132] Y. Song, S. Gong, G. Vaartstra, E.N. Wang, Microtube surfaces for the simultaneous enhancement of efficiency and critical heat flux during pool boiling, ACS Appl. Mater. Interfaces, (2021).
[133] S.G. Liter, M. Kaviany, Pool-boiling chf enhancement by modulated porous-layer coating: Theory and experiment, Int. J. Heat Mass Transfer, 44(22) (2001) 4287-4311.
[134] S.G. Kandlikar, Controlling bubble motion over heated surface through evaporation momentum force to enhance pool boiling heat transfer, Appl. Phys. Lett., 102(5) (2013) 051611.
[135] S. Gong, L. Zhang, P. Cheng, E.N. Wang, Understanding triggering mechanisms for critical heat flux in pool boiling based on direct numerical simulations, Int. J. Heat Mass Transfer, 163 (2020) 120546.
[136] P. Griffith, J.D. Wallis, The role of surface conditions in nucleate boiling, Chemical Engineering Progress Symposium Series, 56(30) (1958) 49-63.
[137] Y.Y. Hsu, On the size range of active nucleation cavities on a heating surface, J. Heat Transfer, 84(3) (1962) 207-213.
[138] A. Jaikumar, T.S. Emery, S.G. Kandlikar, Interplay between developing flow length and bubble departure diameter during macroconvection enhanced pool boiling, Appl. Phys. Lett., 112(7) (2018) 071603.
[139] B.B. Mikic, W.M. Rohsenow, P. Griffith, On bubble growth rates, Int. J. Heat Mass Transfer, 13(4) (1970) 657-666.
[140] Y. Nam, S. Sharratt, C. Byon, S.J. Kim, Y.S. Ju, Fabrication and characterization of the capillary performance of superhydrophilic cu micropost arrays, Journal of Microelectromechanical Systems, 19(3) (2010) 581-588.
[141] A. Jaikumar, S.G. Kandlikar, Pool boiling inversion through bubble induced macroconvection, Appl. Phys. Lett., 110(9) (2017) 094107.
[142] S.H. Kim, G.C. Lee, J.Y. Kang, K. Moriyama, M.H. Kim, H.S. Park, Boiling heat transfer and critical heat flux evaluation of the pool boiling on micro structured surface, Int. J. Heat Mass Transfer, 91 (2015) 1140-1147.
[143] B.S. Kim, S. Shin, D. Lee, G. Choi, H. Lee, K.M. Kim, H.H. Cho, Stable and uniform heat dissipation by nucleate-catalytic nanowires for boiling heat transfer, Int. J. Heat Mass Transfer, 70 (2014) 23-32.
[144] M.-C. Lu, R. Chen, V. Srinivasan, V.P. Carey, A. Majumdar, Critical heat flux of pool boiling on si nanowire array-coated surfaces, Int. J. Heat Mass Transfer, 54(25) (2011) 5359-5367.
[145] J.C. Godinez, D. Fadda, J. Lee, S.M. You, Development of a stable boehmite layer on aluminum surfaces for improved pool boiling heat transfer in water, Appl. Therm. Eng., 156 (2019) 541-549.
[146] H. Honda , H. Takamastu, J.J. Wei, Enhanced boiling of fc-72 on silicon chips with micro-pin-fins and submicron-scale roughness, J. Heat Transfer, 124(2) (2001) 383-390.
[147] M. Tetreault-Friend, R. Azizian, M. Bucci, T. McKrell, J. Buongiorno, M. Rubner, R. Cohen, Critical heat flux maxima resulting from the controlled morphology of nanoporous hydrophilic surface layers, Appl. Phys. Lett., 108(24) (2016) 243102.
[148] N.V. Upot, A. Mahvi, K. Fazle Rabbi, J. Li, A.M. Jacobi, N. Miljkovic, Scalable and resilient etched metallic micro- and nanostructured surfaces for enhanced flow boiling, ACS Applied Nano Materials, (2021).

[149] K.L. Wilke, D.S. Antao, S. Cruz, R. Iwata, Y. Zhao, A. Leroy, D.J. Preston, E.N. Wang, Polymer infused porous surfaces for robust, thermally conductive, self-healing coatings for dropwise condensation, ACS Nano, (2020).
[150] Z. Duan, H. Yang, S. Kano, K. Murakami, Y. Satoh, Y. Takeda, H. Abe, Oxidation and electrochemical behaviors of al2o3 and zro2 coatings on zircaloy-2 cladding by thermal spraying, Surf. Coat. Technol., 334 (2018) 319-327.
[151] R.G. Frieser, M.D. Reeber, Surface treatments of silicon to enhance thermal nucleation, J. Appl. Electrochem., 10(4) (1980) 449-457.
[152] B. Truong, L.-w. Hu, J. Buongiorno, T. McKrell, Modification of sandblasted plate heaters using nanofluids to enhance pool boiling critical heat flux, Int. J. Heat Mass Transfer, 53(1) (2010) 85-94.
[153] P. Hübner, W. Künstler, Pool boiling heat transfer at finned tubes: Influence of surface roughness and shape of the fins, International Journal of Refrigeration, 20(8) (1997) 575-582.
[154] D. Gorenflo, E. Danger, A. Luke, S. Kotthoff, U. Chandra, C. Ranganayakulu, Bubble formation with pool boiling on tubes with or without basic surface modifications for enhancement, Int. J. Heat Fluid Flow, 25(2) (2004) 288-297.
[155] A. Luke, Active and potential bubble nucleation sites on different structured heated surfaces, Chem. Eng. Res. Des., 82(4) (2004) 462-470.
[156] A. Luke, Pool boiling heat transfer from horizontal tubes with different surface roughness, International Journal of Refrigeration, 20(8) (1997) 561-574.
[157] G. Ribatski, J.M.S. Jabardo, Experimental study of nucleate boiling of halocarbon refrigerants on cylindrical surfaces, Int. J. Heat Mass Transfer, 46(23) (2003) 4439-4451.
[158] J. Addy, M. Olbricht, B. Müller, A. Luke, Pool boiling heat transfer on structured surfaces, Journal of Physics: Conference Series, 745 (2016) 032077.
[159] G.Y. Su, C. Wang, L. Zhang, J.H. Seong, R. Kommajosyula, B. Phillips, M. Bucci, Investigation of flow boiling heat transfer and boiling crisis on a rough surface using infrared thermometry, Int. J. Heat Mass Transfer, 160 (2020) 120134.
[160] L. Dong, X. Quan, P. Cheng, An experimental investigation of enhanced pool boiling heat transfer from surfaces with micro/nano-structures, Int. J. Heat Mass Transfer, 71 (2014) 189-196.
[161] Y. Suh, R. Bostanabad, Y. Won, Deep learning predicts boiling heat transfer, Sci. Rep., 11(1) (2021) 5622.
[162] K.N.R. Sinha, V. Kumar, N. Kumar, A. Thakur, R. Raj, Deep learning the sound of boiling for advance prediction of boiling crisis, Cell Reports Physical Science, 2(3) (2021) 100382.
[163] R.S. Hale, R.T. Bonnecaze, C.H. Hidrovo, Optimization of capillary flow through square micropillar arrays, Int. J. Multiphase Flow, 58 (2014) 39-51.
[164] A.S. Sangani, A. Acrivos, Slow flow past periodic arrays of cylinders with application to heat transfer, Int. J. Multiphase Flow, 8(3) (1982) 193-206.